UNIVERSITY OF CALIFORNIA,
IRVINE

Design of Bimetallic Complexes for the Cooperative Activation and Reduction of Carbon Dioxide

THESIS

submitted in partial satisfaction of the requirements
for the degree of

MASTER OF SCIENCE

in Chemistry

by

Steven Andrew Poteet

Thesis Committee:
Professor Jenny Y. Yang, Chair
Professor William J. Evans
Professor Alan F. Heyduk

2015

DEDICATION

In loving memory

of

Parthenia Grace Poteet

My Nanny

1942 - 2006

I think of you often and wonder what it would be like with you still here. Sometimes I can still hear your voice. But I will always feel your love.

TABLE OF CONTENTS

LIST OF FIGURES

LIST OF TABLES

LIST OF ABBREVIATIONS

ΔE_p	Peak potential separation
btu	British thermal unit
CO	Carbon monoxide
CODH	Carbon monoxide dehydrogenase
CV	Cyclic voltammetry
DBU	1,8-diazabicycloundec-7-ene
DCM	Dichloromethane
DOE	U.S. Department of Energy
DMF	N,N'-dimethylformamide
DMSO	dimethylsulfoxide
d	doublet
dd	doublet of doublets
E°	Standard potential
EA	Elemental analysis (C, H, N)
eq	equivalent
ESI-MS	Electrospray ionization mass spectrometry
EPR	Electron paramagnetic resonance
Fsal-n	N,N'-alkylenebis(3-formyl-5-methyl-salicylaldimine)
$Fc^{+/0}$	Ferrocene/ferrocinium internal reference (CV)
FT-IR	Fourier transform infrared spectroscopy
HOMO	Highest occupied molecular orbital
LUMO	Lowest unoccupied molecular orbital
m	multiplet
m/z	mass to charge ratio
μ_B	Bohr magneton
μ_{eff}	effective magnetic moment
NHE	Normal hydrogen electrode
NMR	Nuclear magnetic resonance
o	ortho
OAc	Acetate
O^tBu	*tert*-butoxide
ppm	parts per million
q	quartet
Salen	N,N'-ethylenebis(salicylimine)
Salpn	N,N'-propylenebis(salicylimine)
Salp	N,N'-phenylenebis(salicylimine)
SCE	Saturated calomel electrode
SEC	Spectroelectrochemistry
t	triplet
td	triplet of doublets
THF	tetrahydrofuran
TOF	Turnover frequency
TON	Turnover number

ACKNOWLEDGMENTS

I would first like to thank my chair and advisor Professor Jenny Yang. It has been a privilege to begin my graduate career with Dr. Yang and be an initial member of her lab. Thank you for your support and allowing me freedom with my project.

I would like to thank my committee members, Professor William Evans and Professor Alan Heyduk, who have been supportive during the course of my graduate career, as well as Professor Andy Borovik. Their guidance and advice has been instrumental. I also want to thank the National Science Foundation for funding and the opportunity to refrain from TA duties.

Mom and Dad, your love and advice has helped me all of my life, and probably even more so in graduate school. You think I don't listen, but I do. You have always been reliable, and I have always been stubborn, but you don't let that stop you from loving me, and for that I am deeply appreciative. I would not be where I am today without you. You provide the best examples a son can have. I always strived to live up to standards you set out for me, but I now know that you pushed me to live up to the standards I have set for myself. I am not done growing as a man, and I am sure that I have much more to learn from y'all.

Janelle, you have been my rock. Thank you for being patient with me and looking after my general well being. Your love and support helped me remain strong when facing hard decisions. You saw me at my best and at my worst, and you didn't waiver. I don't know what my time at UCI would have been like without you. I am truly blessed to have you in my life. You have no idea how much I look forward to our future and all the places it takes us.

To David, I want to thank you for the late night talks about research. It was great to bounce ideas off of you, especially when I would drive myself mad with them late in the evening. To Jeff, thanks for listening to me and keeping me grounded. Your friendship means a lot to me and continues to remains strong across the country as if I never left home. You guys have been with me through many walks in life, and I know there are many more to come.

I want to give a shout out to my lab mates, especially Zach and Brian. I really enjoyed our conversations and ability to cut up in lab, especially throwing the baseball in Aldrich Park. I want to also thank Casey, Chad, Jeff, Miles, among many others I'm sure I've missed. There were a lot of intelligent (and probably more unintelligent) conversations we've had over the two years I was with you.

ABSTRACT OF THE THESIS

Design of Bimetallic Complexes for the Cooperative Activation and Reduction of Carbon Dioxide

By

Steven Andrew Poteet

Master of Science in Chemistry

University of California, Irvine, 2015

Professor Jenny Y. Yang, Chair

Carbon dioxide emission continues to be an important topic regarding the future of our society, with its primary function being the leading contributor (by amount) to greenhouse gases. We aim to convert CO_2 to useful fuel derivatives, indirectly, by $2e^-$ reduction to carbon monoxide. This thesis details the preparation of complexes incorporating two metals in a Robson-type macrocycle to be investigated as a method for the catalytic reduction of carbon dioxide to carbon monoxide. The characterization of these complexes, as well as alternative methods of their syntheses, is reported herein. The complexes' reactivity and interaction with CO_2 was probed by cyclic voltammetry and spectrophotometric methods. Comparison to the well studied mono-metallic complexes, Co(salen) and Ni(salen) (salen = N,N'-ethylenebis(salicylimine)), was used to help establish the importance of a bimetallic cooperative effect for CO_2 activation and reduction.

CHAPTER 1

The CO_2 Problem

1.1 Introduction and scope

The consumption of energy continues to be a growing concern, and the demand for sustainable and renewable energy sources has become an important topic in the scientific, political, and commercial sectors.[1,2] Closely related to this lies the concern of climate change that has dominated research efforts in the past couple of decades.[3] The impact of global climate change has far reaching consequences that extends to agriculture, wildlife, and our general well being. Political efforts have been implemented in Western nations to restrict the amount of pollutants emitted by industries and automobiles; however, these restrictions still do not eliminate emissions. More importantly, emerging nations are expanding their technologies to keep up with demand, and the governments do not implement the same constraints seen in established countries. The U.S. DOE predicts an enormous growth period during the next 20 years with the primary contributors being emerging nations. With this, the world energy demand is expected to rise almost 50% from 573 quadrillion btu to 770 quadrillion btu (Figure 1.1).[4]

Two serious problems arise from this outlook: Where will this energy come from and how will we control or eliminate the resulting pollutants? To address these questions, we can look to control the emission of certain pollutants by converting them into sources of energy. There are many methods of procuring renewable energy sources, such as sunlight and wind, but the ability to store the energy generated during periods of low input remains elusive.[5] One method of "storing" this energy is in the form of chemical bonds that can be broken at times of low input.

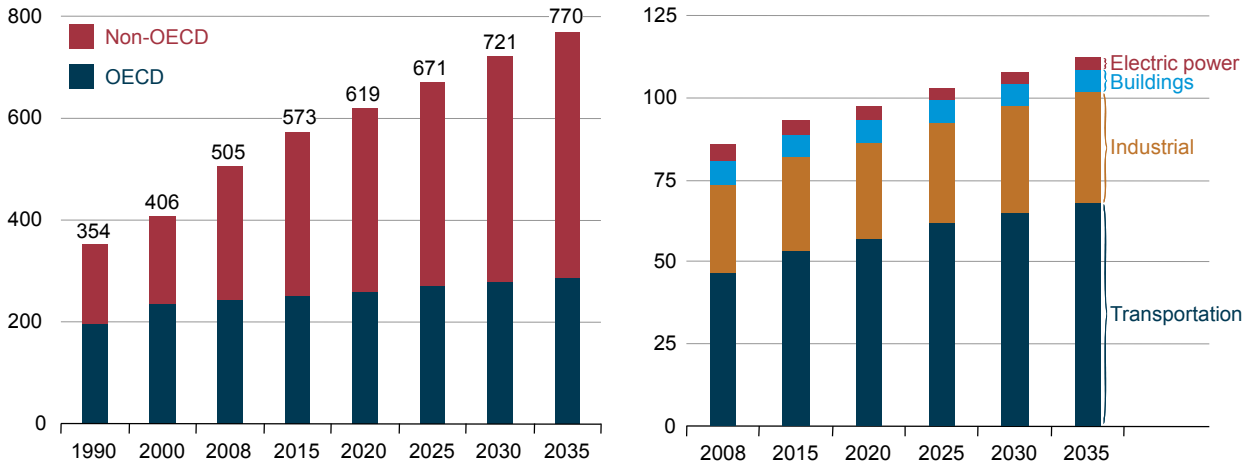

Figure 1.1. *Left*: Projected world energy consumption. OECD= Organization for Economic Cooperation and Development nations (Quadrillion Btu). Current OEDC countries (2010) include: USA, Canada, Mexico, Austria, Belgium, Chile, Czech Republic, Denmark, Estonia, Finland, France, Germany, Greece, Hungary, Ireland, Italy, Luxembourg, the Netherlands, Norway, Poland, Slovakia, Slovenia, Spain, Sweden, Switzerland, Turkey, UK, Japan, South Korea, Australia, New Zealand and Israel. *Right*: World liquids consumption by sector (million barrels per day). Figure taken from Ref 4.

Traditional sources of energy, such as gasoline and diesel, utilize a combustion reaction to generate carbon dioxide as a major byproduct. Because of this, carbon dioxide is being produced at an unsustainable rate. Since the 1960's, CO_2 has risen nearly 25%, as indicated in Figure 1.2.[6] The rise in CO_2 production is intimately linked to the global energy problem through fossil fuel combustion. Significant progress towards the utilization of CO_2 began to develop in the 1970's, but a system that can effectively scavenge and convert CO_2 to useful materials remains largely unsolved.

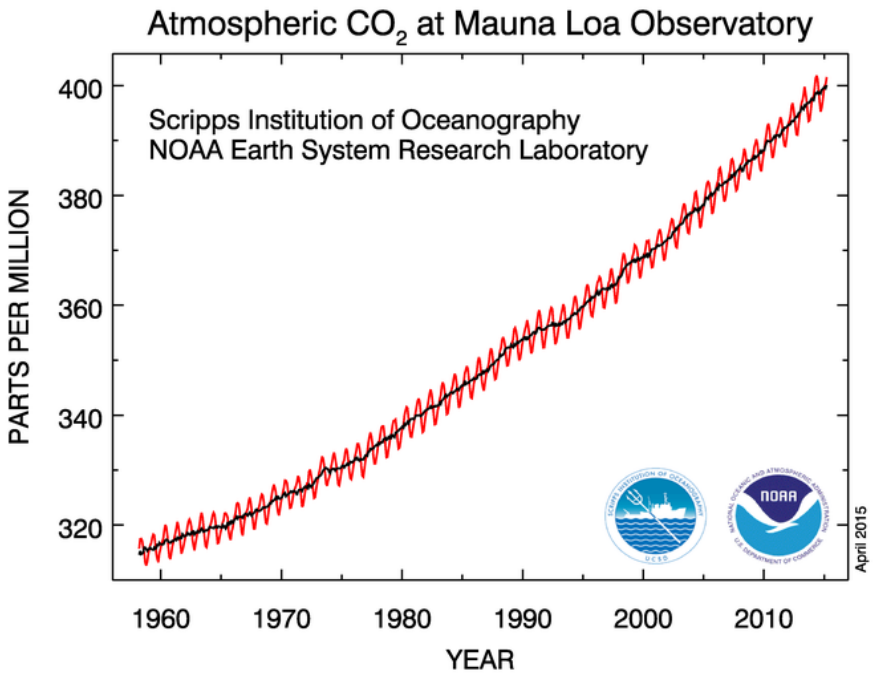

Figure 1.2. The Keeling curve displaying CO_2 emission data in ppm taken at Mauna Loa.[6]

Since more than 30 billion tons of carbon dioxide is produced each year, methods are being developed to convert this pollutant into a potential carbon feedstock for existing technologies that rely on petrochemical processes.[7] In addition, it should be noted that the primary method of energy consumption is projected to remain as transportable fuels, such as gasoline and diesel (Figure 1.1). If carbon dioxide can be reduced to carbon monoxide in bulk (Table 1.1), it could be utilized in the Fisher-Trospch (equation 1.1) process along with H_2 to produce synthetic hydrocarbons.[8] These hydrocarbons can then be combusted to produce CO_2 and H_2O, producing a net neutral carbon cycle (Figure 1.4).

$$2(n+1)\,H_2 \;+\; n\,CO \longrightarrow C_nH_{(2n+2)} \;+\; n\,H_2O \qquad (1.1)$$

This is particularly attractive for several reasons: a) the Fisher-Trospch reaction is already an industrial process b) synthetic hydrocarbons are the main component of gasoline and would allow us to retain our current infrastructure that relies on liquid fuels c) the combustion of the resulting hydrocarbons would form CO_2 and H_2O, resulting in a net carbon neutral cycle.

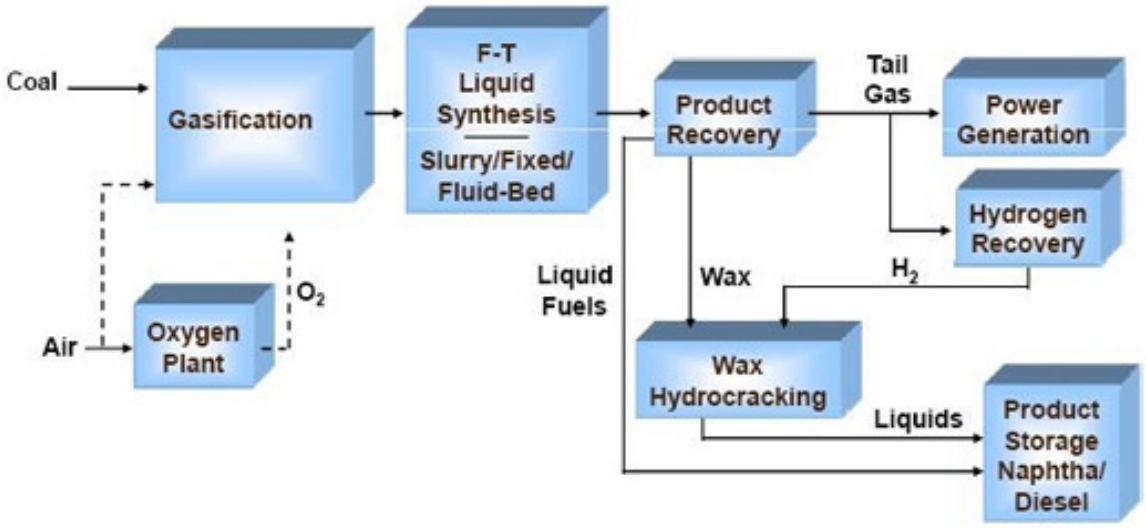

Figure 1.3. Simplified flow chart for Fischer-Tropsch fuel processes.[9]

Figure 1.3 describes a simplified infrastructure for Fischer-Tropsch based processes. With the mass production of CO, the need for coal would be eliminated thus lessening our dependence on fossil fuel sources. Higher molecular weight paraffins are more desired, which represent liquid fuels and diesel. These reactions operate under high temperatures and pressures that require a catalyst. This catalyst depends on the preference for the molecular weights desired, where an Fe-based catalyst is most commonly used with promotors and high surface area binders. Cobalt, while much more costly, demonstrates lower water-gas-shift reactivity, and is sometimes used to lower the side reactions to create more diesel products.

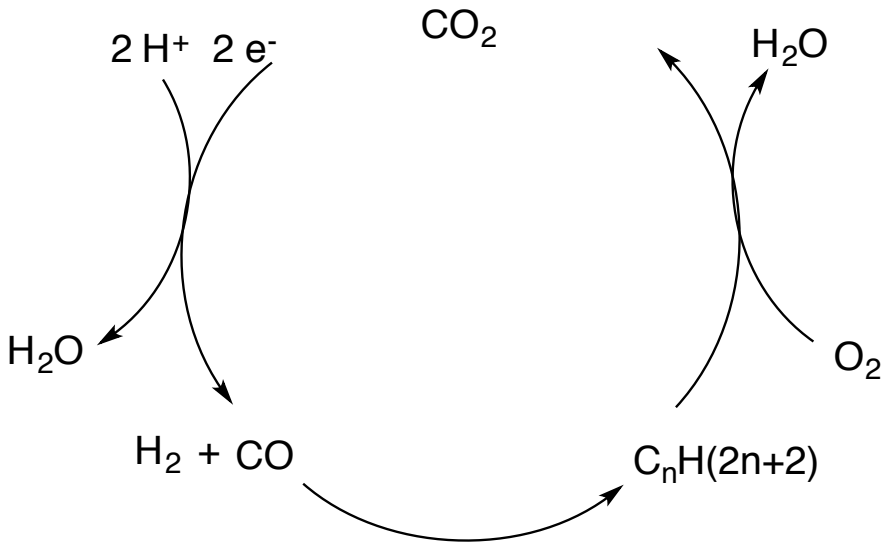

Figure 1.4. Net carbon-neutral cycle for CO_2.

The remainder of Chapter 1 will focus on efforts to overcome the thermodynamic and kinetic barriers of CO_2 activation. Section 1.3 will focus on the biological approach, while section 1.4 will divulge synthetic attempts and current approaches towards CO_2 activation and reduction. The remainder of this thesis will focus on synthetic approaches towards developing models to bind and reduce carbon dioxide. Chapter 2 will describe the synthesis and characterization of these complexes, detailing the success and challenges of each ligand design. Chapter 3 attempts to discuss the characterization of the redox events seen in the synthesized complexes, as well as other important factors such as stability in the presence of acids. Chapter 4 will act as an introduction into the ability of these complexes to interact with CO_2, and the challenges that remain for this project.

1.2 Thermodynamics of CO_2 reduction

There are many ways to approach the reduction of CO_2. The most common pathways are listed in Table 1.1; however, there are still major challenges to perform these reactions. For example, CO_2 is kinetically inert and relatively unreactive, requiring extreme conditions to convert it into more desired commodity chemicals. The relative inertness of carbon dioxide lies simply in the bonding geometry. The molecule adopts a linear geometry, with polar C=O bonds, yet remains nonpolar overall (Figure 1.5). In general, only strong nucleophiles can take advantage of these polar bonds, although this is not necessarily useful since strong nucleophiles result in net loss of energy with respect to the thermodynamic cycles.

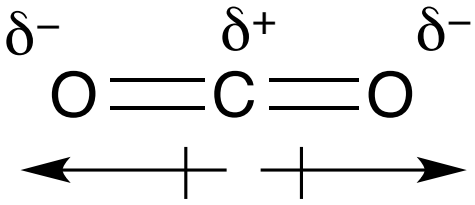

Figure 1.5. Polarity of CO_2.

The general reduction pathways involve 2, 4, 6 and 8 electron processes, with the addition of protons necessary to complete the charge balance (Table 1.1). While the standard free energy values are only mildly endergonic, the actual potentials at which reduction occurs happens at more negative potentials than the standard potentials listed. This excess energy required to perform these reactions is called the overpotential.[10] For example, the reduction of CO_2 to CO on a glassy carbon electrode in the presence of H^+ occurs at -2.6 V vs. $Fc^{+/0}$ in acetonitrile, lying approximately 1.7 V more negative than the approximate value at pH 7 (equation 1.3).[11] Overpotentials are a measure of inefficiency by

measuring the excess energy needed to drive the reaction past the standard potential. The more energy needed to power this reaction results in lower *overall* yield of energy, which is undesirable. This overpotential is a consequence of the large activation barriers in the reductive process. Therefore, to understand the reasons behind the difficulty of this reaction, one must consider the kinetic limitations, specifically the activation barriers for individual steps. For most processes, CO_2 must undergo a geometry change upon reduction, adopting a bent conformation that results in a large endergonic energy penalty, shown in equation 1.2. It is for this reason that a catalyst must be involved to aid in this first step. Catalysts increase reaction rates by lowering activation energies through an alternative mechanism. This thesis mostly concerns electrocatalysts, whereby the catalyst in its resting state is reduced at an electrode surface, generating a reactive complex that can react with a substrate such as CO_2. One can think of this process as an electrode being the source of electrons, supplied to the catalyst that is responsible for the reduction of the substrate.

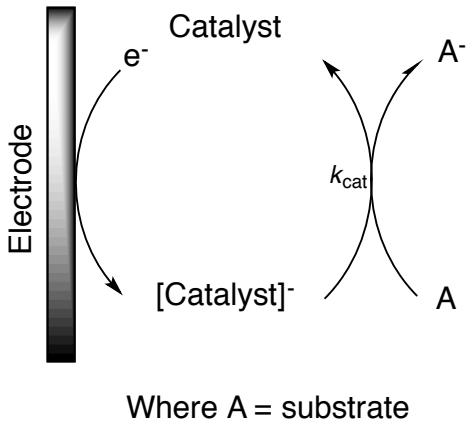

Figure 1.6. General schematic of an electrocatalyst operating at reducing conditions.

Reactions 1.5-1.7 involve processes that incorporate more than 2 e^-/H^+. While the endergonic barriers are lower, the kinetics and proton shuttling remain a challenge to drive these reactions selectively. In addition to the thermodynamic and kinetic barriers

associated with CO_2 reduction, it is important to remember that protons must be in solution for most of these processes. The reduction of H^+ to H_2 (equation 1.8) occurs at more mild potentials than that for the 2 electron process for CO_2 reduction, presenting a competitive reaction that must be avoided for efficient catalyst systems. This competition has limited several catalysis in literature, so the development of CO_2 reduction catalysts needs to be selective to avoid this competitive reaction.[12-14]

Table 1.1. CO_2 reduction reactions at pH 7 vs. NHE at 1 atm

	E° (V)	
$CO_2 + e^- \longrightarrow CO_2^{-\bullet}$	-1.9	(1.2)
$CO_2 + 2\,e^- + 2\,H^+ \longrightarrow CO + H_2O$	-0.53	(1.3)
$CO_2 + 2\,e^- + 2\,H^+ \longrightarrow HCOOH$	-0.61	(1.4)
$CO_2 + 4\,e^- + 4\,H^+ \longrightarrow H_2CO + H_2O$	-0.48	(1.5)
$CO_2 + 6\,e^- + 6\,H^+ \longrightarrow H_3COH + H_2O$	-0.38	(1.6)
$CO_2 + 8\,e^- + 8\,H^+ \longrightarrow CH_4 + 2\,H_2O$	-0.24	(1.7)
$H^+ + 2\,e^- \longrightarrow H_2$	-0.41	(1.8)

1.3 Biological approaches towards CO_2 binding

Molecular catalysts are often inspired by active sites found in enzymes that can perform difficult reactions.[15-24] Many enzymes have inspired fascinating work, such as FeFe-hydrogenase or the Fe-heme center of hemoglobin.[25-37] To date, there have been two enzymes that catalyze the reversible reduction of CO_2 to CO: the O_2-sensitive enzyme containing a $[Fe_4S_5Ni]$ site and the aerobic [MoSCu]-containing enzyme found in *Oligotropha carboxidovorans*. Both enzymes contain bimetallic metal centers, incorporating

a hard and soft combination of metals. Of interest to our lab is the [Fe_4S_5Ni] active site found in carbon monoxide dehydrogenase (CODH II) of *Carboxydothermus hydrogenoformans*, which operates at near thermodynamic potentials (-0.52 V vs. SHE at pH 7) to reversibly oxidize CO to CO_2.[38] We want to take inspiration from these sites to understand how they transfer electrons and protons to catalyze this reaction selectively and at relatively no overpotential.

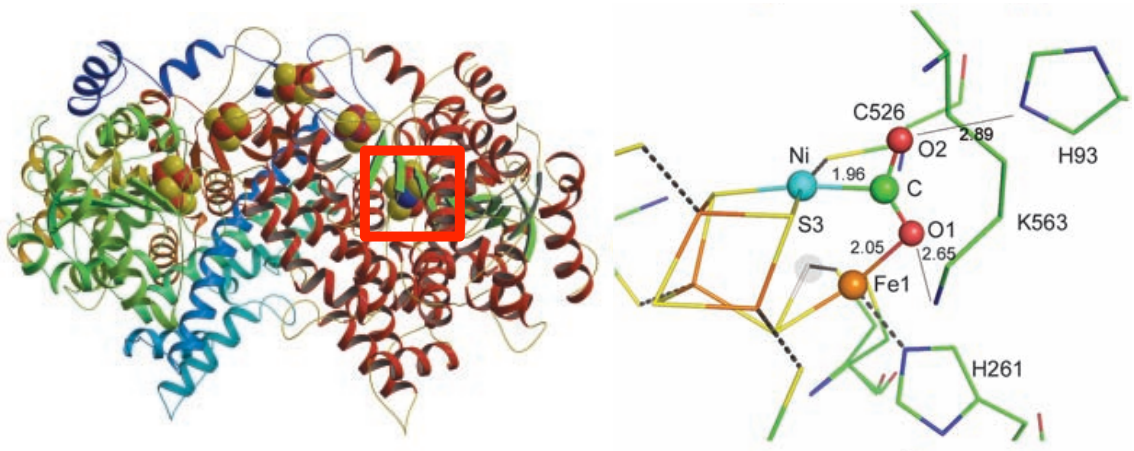

Figure 1.6. *Left*: crystal structure of CODH II dimer of *Carboxydothermus hydrogenoformans* refined at 1.3 Å (red box indicates the position of the [NiFe] active site. *Right*: [NiFe] active site of CODH II bound to CO_2.[39]

The active site of CODH II was structurally characterized by Dobbek and company in 2002 and was found to contain an iron-sulfur [3Fe-4S] cluster as well as a Ni and Fe atom bridged to complete the cluster assembly.[3,39,40] A series of four [4Fe-4S] clusters shuttles electrons to the active site, where the reversible oxidation of CO occurs. X-ray crystallographic data and spectroscopic methods have revealed that the active site contains a square planar Ni(II) ion and an asymmetric high spin, four-coordinate Fe(II) ion, separated at a distance of 2.7 Å (Figure 1.6). This bimetallic system works cooperatively to bind CO_2, and with the help of the secondary coordination sphere, cleaves the C=O bond to

generate CO. The oxidation, or reverse process, occurs at rates of 40,000 s^{-1} while the reduction reaction occurs at a modest 45 s^{-1}.[38] This cooperative binding is essential to lowering the activation barrier, as can be seen by the negligent overpotentials observed. It is generally thought that when reduced, Ni(I) acts as a Lewis base to interact with the LUMO of CO_2, wherby it coordinates to the carbon atom as evidenced by X-ray diffraction. The resulting negative charges that are localized on the oxygen atoms are then stabilized by the Lewis acidic iron, along with hydrogen bonding in the secondary coordination sphere, to help lower the endergonic penalty described in section 1.2.

The aerobic CODH utilizes a [MoCu] cluster to aid in the oxidation of CO to CO_2.[41] The use of a bimetallic system again indicates the importance of the Lewis base/acid pair to stabilize the carboxylate intermediates. The mechanism by which CO is oxidized has not been fully described, and the turnover is lower at 100 s^{-1} compared to the [NiFe] CODH. The reducing capability of Cu(I) is not a powerful enough for reaction 1.3, and therefore has not been studied as intensely as the [NiFe] equivalent.[42-44]

Our aim is to utilize first row transition metals and maximize the efficiency of the catalyst (i.e. turnover number, rate, overpotential, etc). We believe the incorporation of a bimetallic framework that works with first-row transition metals has the capability to work cooperatively to bind CO_2 and stabilize the carboxylate intermediate, similar to the $[Fe_4S_5Ni]$ cubane shown in Figure 1.7.

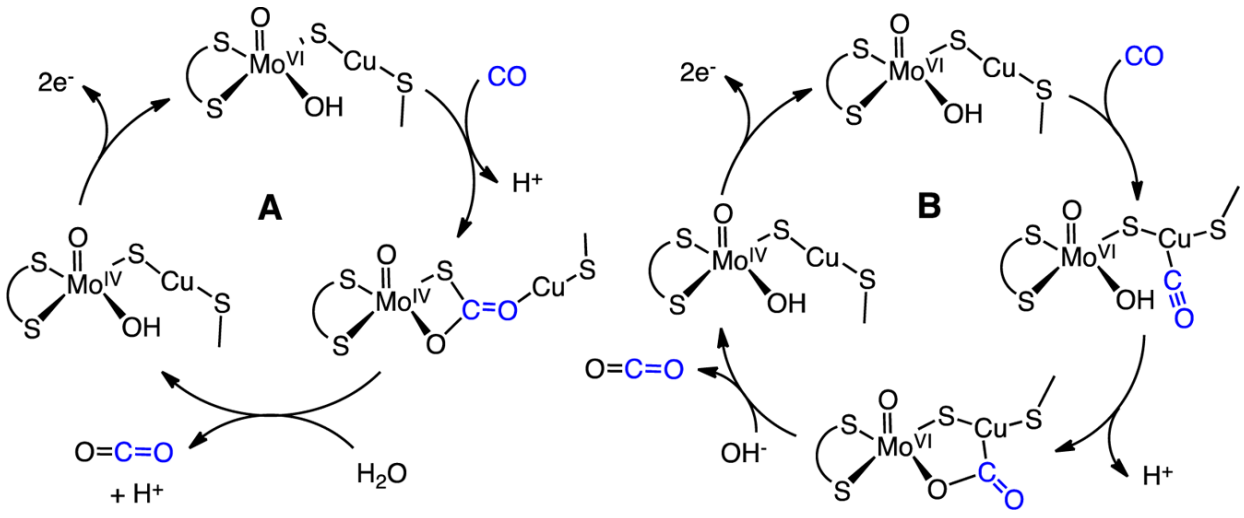

Figure 1.8. Proposed catalytic cycle of [MoCu] CODH. *Left*: Based on isocyanide inhibited enzyme. *Right*: Based on CO coordination to Cu. Figure taken from Ref. 3.

1.4 Synthetic approaches towards CO_2 binding

Since the 1970's, CO_2 utilization has generated a large amount of interest. A vast number of synthetic systems have been designed, where many focus on the $2e^-$ reduction processes (equations 1.2 & 1.3, see below for examples). As mentioned previously, one of the main issues other than chemical inertness, is selectivity, with many of these promising catalysts more suited for H^+ over CO_2 reduction. Almost all known CO_2 reduction catalysts contain metal centers. It is worth noting that many of these metal centers are precious metals, such as Pt, Ru & Rh and it is desirable to develop catalysts that contain earth abundant metals when thinking of the costs on a large scale.[13,14,45-56]

For CO_2 reduction by molecular complexes, the mechanism can be separated into four general reactions: electron transfer to the complex, CO_2 binding, C-O bond cleavage, and release of CO. The following breaks down the requirements individually.

Electron transfer to the complex is dictated by the reduction potentials of the complex. The overall reduction of CO_2 to CO is a $2e^-$ process, however, only a single electron is required to bind CO_2 to the complex. During catalysis, a second electron is needed to complete the reaction. The potential at which this occurs can depend on several factors, such as the influence of the bound carboxylate on the metal center. This can influence the second reduction, whereby the potential needed is not necessarily at the potential to reduce the complex by $2e^-$ in the absence of CO_2.

After electron transfer to the complex, a binding event occurs between CO_2 and the catalyst. As mentioned in Section 1.2, at low overpotentials, binding is generally regarded as the rate-limiting step. This is true for many complexes with varying metals, such as Ni, Fe, Co and Pd. The rate constant is dependent on the potentials at which reduction occurs, where more negative potentials increase the rate of the reaction linearly with *k*. The rate of binding does not necessarily dictate the overall catalytic rate, since the binding of CO_2 with complexes at higher overpotentials is not the rate-limiting step.

Once bound, the C-O bond must be cleaved to generate CO and O^{2-}. This step varies between complexes and may require a second electron, protons, or solvent rearrangement in order for the reaction to occur. In the absence of protons, the O^{2-} acceptor is a second equivalent of CO_2 to generate carbonate and CO. In the presence of protons, water is formed from this oxide and the rate of C-O cleavage is influenced by proton concentration. Again, more negative potentials increase the rate of C-O cleavage, but are not desired for efficient electrocatalysts due to high overpotentials.

Once the oxide has been transferred, it is necessary to release CO. Since CO is regarded as a strong ligand, this release may impede reaction rates if the M-CO bond is

strong. The strength of the M-CO can potentially be modulated by the coordination geometry of the metal ion that is bound to CO.

1.4.1 Synthetic models utilizing cooperative interactions

Of the complexes that can reduce carbon dioxide, many of the successful examples utilize a cooperative interaction to aid in the binding of CO_2.[3,57] Metal cyclams, specifically Ni(I) and Co(I), have been extensively studied as electrocatalysts since the early 1980's by Fujita *et. al*.[58-62] Amine protons in the secondary coordination sphere play an intricate role in the reactivity of the complex. Substitution of these protons to methyl substituents prevents this hydrogen bonding to the carboxylate and limited reaction with CO_2 occurs. In addition, the stereoposition of the protons influences the binding constants of the substrate, where protons directed towards the binding site increases the rate of reduction as opposed to protons directed opposite of the binding site.

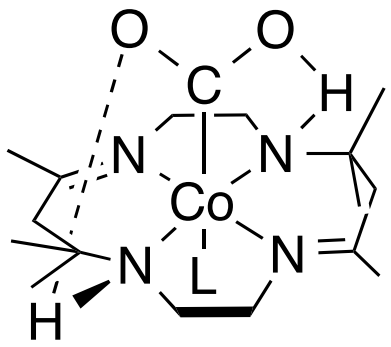

Figure 1.9. Proposed representation of CO_2 bound to a Co(cyclam) complex.

Work done by Dubois and coworkers in the early 1990's demonstrated the effectiveness of $[Pd(triphosphine)solvent]^{2+}$ complexes towards CO_2 reduction in acetonitrile.[63-65] The electrogenerated Pd(I) complex at -1.28 V is strong enough to interact

with CO_2, while Pd(0) is required for H^+ reduction (Figure 1.10). The most productive [Pd(triphosphine)solvent]$^{2+}$ derivative, containing an ethyl backbone (designated etpC), showed Faradaic efficiencies of 85% for CO vs. 16% for H_2, displaying high selectivity for CO_2 reduction over H^+ reduction. Turn over frequencies (TOF) ranged from 1-60 s^{-1}, while the turnover numbers (TON), however, peaked at a modest 130. This is due to the formation of a Pd-Pd bond with a second equivalent of the complex during electrocatalysis, where the dimer shows no reactivity towards CO_2 reduction.

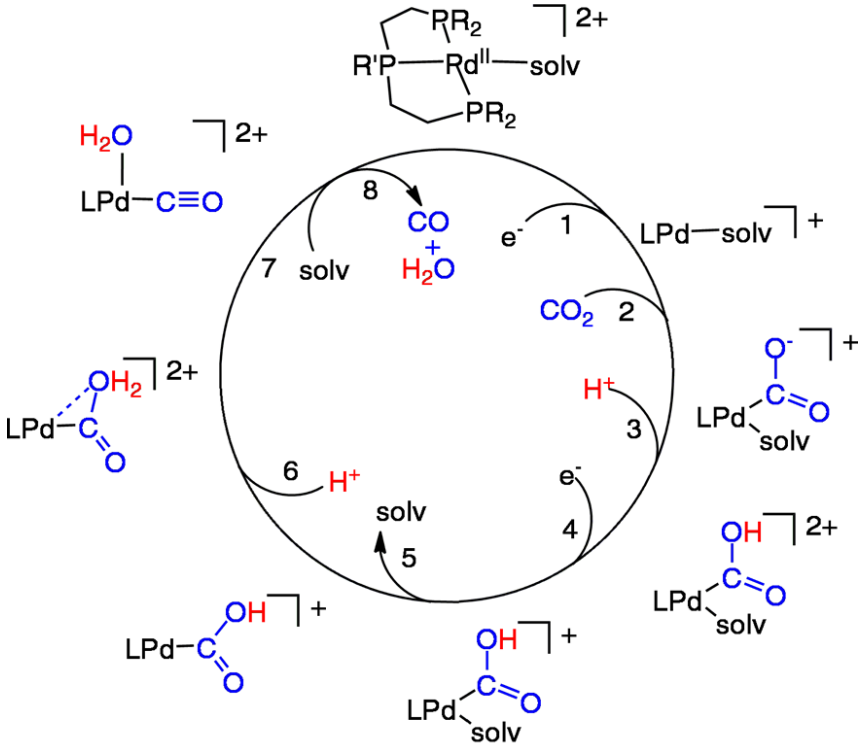

Figure 1.10. Proposed catalytic cycle for [Pd(triphosphine)solvent]$^{2+}$ complexes. Figure taken from Ref 3.

Bipalladium complexes were developed in an attempt to invoke cooperative effects.[48] The TOF increased by 10^3 $M^{-1}s^{-1}$, however, the TON decreased dramatically through rapid deactivation. It is interesting to note that although the TON was still

hindered, the TOF increased substantially. It is proposed that one Pd center interacts with the LUMO of carbon while the second Pd binds the oxygen, similar in manner to the bimetallic interactions seen in CODH II. The Pd-Pd bond formation is likely due to identical redox potentials for each Pd atom, something that is likely prevented in CODH II by the use of two varying metals.

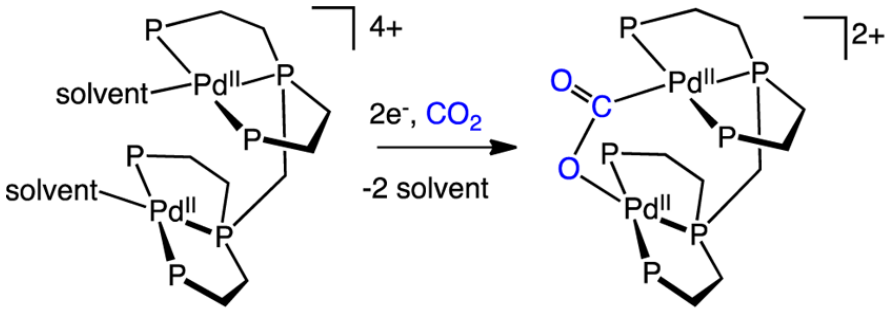

Figure 1.11. Proposed structure of CO_2 bound to the bipalladium phosphine complexes developed by Dubois & co. Figure taken from Ref 3.

In the 1980's, Floriani, Zanazzi, Pletcher, Lewis, and others observed the reactivity of Co(salen)[66,67] in the presence of alkali ions in DMF solutions.[12,61,68-72] Reduction of Co(salen) in the presence of M^+ (where M = Li, Na, K, Cs) leads to complexation of the alkali metal with the oxygen atoms of the salen ligand. This Co(I) bimetallic complex is then able to bind CO_2 across the Co-Li interface. Co(I) is a strong enough reductant to interact with the carbon atom with the Lewis acidic M^+ available to stabilize the resulting negative charge as described above. This complex is able to reduce CO_2 to CO, albeit with low turnovers. In the absence of H^+, the $2e^-$ reduction proceeds via bicarbonate formation using two equivalents of CO_2, as shown in Figure 1.13.[12] The complex formed upon reduction of Co(salen) by 1 e^- in the presence of Li and CO_2 was crystallized to show carbon dioxide was bound across the metal centers. A second equivalent of CO_2 binds, where a second electron

results in the release of bicarbonate. The resulting Co(I)-CO complex then dissociates to reform the active catalyst. It is believed that the dissociation of CO prevents rapid turnovers from occurring and low TOF are obtained. In the presence of H^+, the Faradaic efficiencies of CO decrease to < 5%, with H_2 as the primary product.

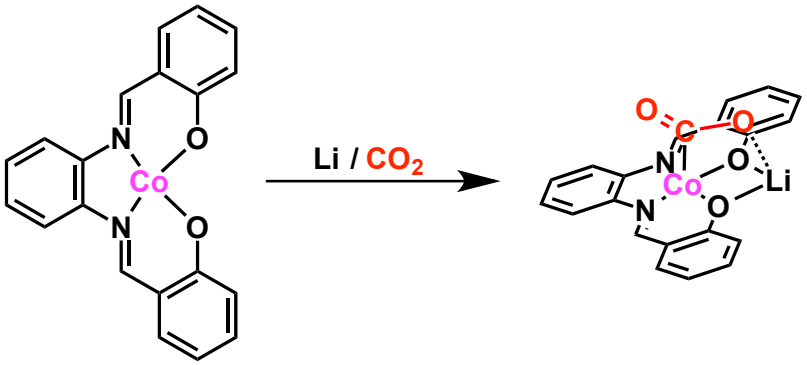

Figure 1.12. Binding of CO_2 to reduced Co(salen) in the presence of Li^+.

It is to this Co(salen) system that we have modeled our catalyst development from. Our goal is to expand from the work done on Co(salen) and incorporate a bimetallic framework consisting of first row transition metals. Our aim is to study the cooperative nature of bimetallic frameworks in a salen-type macrocycle, whereby controlled modifications of the ligand and metal combination will enable us to understand the dynamics involved for CO_2 binding and reduction.

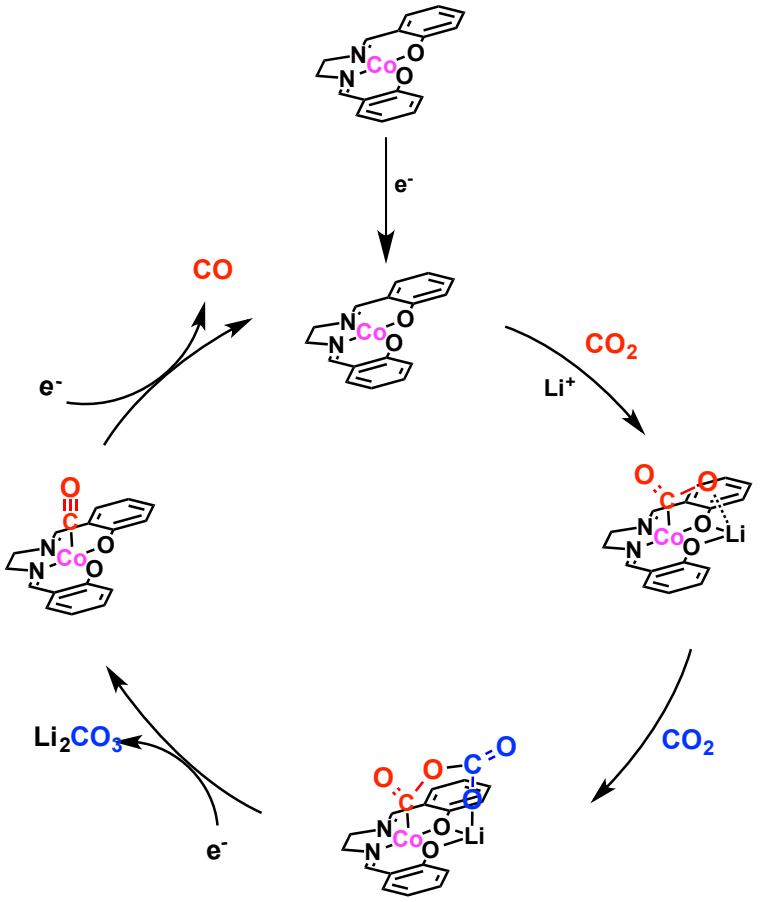

Figure 1.13. Catalytic cycle for the reduction of CO_2 by Co(salen) in the absence of H^+.

1.5 Lewis acid/base interaction and inspiration of ligand design

As mentioned in section 1.4.1, we want to understand the role of bimetallic cooperation between metal centers and how this affects CO_2 reduction processes. Co(salen) has shown encouraging results displaying the importance of cooperative Lewis effects to aid in the reduction of CO_2. Due to the relatively limited but promising literature of Co(salen) reactivity, we wanted to start with a system that could model closely to Co(salen). The addition of two transition metals, plus a ligand scaffold that can readily be

modified, would allow us to tune the complex to achieve an optimum cooperative design for CO_2 reduction.

The ligand scaffold we decided to use is a disalen-type ligand first reported by Robson and coworkers in 1970.[73-83] Historically, these complexes have mostly been studied for their magnetic properties, especially orbital exchange interactions between the two metal centers.[84-92] Condensation of 2 equivalents of diaminopropane, diformylphenol, and MCl_2 (where M = Zn, Cu, Ni, Co, Fe, Mn) resulted in the homobimetallic complex, denoted $M_2L^2Cl_2$. Attempts of synthesizing the metal-free ligand were unsuccessful for many years, resulting in polymeric compounds.[93] Because of this, the ligand is usually synthesized using a template method, sometimes even by templating around lead, followed by metathesis with MSO_4 to generate the homobimetallic complex.[94,95]. It wasn't until recently that the metal-free macrocyclic ligand was successfully made.[96,97]

In 1972, Okawa and Kida developed an alternative approach (shown later in Scheme 2.5), opting to use a step-wise procedure.[86,94,98-104] Condensation of 2 equivalents of diformylphenol with only 1 equivalent of diaminopropane resulted in the metal free ligand $L^{2'}$ (see abbreviations), or noted by the authors as Fsal-3. Reaction with 1 equivalent of $M(OAc)_2$ deprotonates the phenolic protons to form acetic acid while binding the M(II) ion to the N_2O_2 site. Condensation of a second equivalent of diaminopropane completes the macrocycle structure, whereby addition of MCl_2 resulted in the bimetallic species $M^aM^bL^2Cl_2$. Chapter 2 will focus on attempts to synthesize and characterize complexes inspired by Robson and Okawa/Kida.

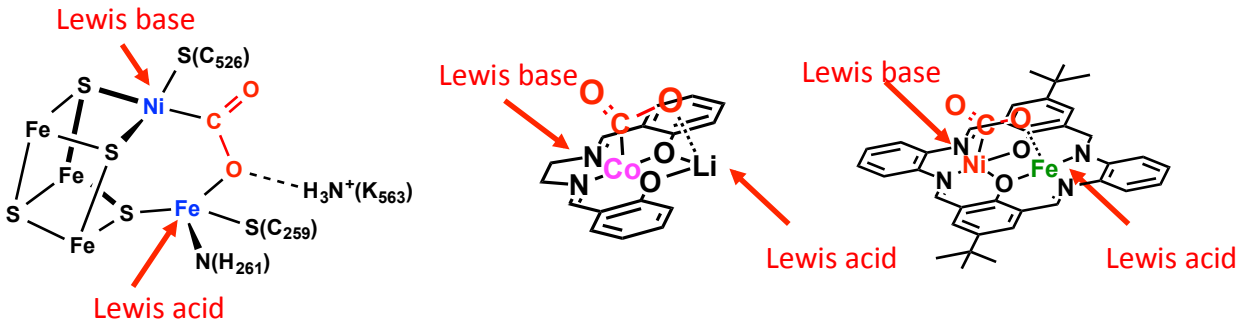

Figure 1.14. Desired characteristics in synthetic bimetallic complexes.

Keeping the mechanism of CODH II in mind, our goal is to have a Lewis basic site that, when reduced, is a strong enough of a nucleophile to interact with the LUMO of CO_2. The second metal site must therefore act as the Lewis acid and stabilize the negative charge. For the basic site, mid to late metals, such as Ni and Co, are preferred, whereas the acidic site would consist of mid to early metals, such as Fe or Mn. One must keep in mind the oxophilicity of the Lewis acidic metal, where early metals generate strong M-O bonds that may inhibit oxide removal from the catalyst. This would be detrimental to catalysis by inhibiting turnover. We aim to provide an acidic metal ion that upon oxide formation can be protonated to form water, which is labile and can be removed. Herein, this manuscript will describe various attempts to develop these complexes, their characterization, stability of the complexes in electrocatalytic conditions, and initial reactivity with CO_2.

CHAPTER 2

Synthetic Approaches

2.1 Synthesis and characterization of $[NiML^1]^{2+}$ complexes

Initial efforts to yield the bimetallic Robson-type complex began with attempts to create the metal-free macrocycle, followed by insertion of the desired metals to obtain the homobimetallic complex. However, this route is not straightforward and the metal-free ligand was not readily obtained. In an attempt to create the nickel homobimetallic complex, a monometallic complex was obtained. Condensation of 2 equivalents of 4-*tert*-butyl-2,6-diformylphenol with 2 equivalents of *o*-phenylenediamine in the presence of 1 equivalent of $[Ni(H_2O)_6](BF_4)_2$ in refluxing methanol produces a dark red product owing to the mono-Ni complex $[NiH_2L^1](BF_4)_2$ shown in Scheme 2.1. This is similar to what was observed by Robson, where it was shown that the template synthesis using $[Ni(H_2O)_6](ClO_4)_2$ instead of $NiCl_2$ resulted in the addition of only a single nickel, with the second pocket site consisting of phenolic protons hydrogen bonded to the imines.[73,105,106]

Scheme 2.1. Synthesis of $[NiH_2L^1](BF_4)_2$.

^{1}H NMR, ESI-MS and X-ray crystallography were used to confirm the product. The complex contains a low-spin four coordinate Ni(II) ion, while the remaining cavity remains protonated, allowing the complex to be NMR active. The ^{1}H NMR displays a resonance at 13.7 ppm, corresponding to the hydrogen-bonded protons in the non-metallated pocket. Crystallographic data confirmed that only a single nickel occupied a pocket, with 50% delocalization across the two coordination sites.

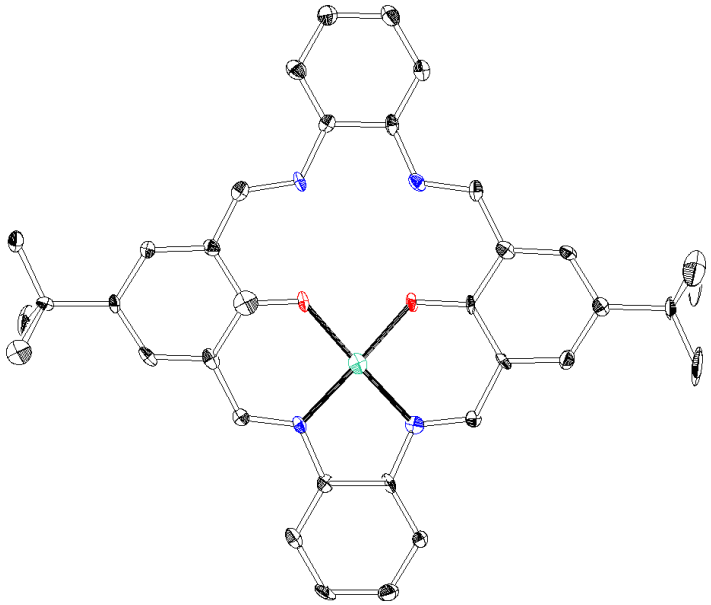

Figure 2.1. Ortep diagram of $[NiH_2L^1](BF_4)_2$. Ellipsoids are shown at 50% probability. A second molecule in the asymmetric unit, hydrogens and BF_4 counter ions have been omitted for clarity. The ortep diagram is shown with no anisotropy and only for structural representation.

This complex provided us with two advantages: a) Ni remains square planar, contrary to literature, making characterization more facile b) to create the heterobimetallic complex, one can simply deprotonate in the presence of a metal salt to yield the appropriate $[NiML^1](BF_4)_2$ complex. The heterobimetallic complexes with the L^1 ligand were synthesized in the following way (Scheme 2.2): $[NiH_2L^1](BF_4)_2$ was dissolved in 5 mL of DMF under an inert atmosphere of N_2. A THF solution (1 mL) of KO^{t}Bu was then added,

followed by the addition of an acetonitrile solution of $[M(CH_3CN)_n](BF_4)_2$ (where n = 4,6). The products were then precipitated out of DMF using diethyl ether and recrystallized.

Scheme 2.2. Synthesis of heterobimetallic complexes $[NiML^1](BF_4)_2$.

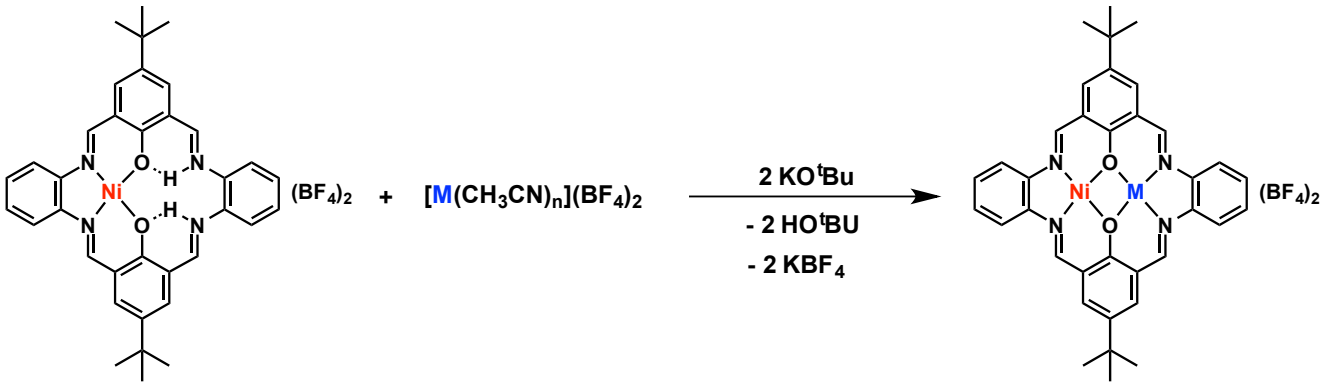

Successful attempts were made with M = Ni, Cu, while unsuccessful results were made with M = Co, Fe, Mn. It should be noted that efforts using $M(OAc)_2$ resulted with acetate bound across the metal centers, leading to dimerization, as shown in Figure A1. The complexes $[NiML^1](BF_4)_2$ (where M = Zn, Cu, Ni, Co, Fe, Mn) were characterized by ESI-MS, ^1H NMR, X-band EPR (when applicable), cyclic voltammetry, and magnetic moment measurements. X-ray crystallography and ESI-MS revealed two different outcomes following insertion of the second metal. When metal ionic radii are small (< 88 pm when high spin, octahedral geometry is considered), stoichiometric insertion is achieved.[107] This is shown with M = Cu and Ni (Figure 2.2, left). Attempts of insertion when the ionic radius is ≥ 88 pm results in a dimerized product. It is thought that the pocket size is too small for metals of this ionic radii, puckering the metal out of the pocket which is then stabilized by dimerization with a second deprotonated $[NiL^1]$ complex. This is observed with M = Fe and

Mn, as shown in Figure 2.2 (right). ^{1}H NMR of these complexes revealed that Ni retains a square planar geometry, resulting in a "diamagnetic" side of the complex.

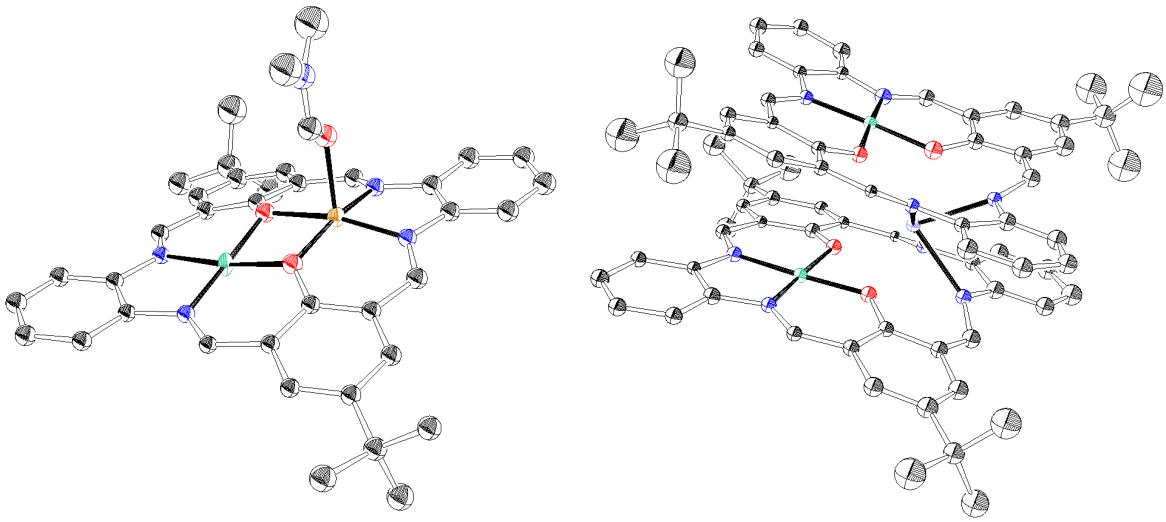

Figure 2.2. Ortep diagrams of (left) $[NiCuL^{1}](BF_4)_2$*DMF and (right) $\{[NiL^{1}]_2$-μ-Fe$\}(BF_4)_2$. Ellipsoids are shown at 50% probability. Uncoordinated solvent, hydrogens and BF_4 counter ions have been omitted for clarity. The ortep diagrams are with no anisotropy and shown only for structural representation.

The dimerization product is observed as the only product in ESI-MS as well (Figure A2). Synthesis using metals with ionic radii ≥ 88 pm give a characteristic *m/z* signal at ~641. This signal has a defined pattern of 0.5 mass-charge units, owing to the $M^{2+}/2$ ratio.

As mentioned before, it is thought that this dimerization is a direct result of the ionic radius of the second metal inserted. This difficulty in metallation of Robson-type ligands has been observed before by Okawa/Kida and others, whereby the authors increased the ligand flexibility by changing the diamine used in the synthesis. We chose to follow this method as well, which will be described below for ligands L^{2}-L^{4}.

Table 2.1. Magnetic data for select $[NiML^1](BF_4)_2$ complexes.

Complex	μ_{eff} / μ_B	g	S
$[NiCuL^1]^{2+}$	1.42	2.1	1/2
$[NiCoL^1]^{2+}$	3.69	4.3	3/2
$[NiFeL^1]^{2+}$	3.16	-	1

2.2 Synthesis and characterization of $[NiML^2]^{2+}$ complexes

The synthesis and characterization of ligands of the L^2 moiety are described below. 1,3-diaminopropane was used instead of *o*-phenylenediamine, where complexes with this linker have been shown to incorporate the larger metal ions such as Mn^{2+} and Fe^{2+}. The synthesis is analogous to the L^1 ligand described in Chapter 2.1.

Scheme 2.3. Synthesis of heterobimetallic complexes $[NiML^2](BF_4)_2$.

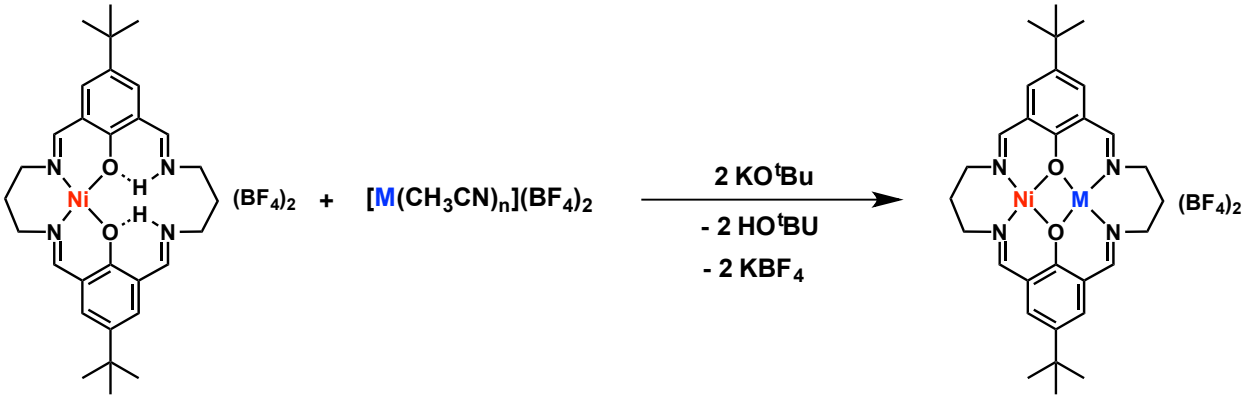

$[NiH_2L^2](BF_4)_2$ was synthesized in a similar manner to L^1, however some differences were observed. Contrary to L^1, $[NiH_2L^2](BF_4)_2$ did not retain a square planar geometry, resulting in a high spin complex. It has been reported that nickel complexes in

the L^2-type Robson macrocycle bind solvent in the axial positions, resulting in a square pyramidal or octahedral geometry with S = 1.[73,105] ^{1}H NMR revealed two broad resonances at 3.38, 6.68, and 12.18 ppm, corresponding to the uncoordinated, diamagnetic side of the complex (Figure 2.3). No resonances were observed beyond 15 ppm in the conditions used during the NMR experiment. ESI-MS displayed signals corresponding to both the mono-Ni complex and $[Ni_2L^2](BF_4)_2$, however, no homobimetallic impurities were observed in the ^{1}H NMR. Crystals suitable for X-ray analysis did not produce a quality structure, although we were able to confirm structurally that only a single nickel resided in the $[NiH_2L^2](BF_4)_2$ framework with acetonitrile ligands bound to Ni, resulting in a pseudo octahedral geometry.

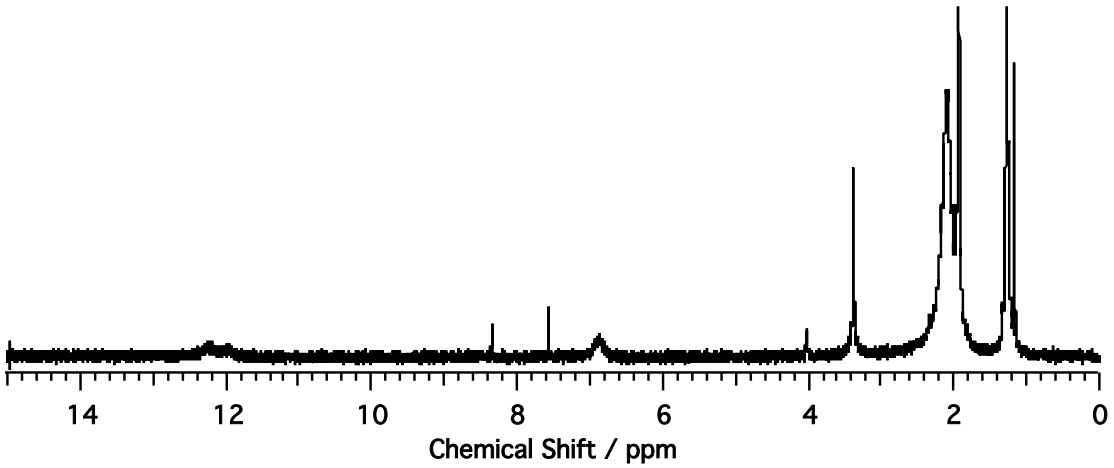

Figure 2.3. ^{1}H NMR of $[NiH_2L^2](BF_4)_2$ in d^6-DMSO.

Metallation of the second pocket site resulted in successful complexation via ESI-MS and X-ray crstallography. Some homobimetallic impurities were observed in mass spectrometry, although the extent of metal scrambling is not clear. Characterization proved unexpectedly difficult, with X-ray crystallography and elemental analysis unable to distinguish the homobimetallic and heterobimetallic purity, while the magnetic orbitals of

the now high spin Ni(II) allowed antiferromagnetic interactions with the second metal site, complicating characterization by magnetic methods. Cyclic voltammetry was therefore employed in an attempt to support the existence of the heterobimetallic species. The cyclic voltammograms are shown in Figure 2.4. It can be observed that the first cathodic process for all complexes listed are at similar potentials, which is likely the Ni(II/I) couple based on reports in literature, which will be described in more in detail in Chapter 3. As can be seen, $[NiCoL^2](BF_4)_2$ displays two cathodic events, the first at -1.44 V and the second at -1.61 V versus the ferrocene/ferrocinium couple, owing to the Ni(II/I) couple prior to the Co(II/I) couple.[100,104] No homobimetallic $[Ni_2L^2](BF_4)_2$ or $[Co_2L^2](BF_4)_2$ were observed in this cyclic voltammogram.

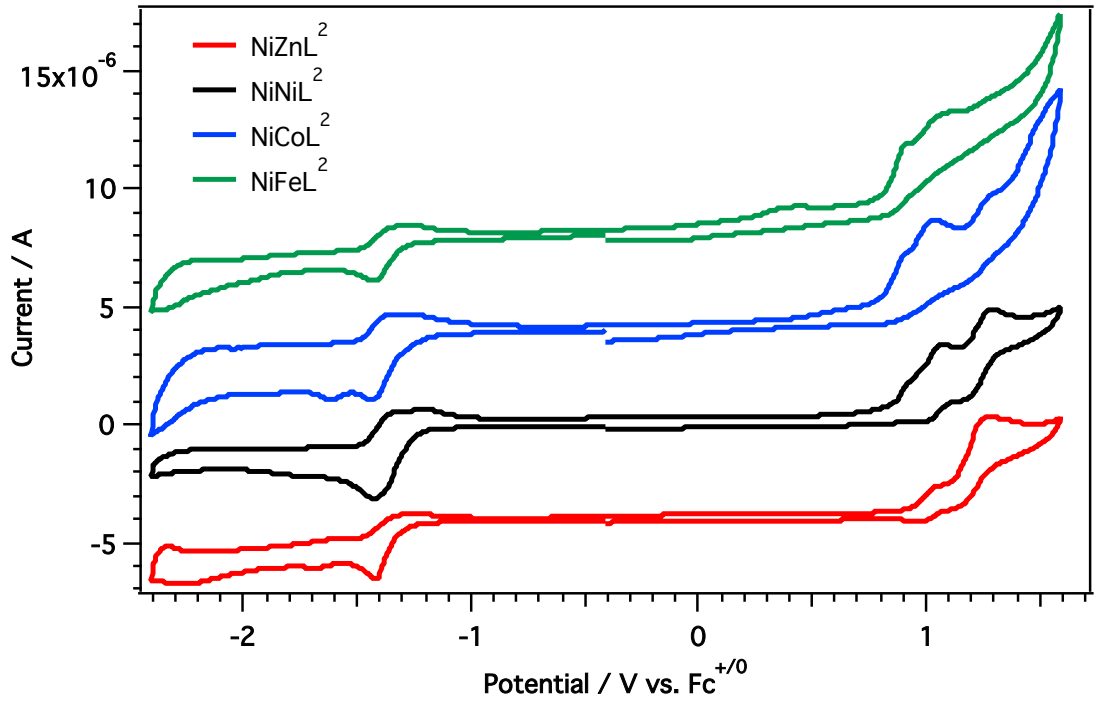

Figure 2.4. Cyclic voltammograms of $[NiML^2](BF_4)_2$ complexes. 2.0 mM complex in CH_3CN, 0.2 M Bu_4NPF_6, 100 mV/s scan rate.

Since characterization of these complexes remained challenging, the diamine used was changed from 1,3-diaminopropane to ethylenediamine. This has been shown to give

increased flexibility, presumably more than the phenylene linker, while maintaining a strong field ligand environment that keeps Ni(II) square planar, which would allow more facile characterization compared to the L^2 complexes.

2.3 Synthesis and characterization of $[NiML^3]^{2+}$ complexes

The synthesis of complexes with the ethylene linker are analogous to L^1 and L^2 complexes. Condensation using one equivalent of $[Ni(H_2O)_6](BF_4)_2$ again resulted in the mono-nickel complex $[NiH_2L^3](BF_4)_2$. Precipitation of orange microcrystals from ethanol gave the complex in 72% yield, with no further purification needed.

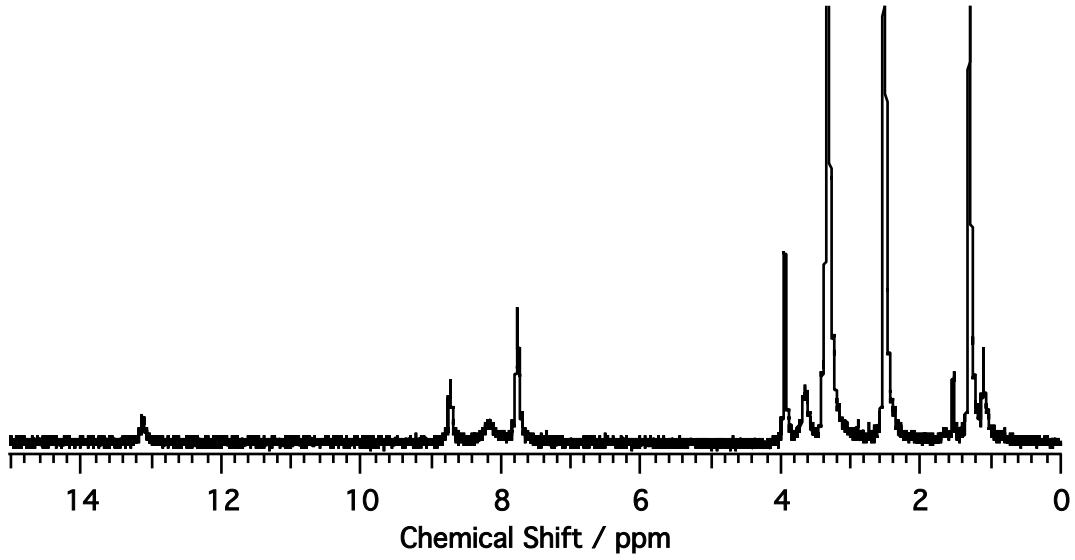

Figure 2.5. ^1H NMR of $[NiH_2L^3](BF_4)_2$ in d^6-DMSO.

Single crystals were isolated by vapor diffusion of diethyl ether into a DMF solution containing $[NiH_2L^3](BF_4)_2$. Each nickel site was disordered with 50% occupation by a Ni ion. This delocalization, along with ^1H NMR, ESI-MS confirmed the identity of the complex. It should also be noted that no homobimetallic complex was observed via ESI-MS.

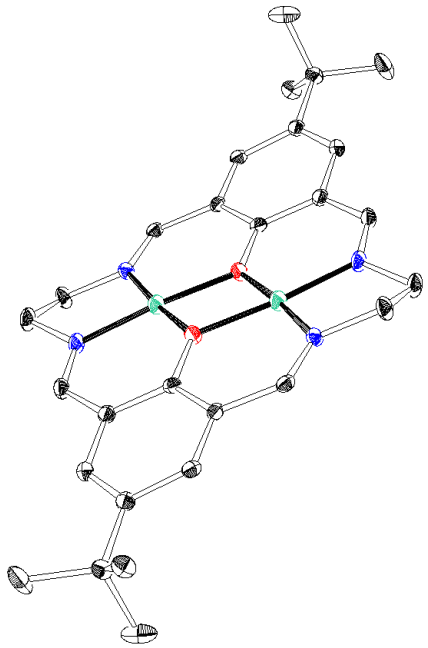

Figure 2.6. Ortep diagram of $[Ni_2L^3](BF_4)_2$. Ellipsoids are shown at 50% probability. Uncoordinated solvent, hydrogens, and BF_4 counter ions have been omitted for clarity.

Deprotonation with LiO^tBu in the presence of $M(BF_4)_2$ (where M = Zn, Cu, Ni, Co) resulted in the desired heterobimetallic complexes. LiO^tBu was used in place of KO^tBu to avoid KBF_4 impurities upon precipitation from ether. These complexes were isolated using ether diffusion into an acetonitrile solution containing the complex.

Scheme 2.4. Synthesis of heterobimetallic complexes $[NiML^3](BF_4)_2$.

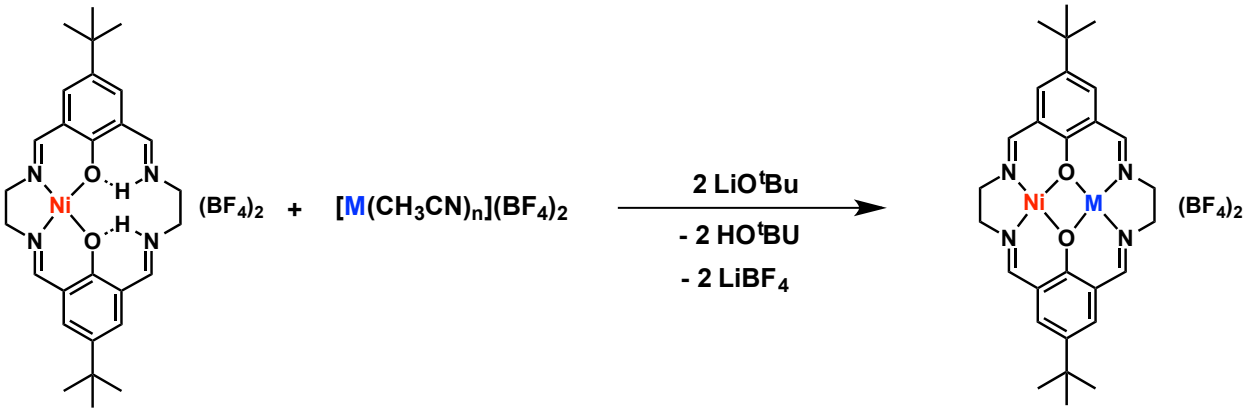

The complexes were characterized by X-ray crystallography, ESI-MS, ^{1}H NMR, cyclic voltammetry and elemental analysis. As can be observed, Ni(II) adopts a square planar geometry, resulting in a "diamagnetic" side of the complex. The second metal can be distinguished due to the adoption of a different geometry upon solvent binding in the axial positions, in contrast to L^2 complexes. This also results in simple paramagnets that can be more easily characterized compared to the L^2 macrocycle since no magnetic coupling occurs.

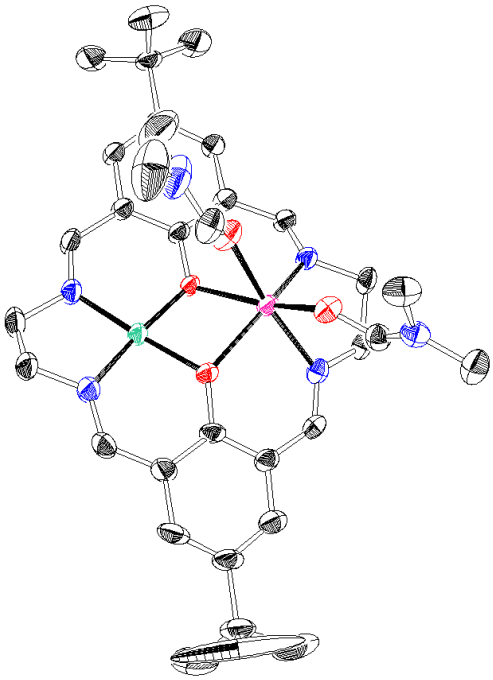

Figure 2.7. Ortep diagram of $[NiCoL^3](BF_4)_2$*DMF. Ellipsoids are shown at 50% probability. A second structure in the asymmetric unit along with uncoordinated solvent, hydrogens, and BF_4 counter ions have been omitted for clarity.

As can be seen from Figure 2.7, as the ionic radii increases, we still observe a puckering of the second metal. Insertion of Fe^{2+} and Mn^{2+} resulted in the dimerized product, similar to what was observed with L^1. This is evident by both ESI-MS and single crystal analysis, shown in Figure 2.8.

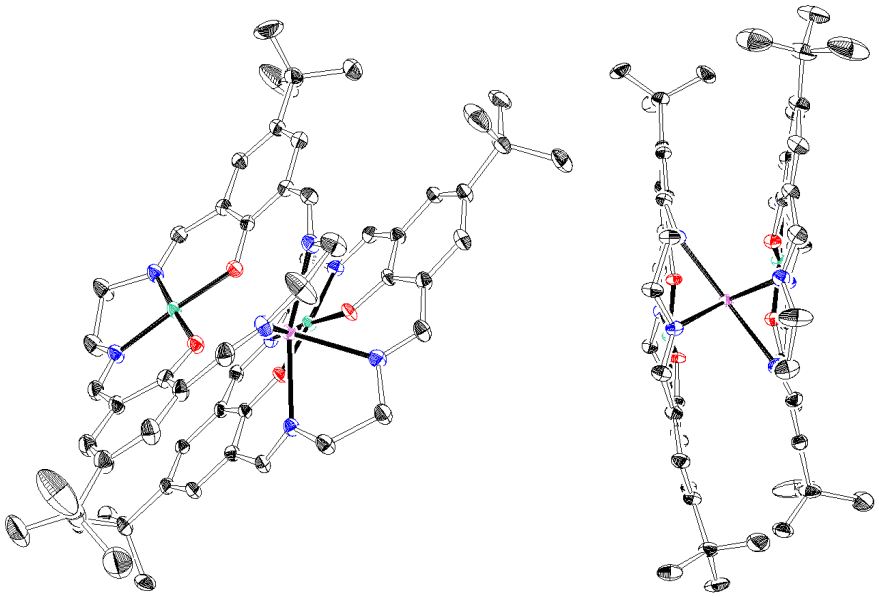

Figure 2.8. Ortep diagram of $\{[NiL^3]_2$-μ-Mn$\}(BF_4)_2$. Ellipsoids are shown at 50% probability. Uncoordinated solvent, hydrogens and BF_4 counter ions have been omitted for clarity.

Since the dimerization was still observed with the L^3 ligand, we decided to once again alter the diamine to provide enough flexibility for larger metals. This approach provides us with a few advantages: a) Ni is smaller and will remain on the ethylene side b) Ni will thus retain square planar geometry with no magnetic coupling c) the propylene side will be flexible enough to incorporate the larger metal ions such as Mn^{2+} and Fe^{2+}.

2.4 Synthesis and characterization of $[NiML^4]^{2+}$ complexes

As mentioned previously, Okawa/Kida developed a method around the same time as Robson to synthesize the heterobimetallic complexes with the same macrocycle. This was achieved using a step-wise synthesis. First, condensation of two equivalents of diformlyphenol with only one equivalent of ethylenediamine produces the ligand $L^{4'}$, or denoted by the authors as Fsal-2. Deprotonation and sequential metallation with $Ni(OAc)_2$

forms the complex $NiL^{4'}$. A second condensation with 1,3-diaminopropane forms the asymmetric NiL^4, shown in Scheme 2.5

Scheme 2.5. Synthesis of $[NiML^4](BF_4)_2$.

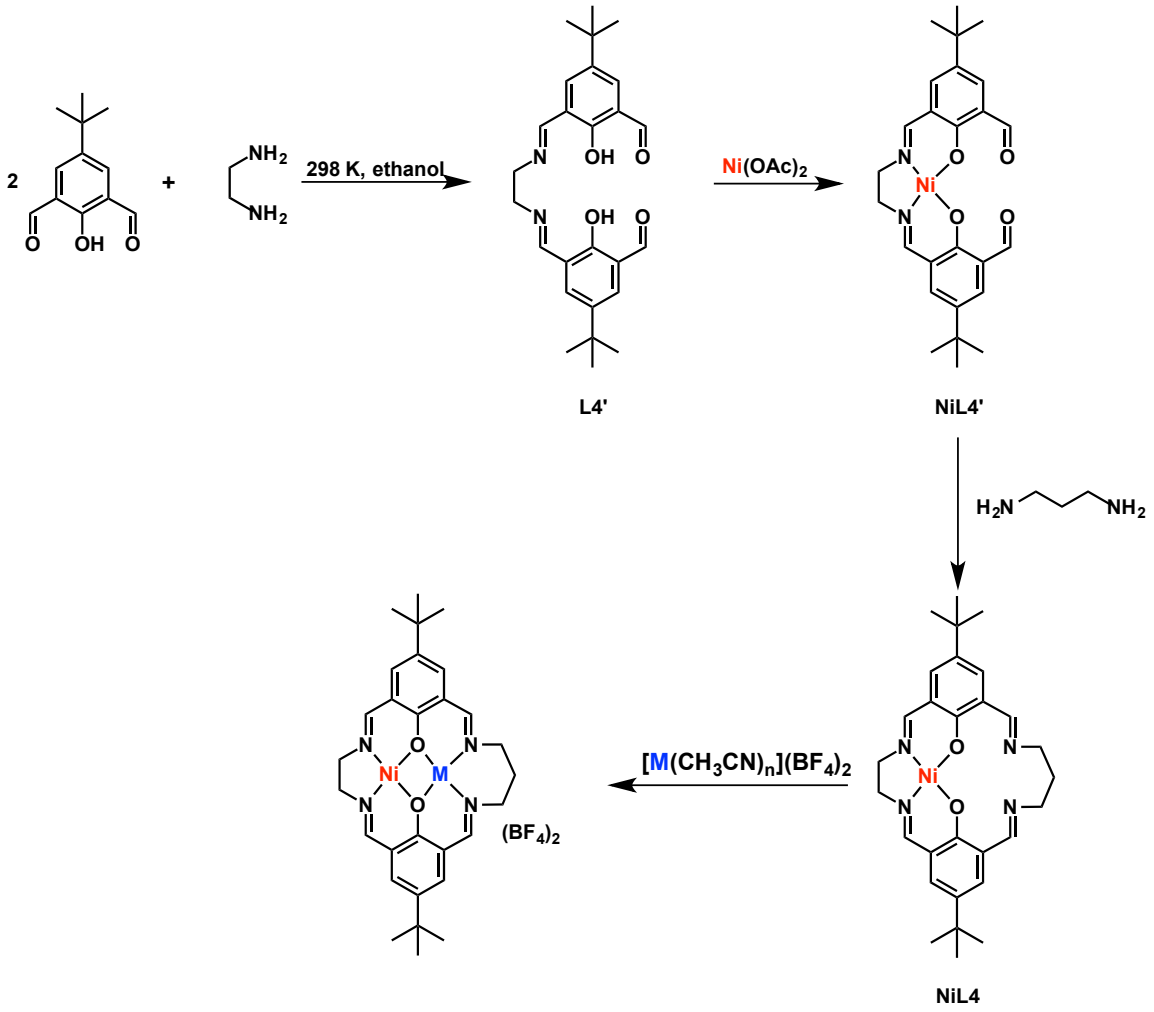

This step-wise synthesis can be monitored by ^1H NMR until insertion of the second metal ion, whereby the complex becomes paramagnetic. Ni(II) retains square planar geometry throughout the synthesis, similar to what was seen in the L^3 complexes, which allows more facile characterization. Condensation of 1,3-diaminopropane results in a loss of the aldehyde resonance at 10.5 ppm for $NiL^{4'}$, confirming the completion of the

macrocycle. Metallation of NiL^4 with $[Mn(CH_3CN)_4](BF_4)_2$ in dichloromethane yields a color change, with a precipitate formed upon addition of diethyl ether. Suitable crystals for X-ray analysis were not obtained and is still under investigation.

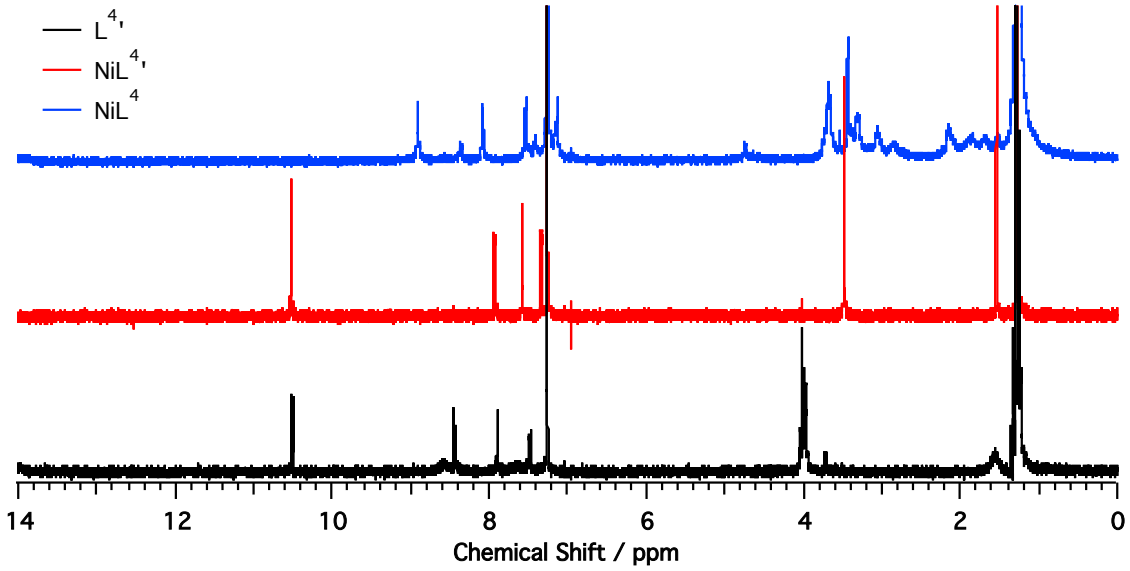

Figure 2.9. ^1H NMR following the synthesis of NiL^4 in CD_3Cl.

CHAPTER 3

Redox characterization of NiM bimetallic systems

3.1 Stability of Schiff-base macrocycle to acidic environments

Since reduction of CO_2 generally involves the presence of H^+, it was pertinent to examine the stability of these complexes in acidic environments. The ligand series described above contains four imines, brought together in a condensation reaction. Generally speaking, imines in the presence of acid reverses the condensation. This would be detrimental to the complex stability under CO_2 reduction conditions.

The diamagnetic complexes $[NiH_2L^1](BF_4)_2$ and $[NiH_2L^3](BF_4)_2$ were probed via ^1H NMR for decomposition in the presence of the acids $[NH_4][BF_4]$ (pK_a = 16.5 in CH_3CN, 10.5 in DMSO and c.a. 11.6 in DMF) and [HDBU][BF_4] (pK_a = 24.3 in CH_3CN, 12 in DMSO, c.a. 13.1 in DMF).[108-110] No noticeable changes were observed upon exposure to these acids within 24 h (Figure 3.1). Stronger acids, such as $[C_6H_5NH_3][BF_4]$ (pK_a = 10.6 in CH_3CN, 3.6 in DMSO, c.a. 5 in DMF) and [HDMF][BF_4] (pK_a = 6.10 in CH_3CN), result in decomposition as seen by ^1H NMR. $[NiCoL^3](BF_4)_2$, $[NiCuL^3](BF_4)_2$, $[Ni_2L^3](BF_4)_2$ also displayed no changes in the absorbance spectrum, indicating no decomposition in mild acidic conditions. It should be noted that exposure of the heterobimetallic complexes in the presence of strong acids such as anilinium or [HDMF][BF_4] replaces the non-Ni atom with H^+, supported by changes in the absorption spectrum. It is unclear of the extent of decomposition following demetallation when stoichiometric amounts of strong acid are added.

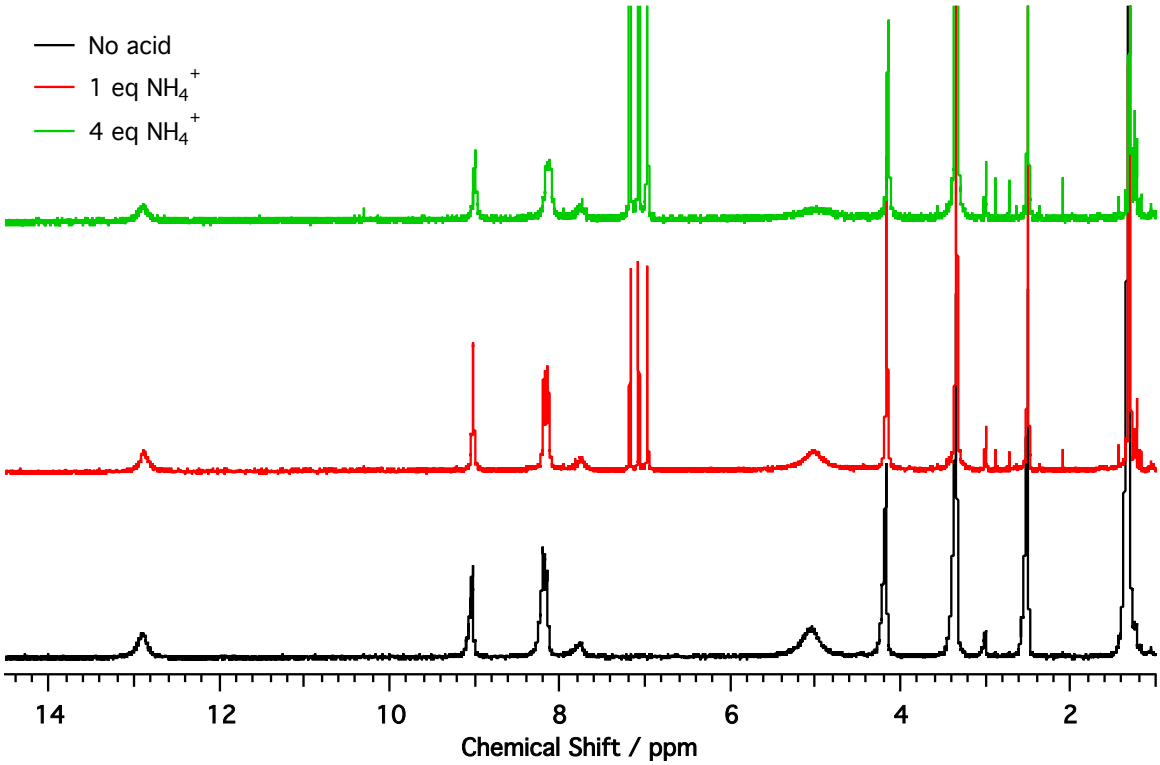

Figure 3.1. ^{1}H NMR probing the acid stability of $[NiH_2L^3](BF_4)_2$ in d^6-DMSO. $[NH_4][BF_4]$ added and the solution was allowed to come to equilibrium for 24 hr.

3.2 Spectroscopic determination of $[NiML]^+$ species

As mentioned, the complexes are designed to be electrocatalysts for reduction processes. The initial method use to probe interaction with CO_2 was monitored by cyclic voltammetry. The complexes described in Chapter 2 all display cathodic waves in the CV, indicative of reduction of the complex. It is desirable then to identify what occurs upon reduction. All of the complexes described contain not only redox-active metals, but also redox-active ligands.[93,95,111] In order to understand the reductive behavior, we used Ni(salen) as a control since it contains a similar ligand field while having a known Ni(II/I) reduction. The identification of the Ni(salen) family has been established in the literature

producing mixed results.[112,113] [Ni(salen)]$^-$ has been identified containing a Ni(I) center, which displays a rhombic signal with g values of 2.25, 2.08, and 2.04 (DMF) in X-band EPR, while also giving rise to d-d transitions at 806 nm and 637 nm.[114] This d-d band structure has been shown in the literature to describe the axial distortion from a d^9 Ni(I) species by comparison to the isoelectronic Cu(salen)-type systems. The band shown in Figure 3.4 (right) is actually comprised of three features that are close in energy. The transitions are assigned as $d_{xy} \rightarrow d_{x^2-y^2}$, $d_{z^2} \rightarrow d_{x^2-y^2}$, and d_{xz}, $d_{yz} \rightarrow d_{x^2-y^2}$.

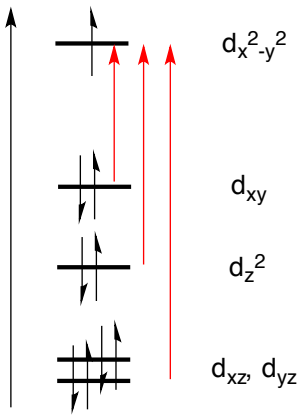

Figure 3.2. d-orbital splitting and transitions for axially distortedd Ni(I) species. Allowable transitions shown with red arrows.

Conversely, Ni(salp)$^-$, which contains a phenyl linker, gives drastically different results. Upon reduction, Ni(salp)$^-$ gives rise to a pseudo isotropic signal with a g = 2.01 (DMF) and transitions in the visible spectrum at 622 nm and 462 nm. It is thought that this reduction generates a radical, not Ni(I), and that at low temperatures remains monomeric Ni(II) while at room temperature dimerizes to $[Ni(salp)_2]^{2-}$. This difference observed upon reduction with similar ligands shows the importance of understanding the redox processes of the complexes we are studying. In addition to distinguishing the difference between

Ni(II/I) and ligand reductions, many of the bimetallic complexes contain redox-active metals that must be identified as well.

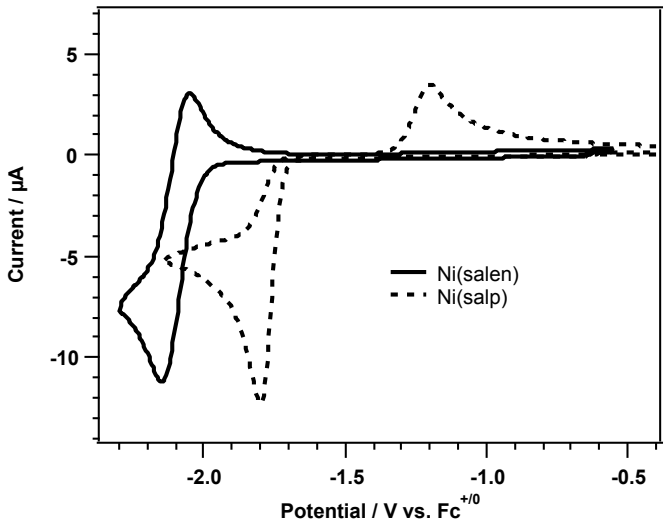

Figure 3.3. Cyclic voltammograms of Ni(salen) (solid line) and Ni(salp) (dashed line). 0.2 M Bu_4NPF_6 in DMF, 100 V/s scan rate.

In this section, the complexes will be separated into two sections: those containing one redox active metal and those containing two redox active metals. The ligand framework does not appear to affect the redox processes and will not be separated from one another to describe the system.

The cyclic voltammogram of Ni(salen) displays a scan rate-dependent, reversible couple at -2.11 V vs. $Fc^{+/0}$ with ΔEp = 99.6 mV. Chemical (or electrochemical) reduction using one equivalent of potassium graphite results in a color change from orange to dark brown, with absorption bands shown in Figure 3.4. X-band EPR displays a rhombic signal with the same g-values described in the literature.

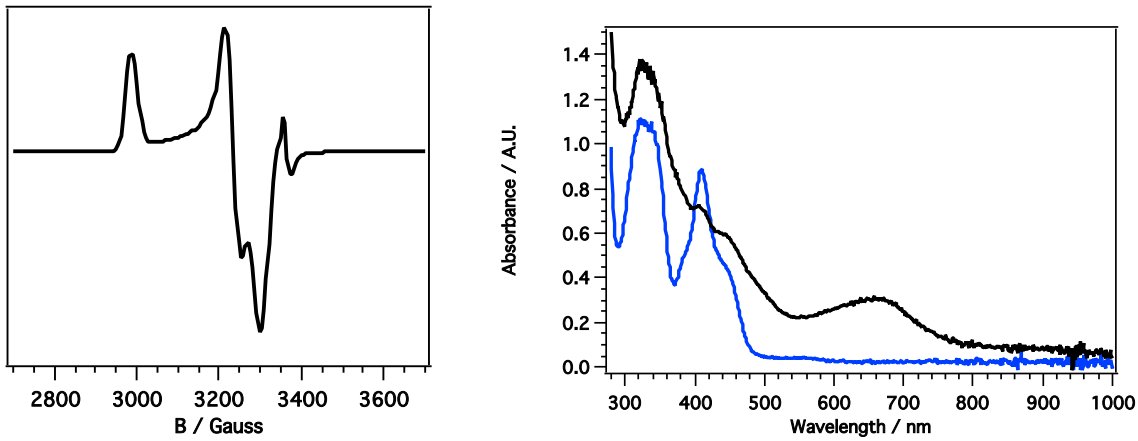

Figure 3.4. (Left) EPR spectrum of Ni(salen)$^{-}$ at 77 K. 1e^{-} reduced species was prepared by addition of 1 eq KC_8 in DMF. 2.0 mM in DMF/THF (1:1). (Right) Absorption spectrum of Ni(salen)$^{-}$ (black) and Ni(salen) (blue). Potential held at -2.2 V vs. $Fc^{+/0}$, 50 μM, 0.2 M Bu_4PF_6 in DMF.

Knowing that a Ni(II/I) reduction of salen complexes results in the spectra described above, we decided to look at the characteristics of the reduced NiH_2L products to understand the nature of the reduced species. $[NiH_2L^1](BF_4)_2$ displays a cathodic wave similar to Ni(salp) but at c.a. 800 mV more positive. The reduction of Ni(salp) gives rise to a cathodic wave at -1.86 V, with a distinct anodic feature at -0.94 V, much too far positive to be related to a simple reoxidation event. This is likely due to the oxidation of the dimer complex formed upon ligand reduction. $[NiH_2L^1](BF_4)_2$ displays similar characteristics with cathodic features at -1.08 V and -2.00 V, with a separated anodic event at -0.49 V.

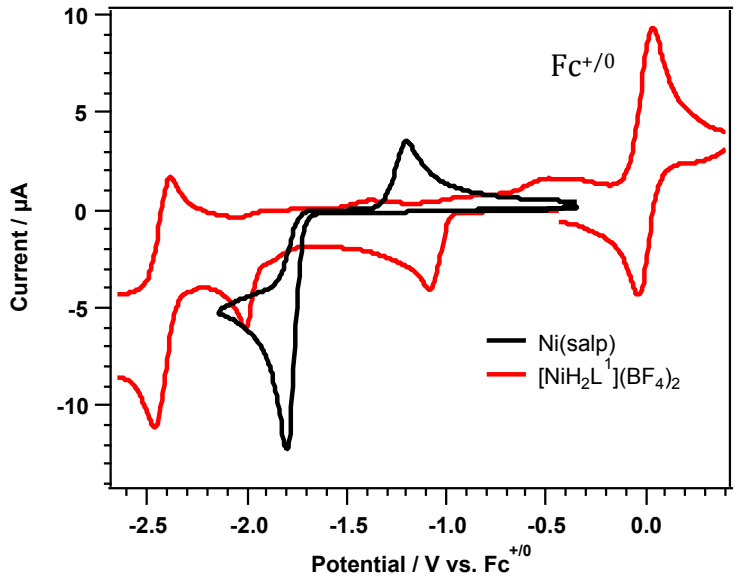

Figure 3.5. Cyclic voltammogram of Ni(salp) (black) and $[NiH_2L^1](BF_4)_2$ (red). 2.0 mM complex, 0.2 M Bu_4NBF_4 in DMF, 100 mV/s scan rate.

The EPR of the chemically reduced species features an isotropic signal at g = 2.0 with no observed hyperfine at 77 K. Spectroelectrochemical reduction to the $1e^-$ reduced species did not result in the low energy d-d band associated with Ni(II/I), but rather a growth of in the $\pi \rightarrow \pi^*$ region of the spectrum, likely due to ligand reduction.

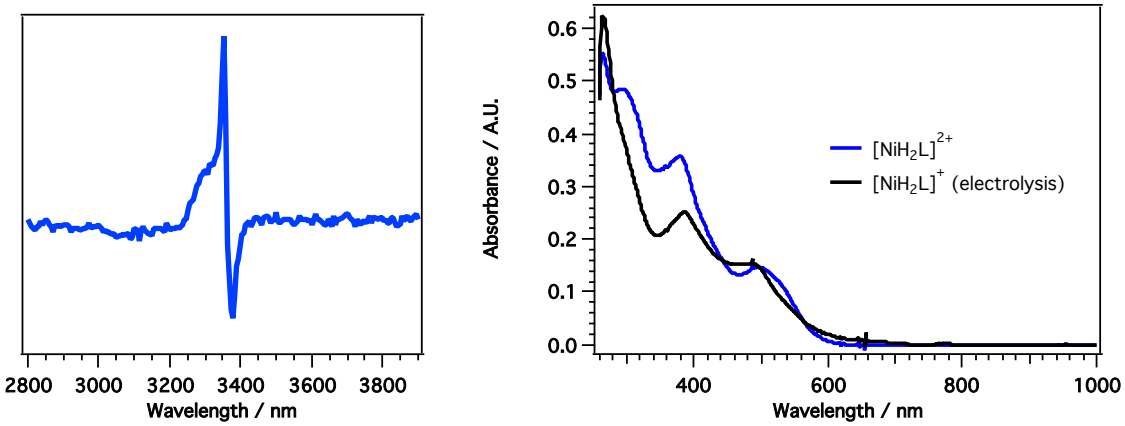

Figure 3.6. (Left): EPR spectrum of $[NiH_2L^1]^+$ at 77 K. $1e^-$ reduced species was prepared by addition of 1 eq KC_8 in DMF/THF (1:1). (Right): Absorption spectrum of $[NiH_2L]^+$ (black) and $[NiH_2L^1]^{2+}$ (blue). Potential held at -1.2 V vs. $Fc^{+/0}$, 50 µM, 0.2 M Bu_4PF_6 in DMF.

Reduction of $[NiH_2L^3](BF_4)_2$ also does not display the Ni(II/I) characteristics seen in Ni(salen). Two irreversible cathodic events at -1.41 and -1.65 V are observed in the cyclic voltammogram of $[NiH_2L^3]^{2+}$. The EPR spectrum of the $1e^-$ reduced species give an isotropic signal at g = 2.0 with no observable. SEC-UV-Vis displays a shoulder upon reduction in the $\pi \rightarrow \pi^*$ region, similar to what was observed for $[NiH_2L^1]^{2+}$.

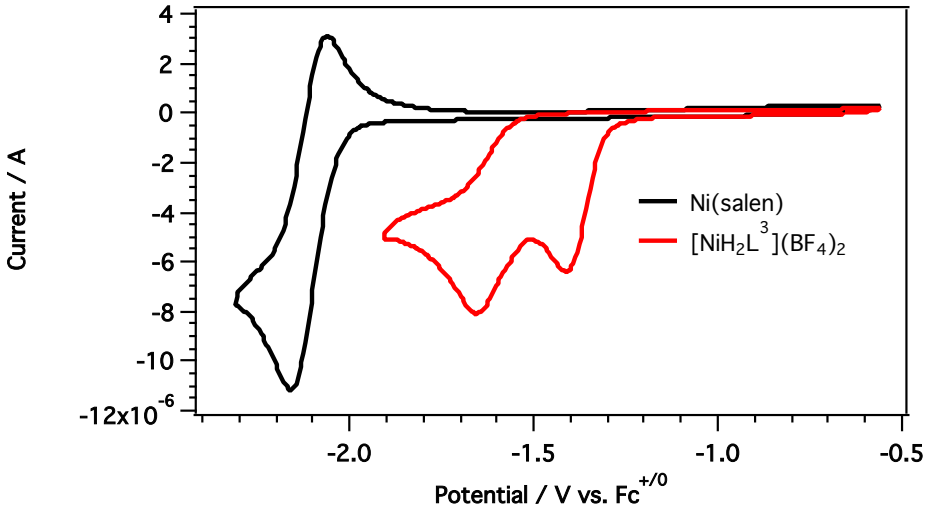

Figure 3.7. Cyclic voltammograms of Ni(salen) (black) and $[NiH_2L^3](BF_4)_2$ (red). 2.0 mM sample, 0.2 M Bu_4NPF_6 in DMF, 100 mV/s scan rate.

The reduction of both $[NiH_2L^1](BF_4)_2$ and $[NiH_2L^3](BF_4)_2$ do not display the characteristics of Ni(I) as seen in Ni(salen) but more closely resemble the features seen in Ni(salp). It is likely that the reduction of the $[NiH_2L]^{2+}$ complexes does not happen at the metal center, but on the ligand, which is influenced by the phenolic protons in the second pocket.

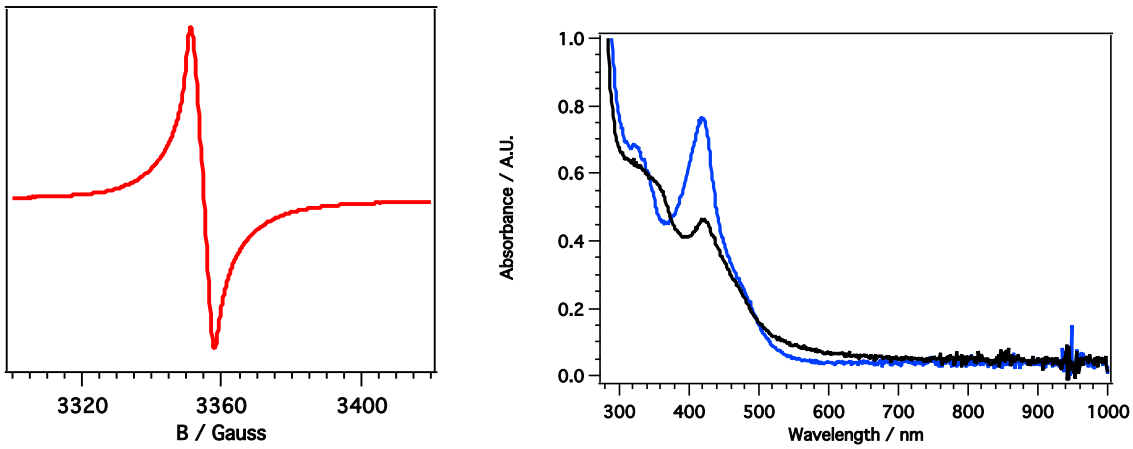

Figure 3.8. (Right): EPR spectrum of $[NiH_2L^3]^+$ at 77 K. 1e- reduced species was prepared by addition of 1 eq KC_8 in DMF/THF (1:1). (Left): Absorption spectrum of $[NiH_2L^3]^+$ (black) and $[NiH_2L^3]^{2+}$ (blue). Potential held at -1.5 V vs. $Fc^{+/0}$, 50 μM, 0.2 M Bu_4PF_6 in DMF.

The bimetallic complexes $[NiML]^{2+}$ present more difficulty with regards to characterizing the intermediates. Reduction of Ni(II) to Ni(I) generates a magnetic orbital for which a paramagnetic metal can then couple to. This is generally the case for these complexes, resulting in antiferromagnetic coupling through the phenoxo bridge. Since magnetic coupling makes EPR characterization difficult, the absorption spectrum can then be used to help identify the reduced species. The absorption features seen in Ni(salen) have also been observed by Okawa for $[NiMnL^4]^+$, which gives us a method for assigning Ni(II/I) couples.[100,104] Unlike the $[NiH_2L]^{2+}$ complexes, reduction of the complexes $[NiML^n]^{2+}$ complexes (where n = 1,3 and M = Ni, Co, Fe) resemble Ni(II/I) reductions. As can be seen in Figure 3.9, $[Ni_2L^3]^{2+}$ and $[NiCoL^3]^{2+}$ have reversible couples at -1.20 V and -1.24 V, respectively, while $[Ni_2L^3]^{2+}$ has a second, irreversible couple at -1.52 V and $[NiCoL^3]^{2+}$ has a quasireversible couple at -1.65 V. Reduction of each complex by $1e^-$ generates a low energy d-d band, similar to what is observed for Ni(salen). The reduction of $[NiCoL^2](BF_4)_2$

has been described in this same manner, with the first reduction corresponding to $Ni^{I}Co^{II}$ and the second reduction as the $Ni^{I}Co^{I}$ species.[100,104]

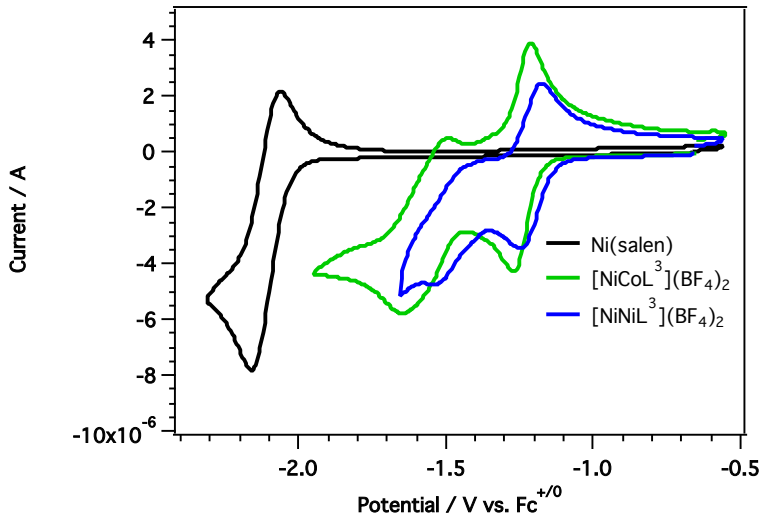

Figure 3.9. Cyclic voltammograms of $[NiML^3](BF_4)_2$ {M = Co (green), Ni (blue)}. 2.0 mM complex, 0.2 M Bu_4NPF_6 in DMF, 100 mV/s scan rates.

This d-d band was also observed upon the reduction of $\{[NiL^1]_2\text{-}\mu\text{-}Fe\}^{2+}$ and $\{[NiL^1]_2\text{-}\mu\text{-}Co\}^{2+}$ at the first reduction potential. The similarities in reduction potential as well as the appearance of the d-d band may indicate that the first reduction is likely the Ni(II/I) couple.

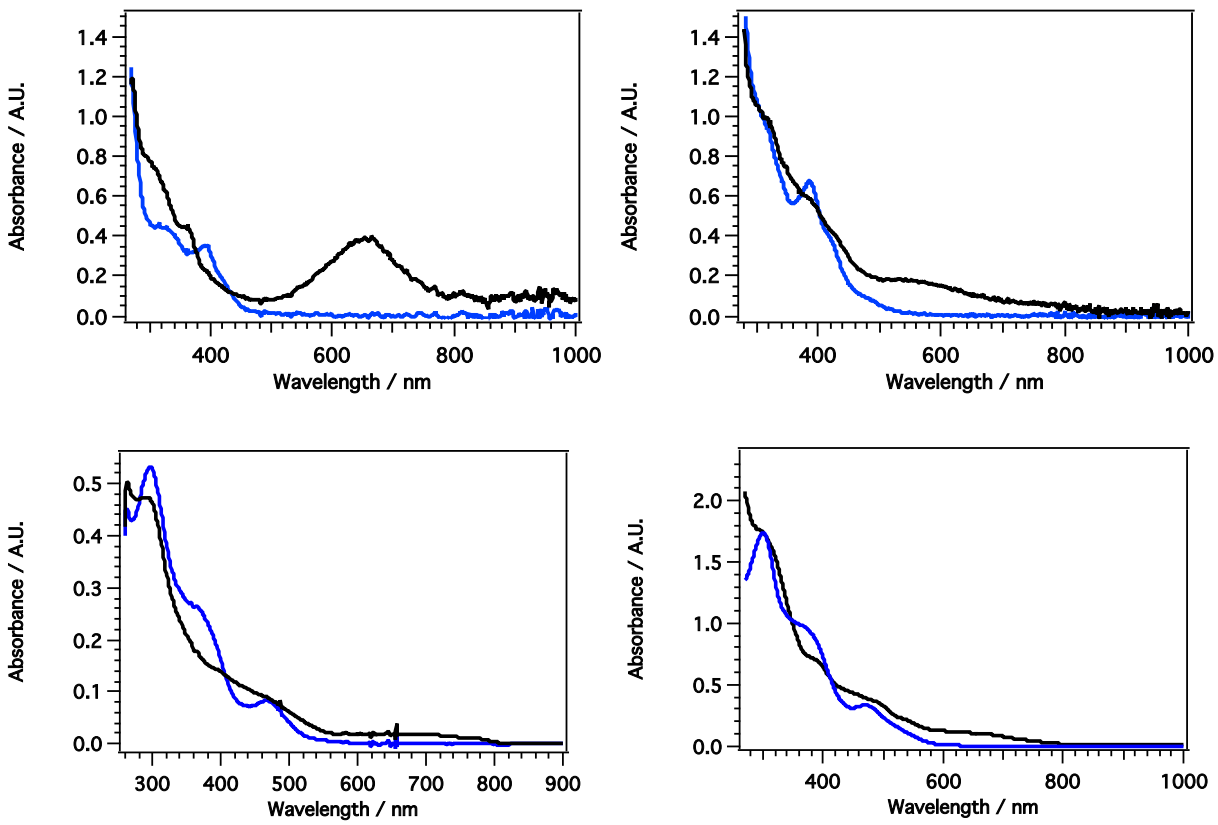

Figure 3.10. (Top left): Absorption spectrum of $[NiCoL^3]^+$ (black) and $[NiCoL^3]^{2+}$ (blue). (Top right): Absorption spectrum of $[Ni_2L^3]^+$ (black) and $[Ni_2L^3]^{2+}$ (blue). (Bottom left): Absorption spectrum of $\{[NiL^1]_2\text{-}\mu\text{-}Fe\}^+$ (black) and $\{[NiL^1]_2\text{-}\mu\text{-}Fe\}^{2+}$ (blue). (Bottom right): Absorption spectrum of $\{[NiL^1]_2\text{-}\mu\text{-}Co\}^+$ (black) and $\{[NiL^1]_2\text{-}\mu\text{-}Co\}^{2+}$ (blue). Potentials held at past the first reduction potential vs. $Fc^{+/0}$, 50 μM, 0.2 M Bu_4PF_6 in DMF.

CHAPTER 4

Interaction with CO_2

4.1 Influence of Na^+ on Co(salen)

It has been observed since the 1980's that the Co(salen) family, upon reduction in the presence of alkali metals, can bind and reduce carbon dioxide by two electrons to carbon monoxide, albeit at low turnovers.[12,68-71] Figure 4.1 shows the cyclic voltammograms of Co(salp) in the presence of CO_2 and acid. It is observed that minimal changes occur with CO_2 alone, and that addition of acid results in a positive shift in the first reduction with a slight increase in current. This is attributed to H^+ reduction, which is known to occur. However, with the introduction of Na^+, a new cathodic wave arises which has been reported to be the reduction of the bicarbonate bound intermediate (see Figure 1.13).[12] Again, there is a large current increase in the presence of H^+, indicative of H_2 production with small amounts of CO_2 reduction. Ni(salen) and Ni(salp) do not show interactions with CO_2 with or without the presence of alkali metals.

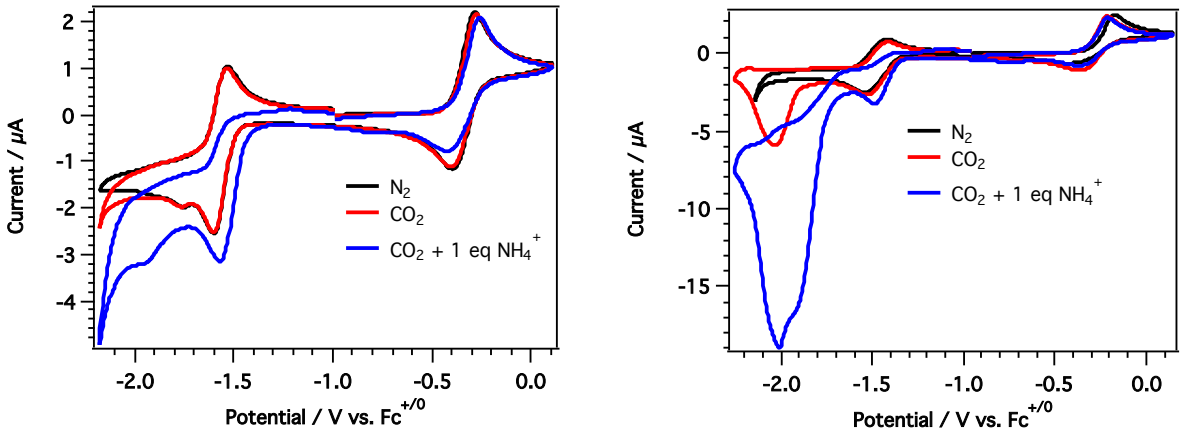

Figure 4.1. (Left): Cyclic voltammogram of Co(salp) under CO_2 in the absence of Na^+. 0.2 M Bu_4NPF_6 in DMF, 100 mV/s scan rate. NH_4^+ = $[NH_4][BF_4]$ (Right): Cyclic voltammogram of Co(salp) under CO_2 in the presence of Na^+. 0.2 M $NaPF_6$ in DMF, 100 mV/s scan rate.

4.2 Interactions of $[NiML^1](BF_4)_2$ with CO_2

Complexes with L^1 ligands displayed some interaction with CO_2. Of note are the complexes $\{[NiL^1]_2\text{-}\mu\text{-}Co\}(BF_4)_2$ and $\{[NiL^1]_2\text{-}\mu\text{-}Fe\}(BF_4)_2$, shown in Figure 4.2. Our interest in $\{[NiL^1]_2\text{-}\mu\text{-}Fe\}(BF_4)_2$ was due to the elemental similarity to CODH II, where no synthetic NiFe bimetallic complex has displayed reactivity with CO_2 or CO.[115-119] Cyclic voltammograms of $\{[NiL^1]_2\text{-}\mu\text{-}Fe\}(BF_4)_2$ in DMF displayed an irreversible cathodic event at -1.38 V. Upon exposure to carbon dioxide, no current increase is seen at this potential; however, an onset increase in current occurs at potentials past the first reduction event. This displays scan rate dependent behavior, with onset potentials becoming more positive as the scan rate is decreased (Appendix Figure A5). This scan rate dependent behavior is also seen in $\{[NiL^1]_2\text{-}\mu\text{-}Co\}(BF_4)_2$ at approximately the same potential. It should be noted that increases in current beyond -1.9 V were not investigated due to direct reduction of CO_2 on the glassy carbon working electrode in DMF.

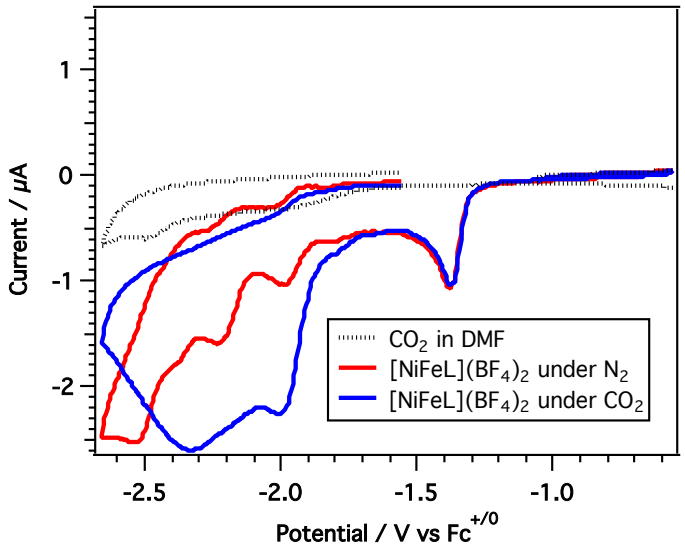

Figure 4.2. Cyclic voltammogram of $\{[NiL^1]_2\text{-}\mu\text{-}Fe](BF_4)_2$ under CO_2. 2.0 mM complex, 0.2 M Bu_4NBF_4 in DMF, 25 mV/s. Interaction of CO_2 on a glassy carbon electrode in the absence of complex shown in dotted black line.

$[NiH_2L^1](BF_4)_2$ and $[NiZnL^1](BF_4)_2$ also showed onset current increases in the presence of CO_2, though at more negative potentials (Appendix Figure A8 & A10). This too showed scan rate dependent behavior, with $[NiH_2L^1](BF_4)_2$ showing only slightly more positive onset potentials at slow scan rates (< 25 mV/s) and $[NiZnL^1](BF_4)_2$ showing modest potential shifts.

These results were corroborated using bulk chemical reduction and spectroelectrochemistry to monitor the reaction with CO_2 by molecular spectroscopy. Holding the potentials past the first cathodic event generates the $1e^-$ reduced product, whereby introduction of CO_2 induces change in the absorption spectrum shown Figure 4.3.

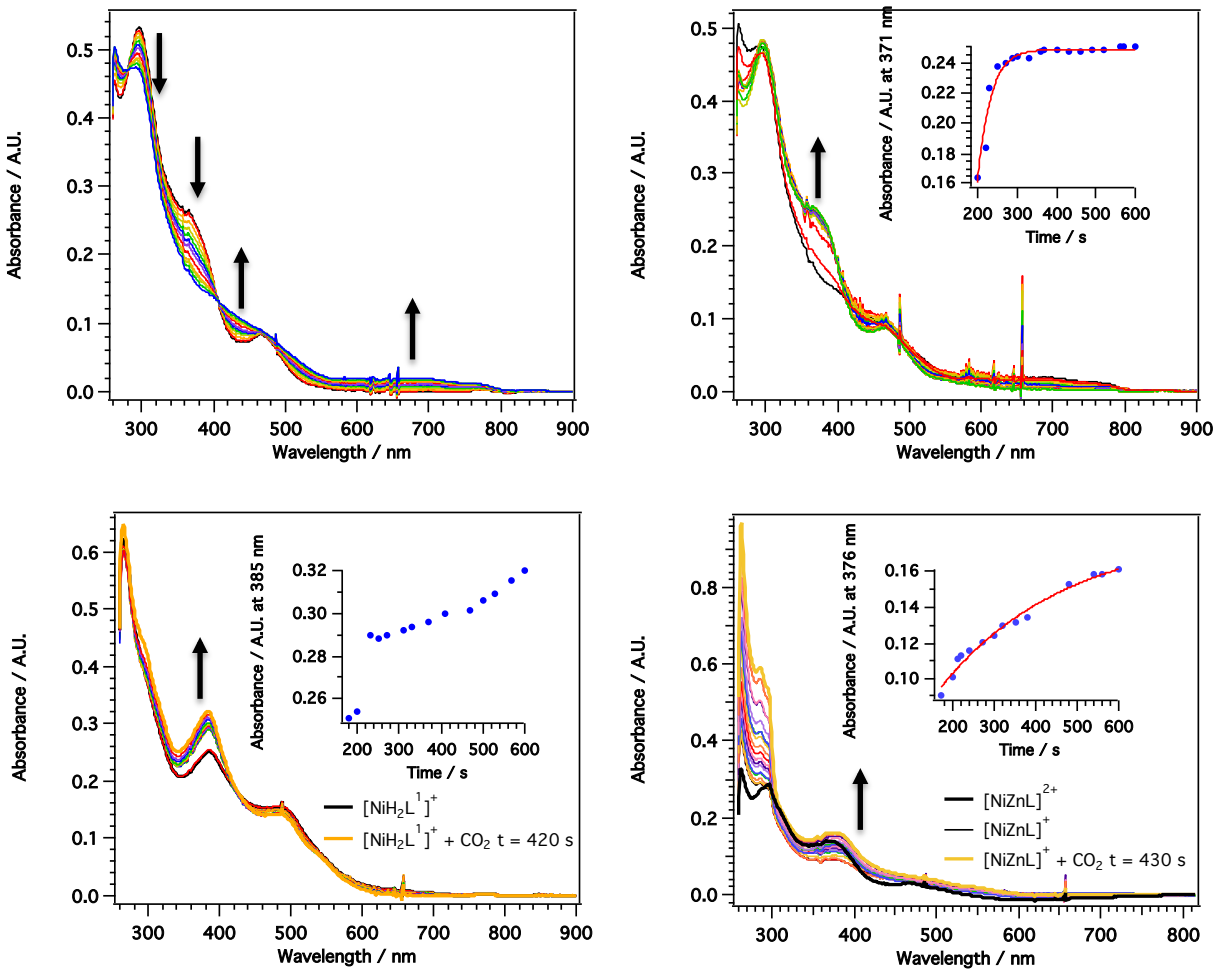

Figure 4.3. (Top left): Electrolysis of $\{[NiL^1]_2\text{-}\mu\text{-}Fe\}^{2+}$. Potential held at -1.6 V vs. $Fc^{+/0}$. 0.2 M Bu_4NBF_4 in DMF under Ar. (Top right): Addition of CO_2 to electrolyzed $\{[NiL^1]_2\text{-}\mu\text{-}Fe\}^{+}$. *Inset*: time vs. absorbance at 371 nm after the addition of CO_2. (Bottom left): Addition of CO_2 to electrolyzed $[NiZnL^1]^{+}$. *Inset*: time vs. absorbance at 385 nm after the addition of CO_2. (Bottom right): Addition of CO_2 to electrolyzed $[NiH_2L^1]^{+}$. *Inset*: time vs. absorbance at 376 nm after the addition of CO_2.

Although these results indicate an interaction with CO_2, no CO was detected during bulk electrolysis. This could be explained by the structure of the complexes. As stated throughout the text, we believe that CO_2 reduction is facilitated by cooperation among the metal ions. With respect to the structure shown in Figure 2.2, a cooperative interaction between the Ni and Fe ions of $\{[NiL^1]_2\text{-}\mu\text{-}Fe\}(BF_4)_2$ is not likely unless the complex

dissociates upon reduction. It is due to this structural interference that we pursued complexes containing the L^2 ligand to avoid the hindrance made by complex dimerization.

4.3 Interactions of $[NiML^2](BF_4)_2$ with CO_2

Of the complexes containing the L^2 ligand, $[NiCoL^2](BF_4)_2$ displayed the most promising results. The cyclic voltammogram of $[NiCoL^2](BF_4)_2$ contains two quasireversible reduction events at -1.41 V and -1.59 V pertaining to the Ni(II/I) couple and Co(II/I) couple, respectively.[100] Introduction of carbon dioxide does not result in a current increase, but perturbations in the cyclic voltammogram are observed. A reductive event at -1.79 V appears, while the anodic wave associated with Co(I/II) couple disappears. Introduction of a protic source, $[NH_4][BF_4]$ induces a large current increase with an onset potential of -1.4 V. The maximum current starts at -1.61 V and increases linearly with the concentration of H^+, plateauing at a maximum current at -1.82 V, shown in Figure 4.4.

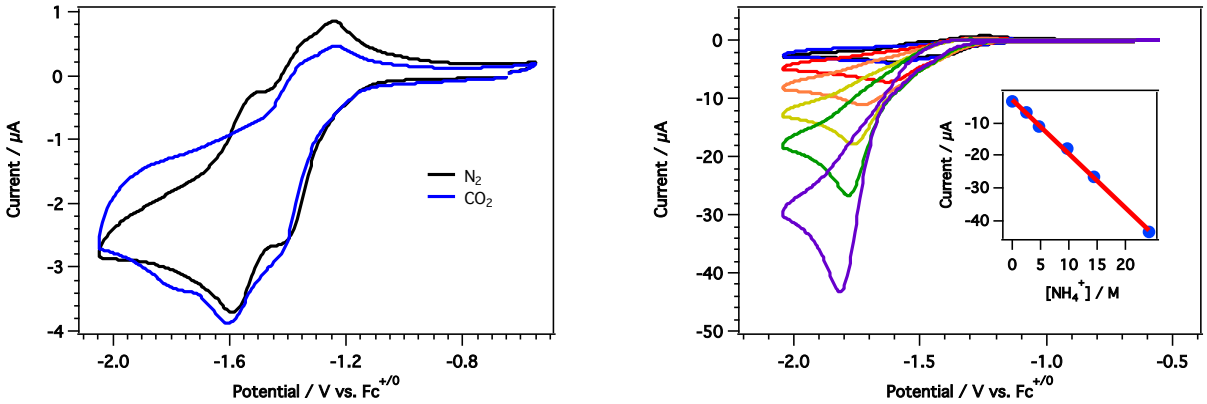

Figure 4.4. (Left): Cyclic voltammogram of $[NiCoL^2](BF_4)_2$ under N_2 (black) and CO_2 (blue). 0.2 M Bu_4NPF_6 in DMF, 25 mV/s. (Right): Cyclic voltammogram of $[NiCoL^2](BF_4)_2$ under N_2 (black), CO_2 (blue), and increasing equivalents of $[NH_4][BF_4]$ (red-purple). *Inset*: Current vs. $[H^+]$ for the addition of $[NH_4][BF_4]$.

Introduction of protic sources in the absence of CO_2 likewise results in an increase in current. Figure 4.5 illustrates this; however, after 2 equivalents of acid have been added, the addition of CO_2 still produces an increase in current. Furthermore, the reversibility of the Co(II/I) couple diminishes only in the presence of both H^+ and CO_2, indicating catalytic behavior.

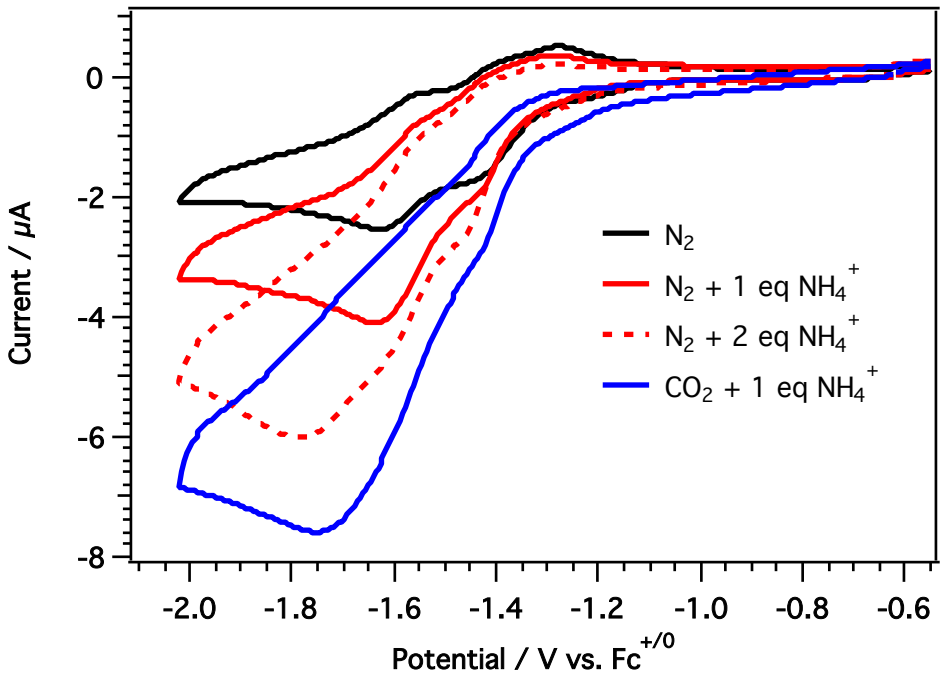

Figure 4.5. Cyclic voltammogram of $[NiCoL^2](BF_4)_2$ under N_2 (black), 1-2 equivalents of $[NH_4][BF_4]$ under N_2 (red), and the addition of CO_2 (blue). 0.2 M Bu_4NPF_6 in DMF, 25 mV/s.

Attempts to characterize the intermediates formed upon electrocatalysis did not yield carbonyl stretches in the IR. CO_2 is known to reduce on Pt electrodes at -1.7 V vs. $Fc^{+/0}$ to carbonate, with stretching frequencies around 1650 cm^{-1}, while the other product CO is not seen due to the cell used, so care must be used in interpretation of SEC-IR results.[11,120] Bulk electrolysis was run at potentials held past the first and second reduction potential at -1.4 and -1.65 V, respectively. Large amounts of hydrogen were detected via gas chromatography, indicating that the catalysis observed during cyclic voltammetry is a

result of H^+ reduction to H_2; no carbon monoxide was detected. FT-IR of the sample following electrolysis did not result in the detection of carbonyl stretches.

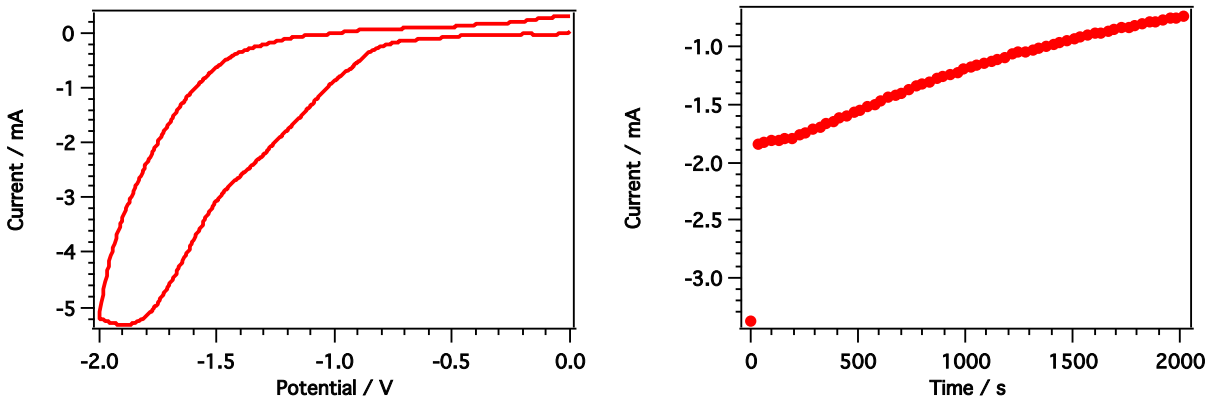

Figure 4.6. (Left): Cyclic voltammogram of $[NiCoL^2](BF_4)_2$ before electrolysis. 1.0 mM complex, 0.2 M Bu_4NPF_6 in DMF, 2.0 mM $[NH_4][BF_4]$, 100 mV/s. (Right): Time vs. current of $[NiCoL^2](BF_4)_2$ during electrolysis.

It has been mentioned that of the complexes containing the L^2 ligand, only $[NiCoL^2](BF_4)_2$ displayed promising cyclic voltammograms in the presence of CO_2. It should be noted that similar complexes, such as $[NiFeL^2](BF_4)_2$ showed only subtle changes in the reversible behavior upon the introduction of CO_2; however, in the presence of acid, the only activity that was observed is likely due to H^+ reduction (Figure A14).

4.4 Interactions of $[NiML^3](BF_4)_2$ with CO_2

Complexes containing the L^3 ligand did not show promising behavior for reduction of CO_2. Introduction of CO_2 into solutions containing $[NiML^3](BF_4)_2$, such as $[NiCoL^3](BF_4)_2$, did not show features in the cyclic voltammogram indicative of interaction. Addition of $[NH_4][BF_4]$ resulted in a current increases beyond the Co(II/I) couple. Activity with protons under inert atmosphere was noticed, however, the sample displayed crossover behavior in the cyclic voltammogram under these conditions. Interestingly, the addition of carbon

dioxide caused the crossover event to be noticeably absent, indicating possible interference/reaction with CO_2 in protic conditions. This possible interaction of CO_2 with these complexes remains undetermined.

CHAPTER 5

Summary and Conclusions

Our aim was to develop bimetallic complexes that acted in a way similar to CODH II that work cooperatively to reduce carbon dioxide by $2e^-$. The complex design was influenced by the Co(salen) system, utilizing a Robson-type macrocycle to bring two metal ions into close proximity that could be tuned to work together to bind and reduce CO_2. The synthesis and characterization detailed in Chapter 2 presented surprising results that required ligand modifications to address unforeseen issues. It was shown that template syntheses involving $[Ni(H_2O)_6](BF_4)_2$ incorporated a single nickel ion, leaving the second binding site available to add a different metal ion. However, the diamine used (phenyl, propyl, ethyl) controlled the flexibility of the pocket, with 1,3-diaminopropane (L^2) allowing stoichiometric insertion while *o*-phenylenediamine (L^1) and ethylenediamine (L^3) were too rigid to allow addition of larger metal ions (e.g. Fe(II) and Mn(II)). Synthetically, complexes containing the L^2 ligand present challenges regarding characterization. Nickel adopts a 6-coordinate geometry in L^2, allowing a magnetic orbital on Ni to interact with magnetic orbitals of the second metal through the phenoxo-bridge, leading to antiferromagnetic coupling. Complexes containing L^3 were the best characterized, with the complexes easily crystallized. It was shown that these complexes retained square planar geometry for Ni(II), resulting in a simple paramagnet upon insertion of a second metal ion.

The complexes displayed varying redox behavior, with compounds of the formula $[NiH_2L^n](BF_4)_2$ (with n = 1 & 3) displaying ligand reductions, while bimetallic complexes $[NiML^n](BF_4)_2$ (with M = Ni, Co, Fe and n = 1 & 3) displaying what appears to be Ni(II/I) reductions as the first reduction process, with this assessment supported in the literature.

Complexes containing L^1 and L^3 did not show promising reactivity with CO_2 for reduction. $\{[NiL^1]_2\text{-}\mu\text{-}Fe\}(BF_4)_2$ displayed interaction with CO_2 after reduction of the complex by $1e^-$. The details of this interaction are not yet understood, but it does not lead the production of CO. Of the complexes made in Chapter 2, the most promising example was the complex $[NiCoL^2](BF_4)_2$, which displayed catalytic behavior in the cyclic voltammogram in acidic conditions; however, H_2 and not CO was detected during bulk electrolysis.

Although these complexes did not result in CO production, we believe that the right combination of acid and base, along with contributions from the ligand macrocycle, could lead to an effective method to bind and reduce CO_2 at low overpotentials. Although nature has had much more time to tune CODH II, our understanding of the importance of cooperative effects has increased dramatically in the last two decades, and should continue to develop as more complexes display these properties.

CHAPTER 6

Experimental

6.1. Synthetic Methods & Materials

Many of the complexes described below are air-sensitive, and must be handled under an inert atmosphere of nitrogen using standard glovebox and Schlenk techniques. Unless otherwise noted, all procedures were performed at ambient temperature (21-24 °C). All solvents were sparged with argon and dried using a solvent purification system. Acetonitrile, ethereal, and halogenated solvents were passed through two columns of neutral alumina. DMF and alcohol solvents were passed through columns of activated molecular sieves. The ligands salen, salophen, sal-pren and the metal starting materials $[M(CH_3CN)_{4\text{-}6}][BF_4]_2$ were synthesized according to established procedures. Potassium graphite (KC_8) was synthesized by heating stoichiometric amounts of potassium and graphite in drybox until a homogenous bronze-colored powder was obtained. All other materials, including CO_2 (99.999%) and CO (99.5%), were purchased from commercial sources and used without further purification.

6.2. Physical Methods

Elemental analyses (EA) were performed on a Perkin Elmer 2400 Series II CHNS/O analyzer. Electrospray ionization mass spectrometry (ESI-MS) was performed with a Micromass LCT mass spectrometer. Gas chromatography (GC) was performed on an Agilent Technologies 7890A GC system with a front TCD inlet and detector. Samples were run using a 500 mL injection using a 5:1 split injection method. The column used was a isothermally at 40 °C. Nuclear magnetic resonance (NMR) spectra were recorded on a

Bruker GN500 spectrometer with a BBO probe (^{1}H and ^{13}C). ^{1}H NMR spectra were referenced to TMS using the residual proteo impurities of the solvent; All chemical shifts are reported in the standard δ notation in parts per million; positive chemical shifts are to a higher frequency from the given reference. Solution magnetic moments were determined by Evans Method using a sealed capillary containing either 5% CH_2Cl_2/d^6-DMSO as an internal reference.[121] Perpendicular-mode X-band electron paramagnetic resonance (EPR) spectra were collected using a Bruker EMX spectrometer. Infrared (IR) absorption measurements were taken as liquid films on a Varian 1000 spectrophotometer. Spectroelectrochemical experiments were performed using a 3-electrode cell with gold working, silver reference, and gold counter electrodes. Background spectra were taken before electrolysis, and difference spectra were collected while applying a controlled potential. For each experiment, potentials were measured and applied relative to an internal ferrocene reference. Electrochemical experiments were carried out with a Pine Wavedriver 10 potentiostat. Electrochemical experiments were carried out in an acetonitrile or DMF solution with ~ 2.0 mM analyte and 0.20 M Bu_4NPF_6 or Bu_4NBF_4. The working electrode was a glassy carbon disc with a diameter of 3 mm or 1 mm; the counter electrode was a glassy carbon rod; and the reference electrode was a silver wire in 0.20 M Bu_4NPF_6 or Bu_4NBF_4 in CH_3CN separated from the bulk solution by a Vycor frit. Potentials were referenced at 100 mV/s (unless otherwise noted) to the ferrocene/ferrocenium couple at 0 V using ferrocene as an internal reference. M(salen) and Fsal-n-M (where M = Co, Ni, n = 2,3) were prepared according to literature methods.[67,98,99,101,122]

6.2.1. Detection of products by GC

Bulk electrolysis was carried out using a single compartment cell with a working electrode (vitreous carbon), reference electrode (silver wire in 0.2 M Bu_4NPF_6 in CH_3CN separated by Vycor frit) and a counter electrode (vitreous carbon). The working compartment contained > 2.0 mM, 0.20 M Bu_4NPF_6, and 2.0 mM NH_4BF_4 in acetonitrile. The headspace of the working compartment was sampled by syringe. The method for CO detection utilized a split 5:1 split injection, operating under isothermal conditions at 40°C, helium carrier gas and 500 μL injections. CO was detected at a retention time of c.a. 11 min, with adequate separation from N_2 and O2.

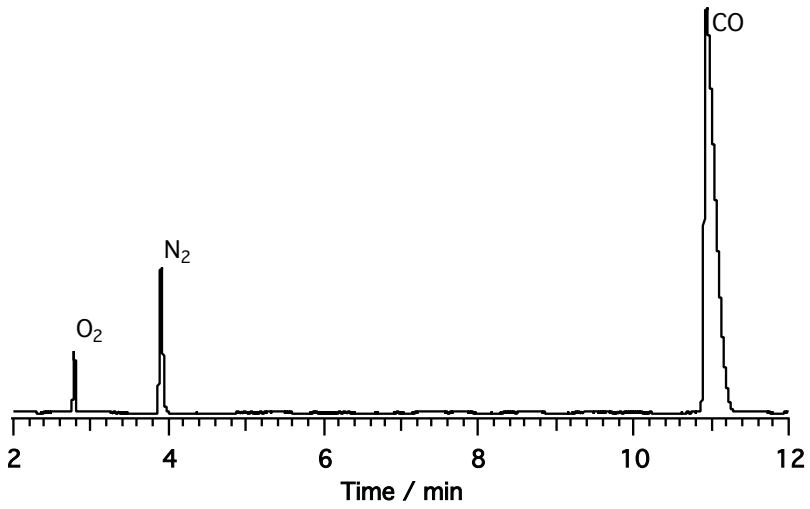

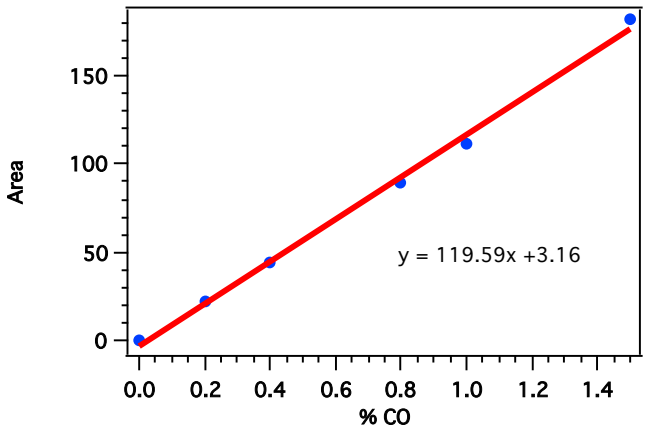

6.3. M(SALEN) SYNTHESIS

6.3.1. H_2Salen (salen = N,N'-ethylenebis(salicylimine)).

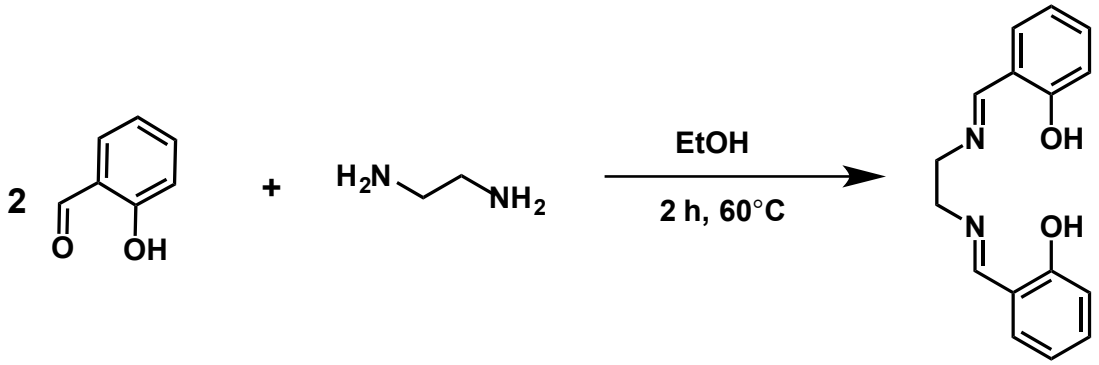

To a solution containing salicylaldehyde (8.26 mmol) in 15 mL of ethanol was added ethylenediamine (4.48 mmol) in minimal ethanol. The solution was heated to 60°C for 5 minutes, whereby the yellow crystals were filtered and washed with cold ethanol. (Yield 93.4%). ^{1}H NMR (500 MHz, d^6-DMSO) δ: 13.37 (2H, s), 7.41 (2H, dd), 7.31 (2H, td), 6.86 (4H, m), 3.92 (4H, s).

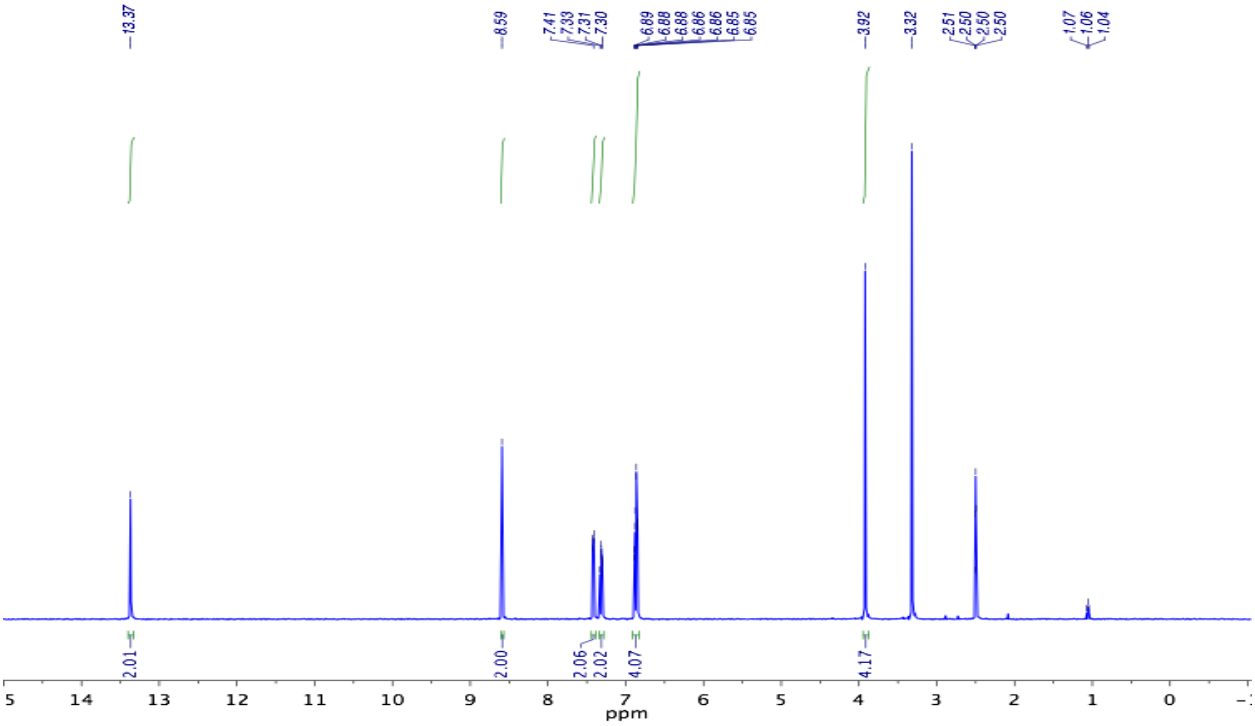

6.3.2. H_2Salpn (salpn = N,N'-propylenebis(salicylimine)).

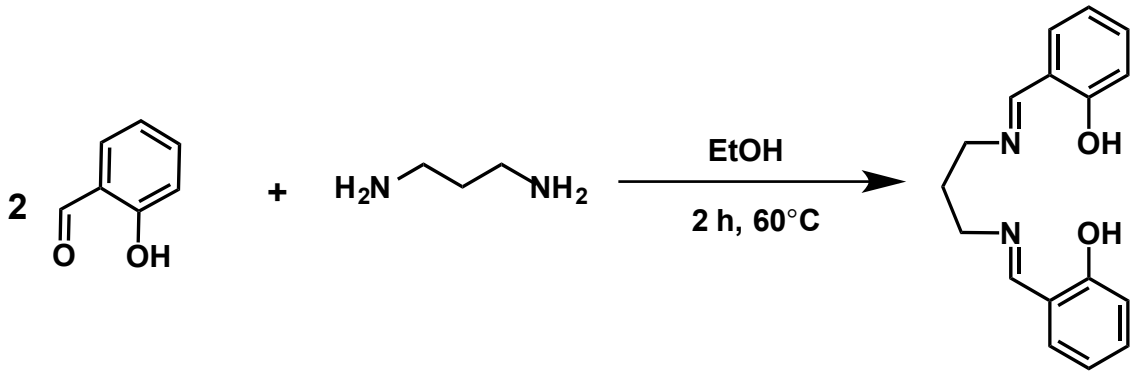

To a solution refluxing ethanolic solution containing salicylaldehyde (4.21 mmol) was added 1,3-diaminopropane (in 5 mL CH_3OH, 2.10 mmol). The solution was kept at reflux for 2 h, whereby the solution was concentrated under vacuum until precipitate formed. The precipitate was filtered and washed with diethyl ether (5 mL, 3X). (Yield 79.8%) ^{1}H NMR (500 MHz, d^6-DMSO) δ: 13.48 (2H, broad s), 8.58 (2H, s), 7.42 (2H, d), 7.32 (2H, dd), 6.88 (4H, m), 3.68 (4H, t), 2.02 (2H, q).

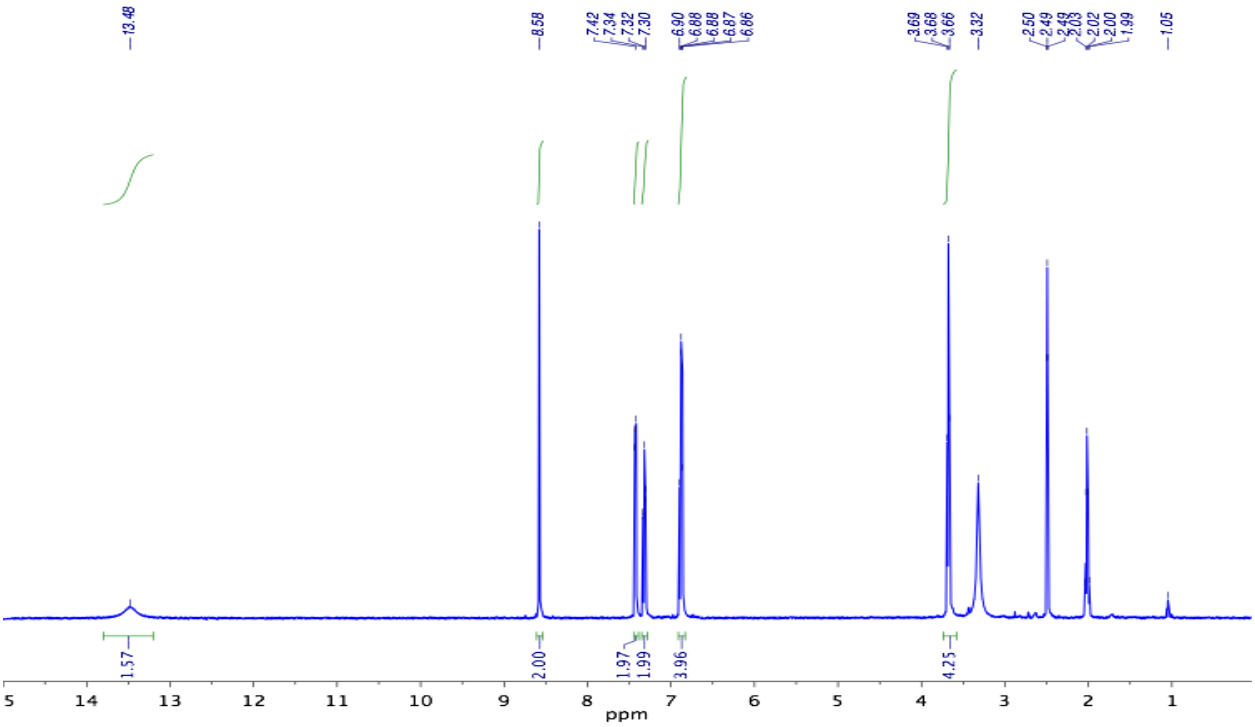

6.3.3. H_2Salp (salp = N,N'-phenylenebis(salicylimine)).

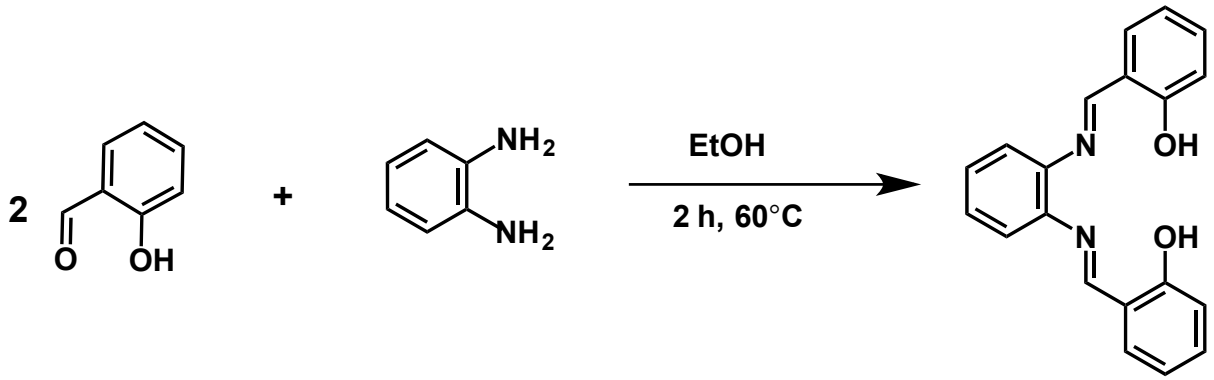

To a solution containing salicylaldehyde (16.5 mmol) in 15 mL of ethanol was added *o*-phenylenediamine (8.48 mmol) in minimal ethanol. The solution was heated to 60°C for 30 minutes, whereby the orange crystals were filtered and washed with cold ethanol. (Yield 83.5%). ^{1}H NMR (500 MHz, d^6-DMSO) δ: 13.09 (2H, s), 8.78 (2H, s), 7.52 (2H, dd), 7.39 (4H, m), 6.98 (4H, m).

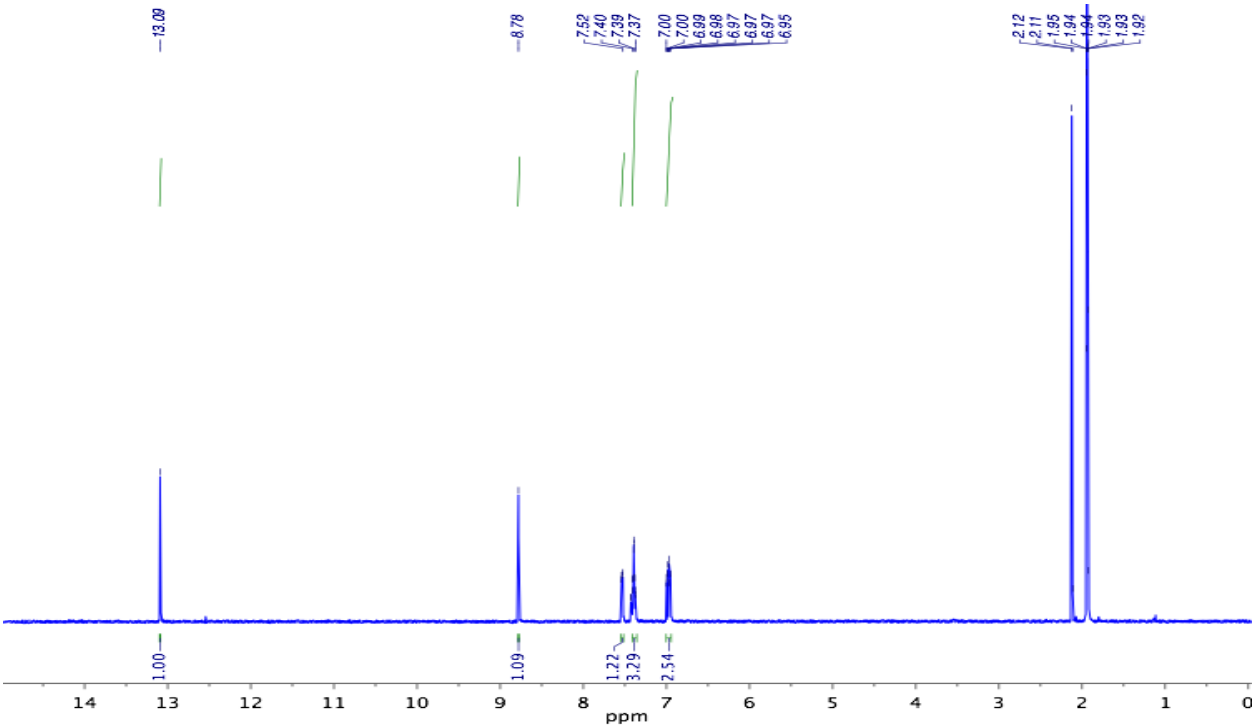

6.3.4. Co(salen). H_2salen (1.18 mmol) was dissolved in hot ethanol for 30 min under N_2. $Co(C_2H_4O_2)_2$*$4H_2O$ (1.17 mmol) in water was added dropwise over 10 min and the solution was allowed to reflux for 5 minutes. The red product was filtered, washed with water and ether and dried *en vacuo*.

6.3.5. Co(salpn). H_2salpn (0.560 mmol) was dissolved in hot ethanol for 30 min under N_2. $Co(C_2H_4O_2)_2$*$4H_2O$ (0.592 mmol) in water was added dropwise over 10 min and the solution was allowed to reflux for 5 minutes. The tan precipitate was filtered and washed with water (Yield = 75.0%).

6.3.6. Co(salp). H_2salp (0.959 mmol) was dissolved in hot ethanol for 30 min under N_2. $Co(C_2H_4O_2)_2$*$4H_2O$ (0.950 mmol) in water was added dropwise over 10 min and the solution was allowed to reflux for 5 minutes. The red product was filtered and washed with water (Yield = 82.5%). ESI-MS *m/z*: 372.98 (M^+), 746.03 ($2M^+$). CV (Bu_4NBF_4): $E_{1/2}$, V vs Fc/Fc^+ = -0.34 ($Co^{3+/2+}$), -1.57 V ($Co^{2+/+}$).

6.3.7. Ni(salen). H_2salen (0.887 mmol) was dissolved in hot ethanol for 30 min. $Ni(C_2H_4O_2)_2$*$4H_2O$ (0.899 mmol) in water was added dropwise over 10 min and the solution was allowed to reflux for 5 minutes. The orange product was filtered and washed with water. ^{1}H NMR (500 MHz, d^6-DMSO) δ: 7.91 (2H, s), 7.28 (2H, dd), 7.16 (4H, td), 6.71 (2H, d), 6.52 (2H, t). CV (Bu_4NBF_4): $E_{1/2}$, V vs Fc/Fc^+ = -2.11 V ($Ni^{2+/+}$).

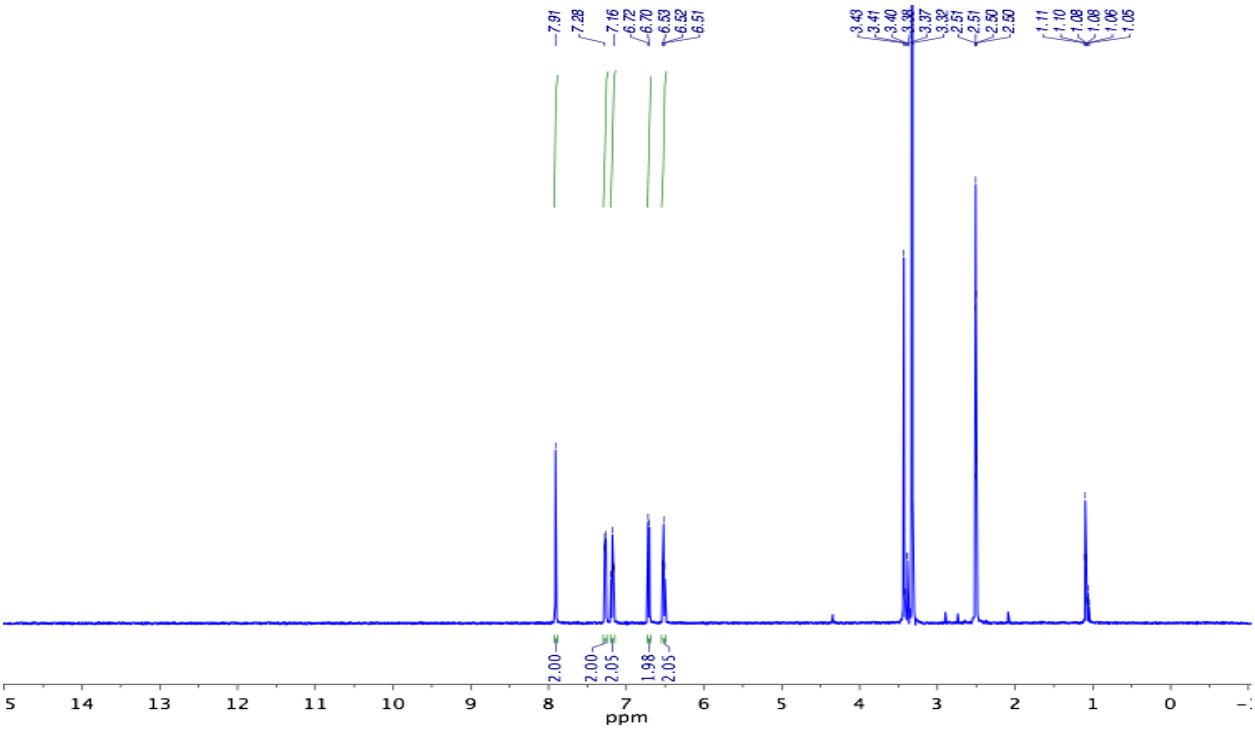

6.3.8. Ni(salpn). H_2salpn (0.446 mmol) was dissolved in hot ethanol for 30 min. $Ni(C_2H_4O_2)_2$*$4H_2O$ (0.467 mmol) in water was added dropwise over 10 min and the solution was allowed to reflux for 5 minutes. The pea green product was filtered and washed with water.

6.3.9. Ni(salp). H_2salp (0.493 mmol) was dissolved in hot ethanol for 30 min. $Ni(C_2H_4O_2)_2$*$4H_2O$ (0.516 mmol) in water was added dropwise over 10 min and the solution was allowed to reflux for 5 minutes. The red product was filtered and washed with water. Recrystallization from vapor diffusion of diethyl ether into a chloroform solution yielded red needles of Ni(salp). ESI-MS *m/z*: 373.01 ($M\text{-}H^+$), 395.02 ($M\text{-}Na^+$), 746.03 ($2M\text{-}H^+$), 767.02 ($2M\text{-}Na^+$). ^{1}H NMR (500 MHz, d^6-DMSO) δ: 8.89 (2H, s), 8.15 (2H, dd), 7.60 (2H, d), 7.31 (4H, m), 6.89 (2H,d), 6.67 (2H, t). CV (Bu_4NBF_4): E_c, V vs Fc/Fc^+ = -1.85 V ($Ni^{2+/+}$).

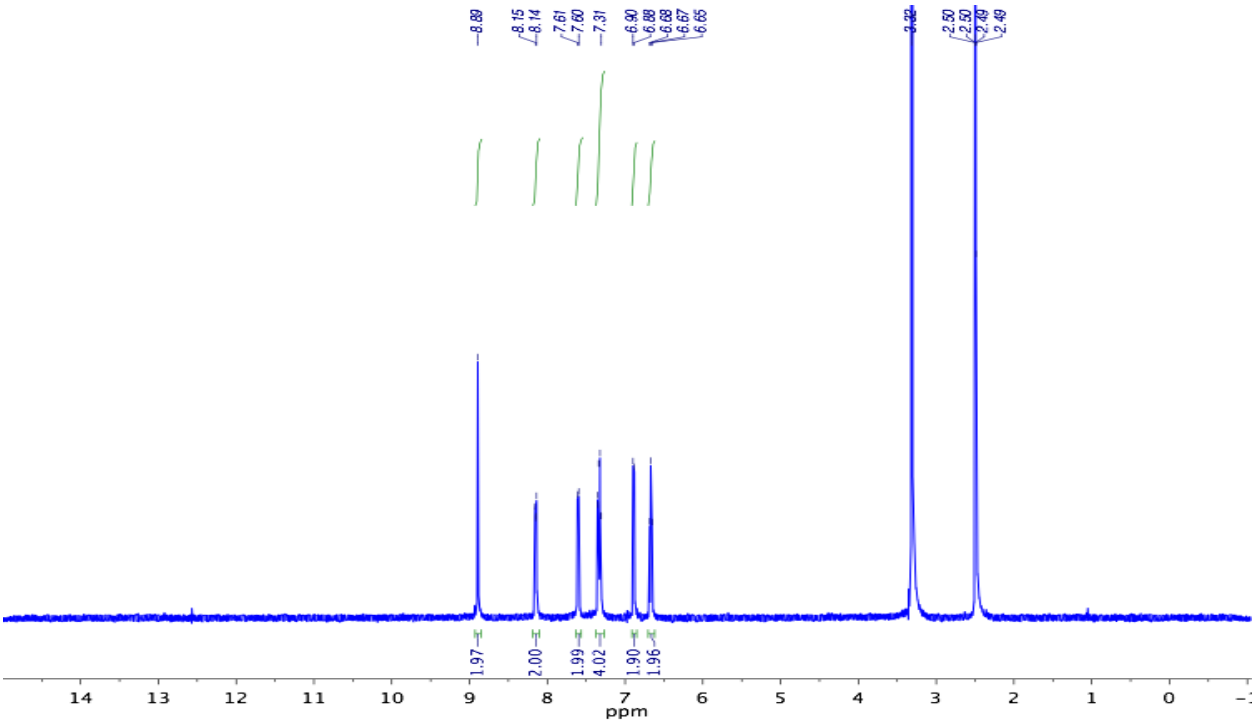

6.4. NiM HETEROBIMETALLICS

6.4.1. $[NiH_2L^1](BF_4)_2$

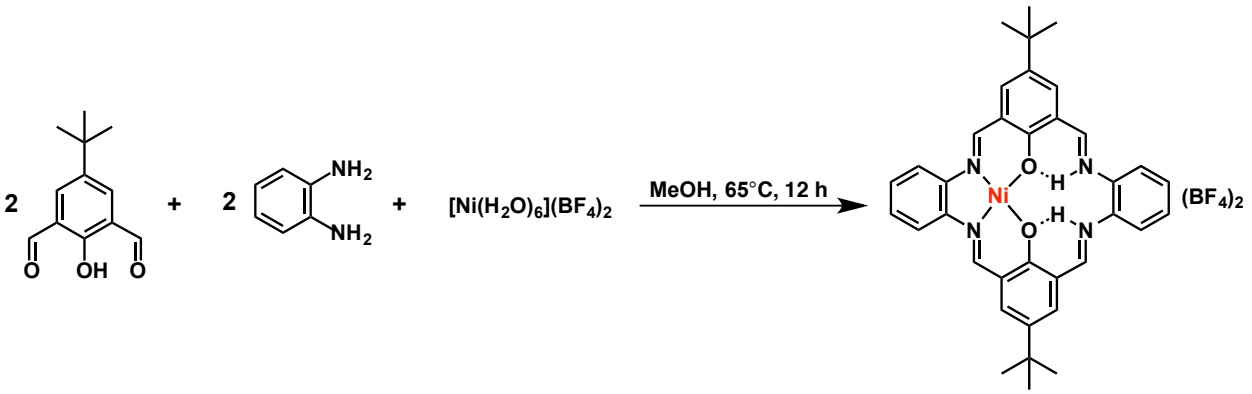

Modified from a previously reported procedure.[73] A solution containing *o*-phenylenediamine (5.94 mmol) and $[Ni(H_2O)_6](BF_4)_2$ (2.94 mmol) in a minimal amount of methanol was added to a warm solution of 4-*tert*-butyl-2,6-diformylphenol (5.92 mmol) in 100 mL of methanol. The solution was brought to reflux for 8 h, filtered, washed with cold methanol, and dried under vacuum (yield 70%). Crystals suitable for X-ray analysis were grown from vapor diffusion of diethyl ether into a concentrated DMF solution containing the compound. ESI-MS *m/z*: 613.12 (M^+). ^{1}H NMR (500 MHz, d^6-DMSO) δ: 13.65 (1H, s), 8.74 (2H, s), 8.30 (2H, s), 7.71 (2H, dd), 7.66 (2H, broad s), 7.62 (4H, dd), 7.56 (2H, dd), 7.31 (2H, dd), 1.38 (18H, s). CV (Bu_4NBF_4): E_c, V vs $Fc^{+/0}$ = -1.06 V ($Ni^{2+/+}$), -2.05 V.

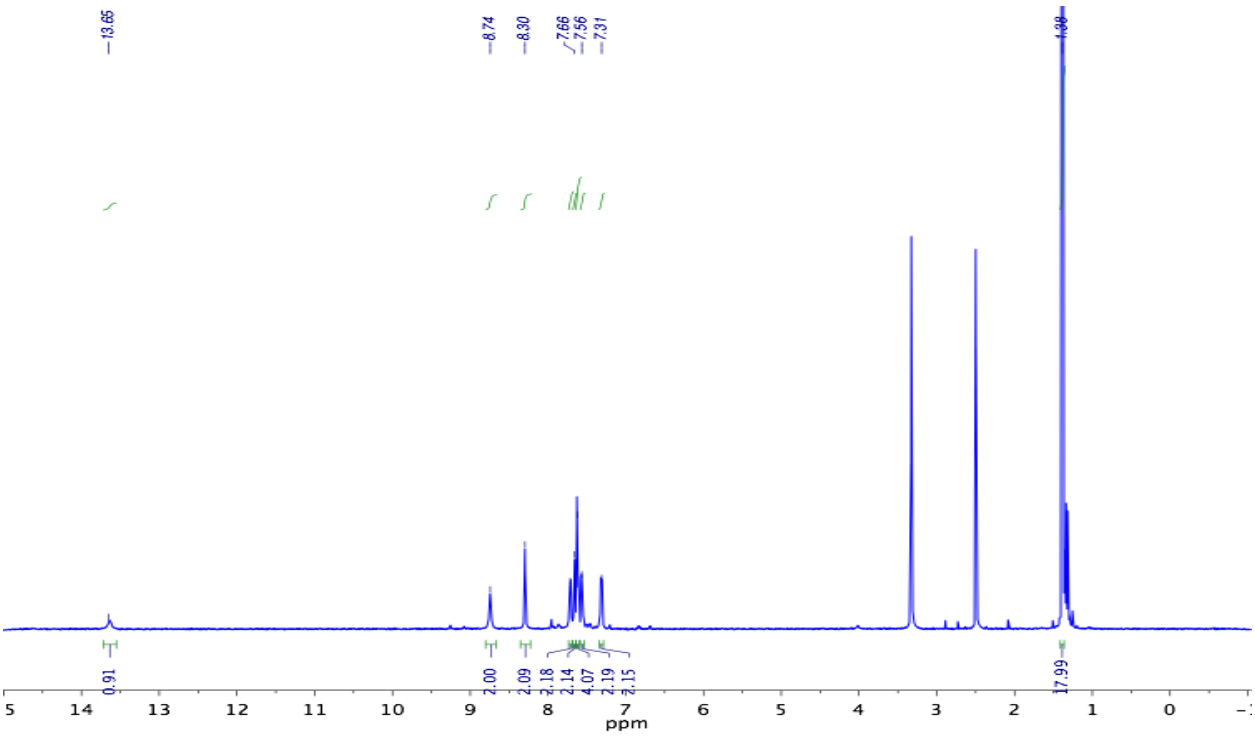

6.4.2. $[NiZnL^1](BF_4)_2$. To a vigorously stirred solution of $[NiH_2L^1](BF_4)_2$ in DMF was added solid KO^{t}Bu followed by the addition of solid $[Zn(H_2O)_x](BF_4)_2$. This reaction was allowed to stir at room temperature for approximately 2 hours. The red-brown solution was poured

into 40 mL diethyl ether, and the resulting precipitate was filtered, washed with diethyl ether and dried under vacuum. ESI-MS *m/z*: 713.10 ($M^*2H_2O^+$). ^1H NMR (500 MHz, d^6-DMSO): 8.57 (2H, s), 8.46 (2H, s), 7.86 (2H, dd), 7.76 (2H, d), 7.68 (2H, d), 7.60 (2H, dd), 7.40 (2H, dd), 7.13 (2H, dd), 1.43 (18H, s).

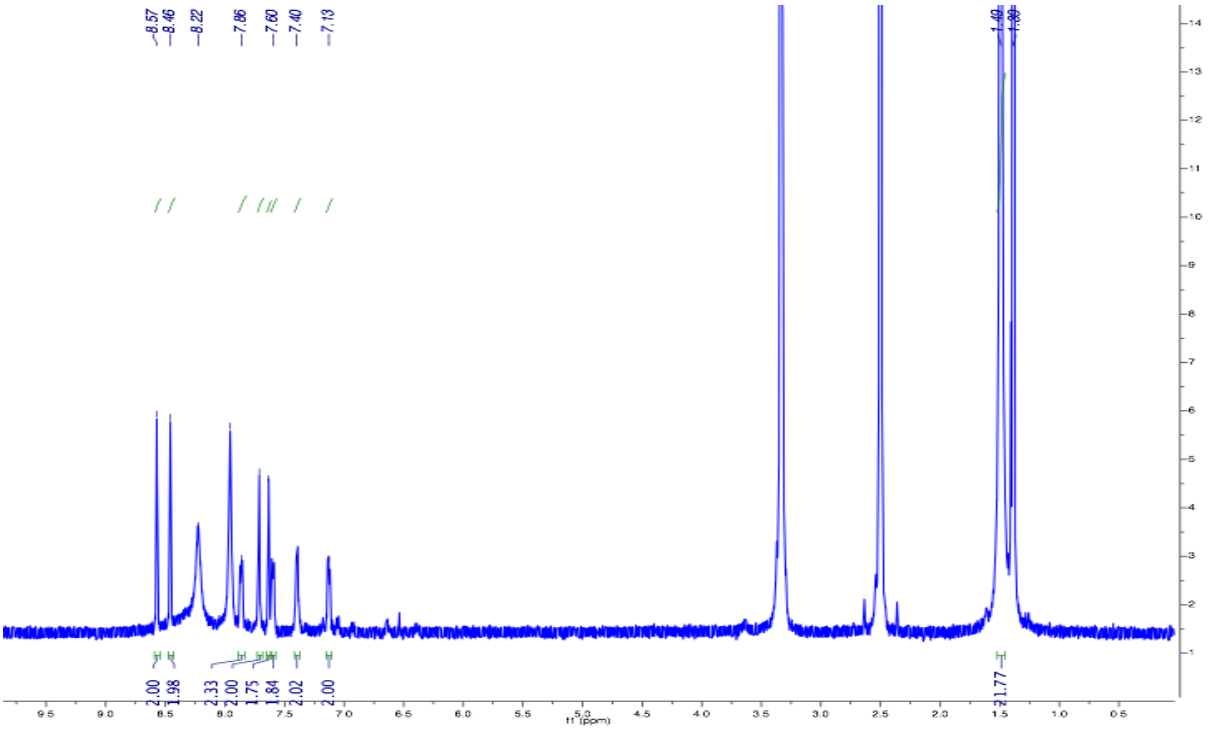

6.4.3. $[NiCuL^1](BF_4)_2$. To a suspension containing $[NiH_2L^1](BF_4)_2$ (0.188 mmol) was added a solution containing $[Cu(MeCN)_4](BF_4)_2$ (0.193 mmol) in a minimal volume of methanol. The reaction was allowed to stir for 15 h at 65°C, and the product was filtered and washed with cold methanol (Yield 81.6%). Alternatively, the method described for $[NiZnL^1](BF_4)_2$ provides the product in nearly the same yield. Single crystals suitable for X-ray analysis were grown from vapor diffusion of diethyl ether in a DMF solution containing the product. ESI-MS *m/z*: 337.55 ($M^{2+}/2$). ^1H NMR (500 MHz, d^6-DMSO) δ: 21.48, 15.20, 11.02, 9.94. X-band EPR (DMF/THF 1:1, 77 K): $g_1 = 2.1$. No EA was collected.

6.4.4. $[Ni_2L^1](BF_4)_2$. A suspension of $[NiH_2L^1](BF_4)_2$ (0.197 mmol) in methanol was brought to reflux. To this suspension was added a solution of $[Ni(H_2O)_6](BF_4)_2$ (1.2 eq) in minimal methanol dropwise. The mixture was allowed to reflux for 72 h, where the product was filtered and washed with cold methanol. ESI-MS *m/z*: 335.0 ($M^{2+}/2$), 757.1 ($M\text{-}BF_4^+$). ^{1}H NMR (500 MHz, d^6-DMSO) δ: 21.62, 15.18, 11.00, 9.89. No EA was collected.

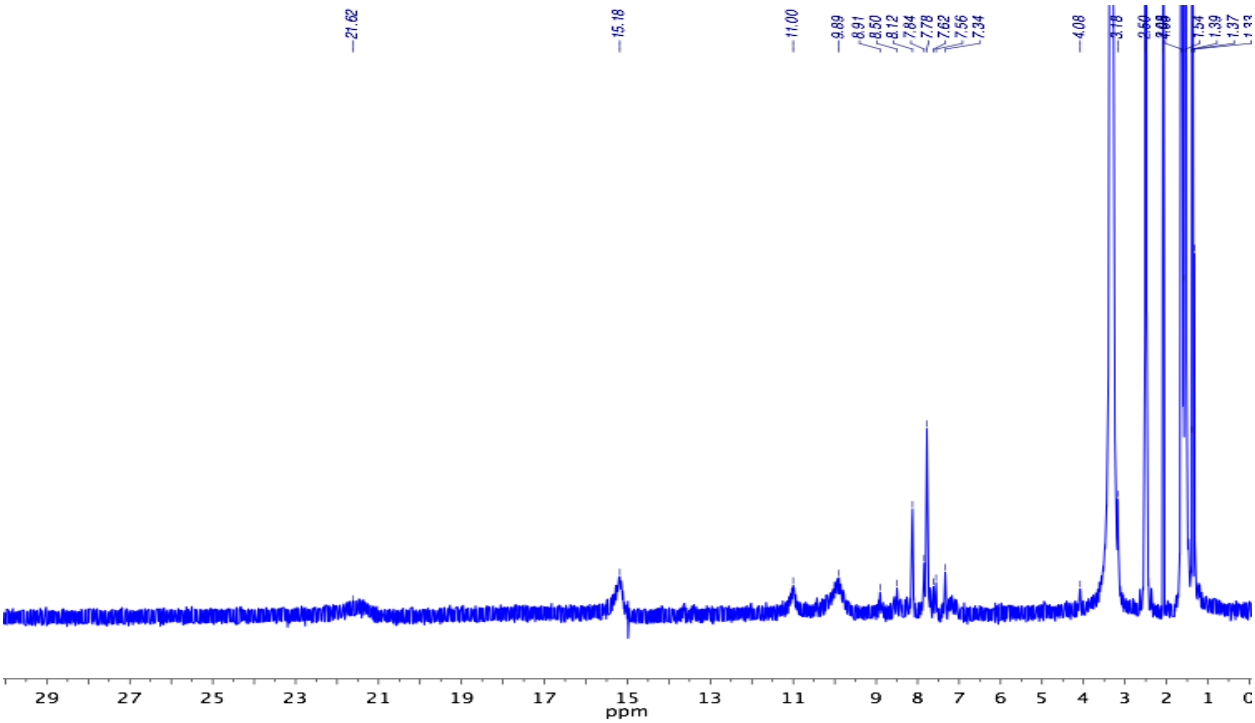

6.4.5. $\{[NiL^1]_2\text{-}\mu\text{-}Co\}(BF_4)_2$. In an O_2 free glovebox, $[NiH_2L^1](BF_4)_2$ (0.0674 mmol) was dissolved in 5 mL DMF. Solid KO^{t}Bu (0.146 mmol) was added with vigorous stirring, followed by the addition of solid $[Co(CH_3CN)_6](BF_4)_2$ (0.0691 mmol). The reaction was stirred at room temperature for 2 hrs, where the solution was poured into 40 mL of diethyl ether and the precipitate was collected and dried under vacuum to yield an orange powder. ^{1}H NMR (500 MHz, d^6-DMSO) δ: 17.80, 12.45, 9.44, 5.93, 5.10, 4.65. ESI-MS *m/z*: 641.58

($M^{2+}/2$). EPR (DMF/THF 1:1, 77 K): g_1 = 4.16. E_c, V vs $Fc^{+/0}$ = -1.40 V ($Ni^{I}Co^{II}$). No EA was collected.

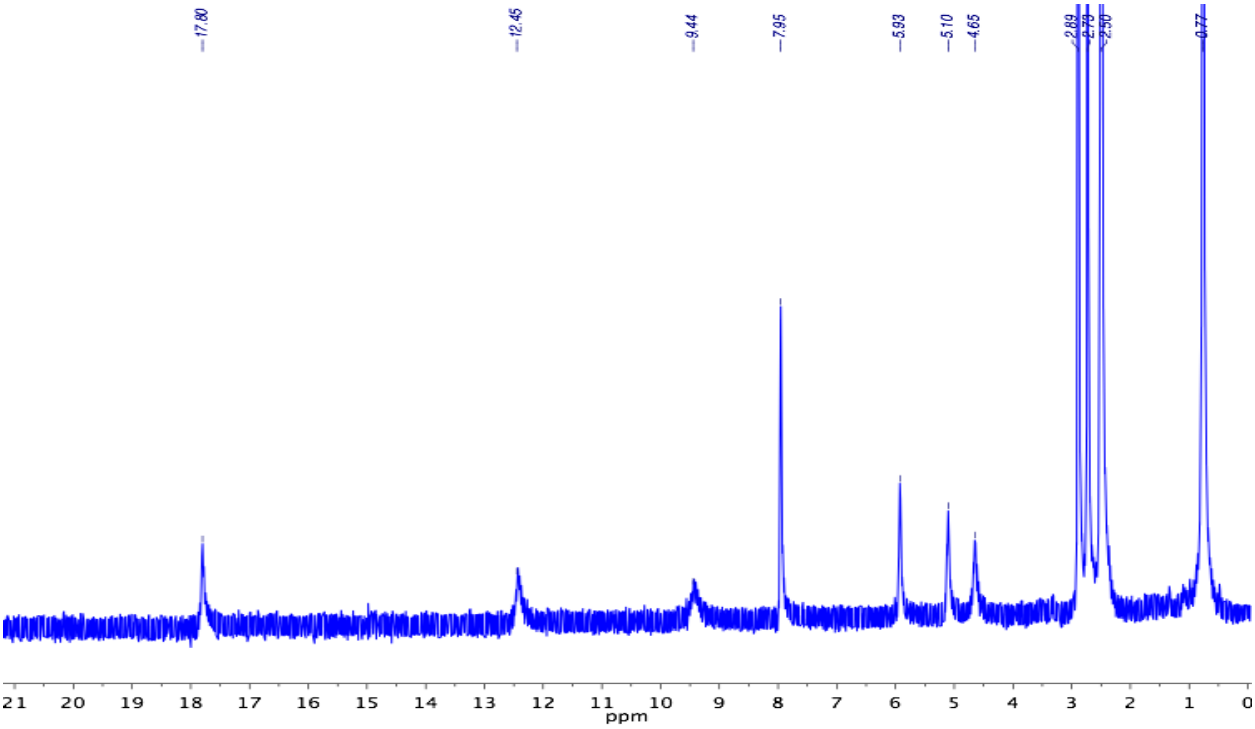

6.4.6. {[NiL^1]$_2$-μ-Fe}(BF$_4$)$_2$. Analogous to [NiCoL^1](BF$_4$)$_2$. Suitable crystals for X-ray analysis were grown from vapor diffusion of diethyl ether into a saturated solution of analyte in CH_3CN. ^{1}H NMR (500 MHz, d^6-DMSO) δ: 26.52, 17.26, 16.68, 10.72, 9.22, 8.26. ESI-MS *m/z*: 640.09 ($M^{2+}/2$). E_c, V vs $Fc^{+/0}$ = -1.45 V ($Ni^{I}Fe^{II}$). No EA was collected.

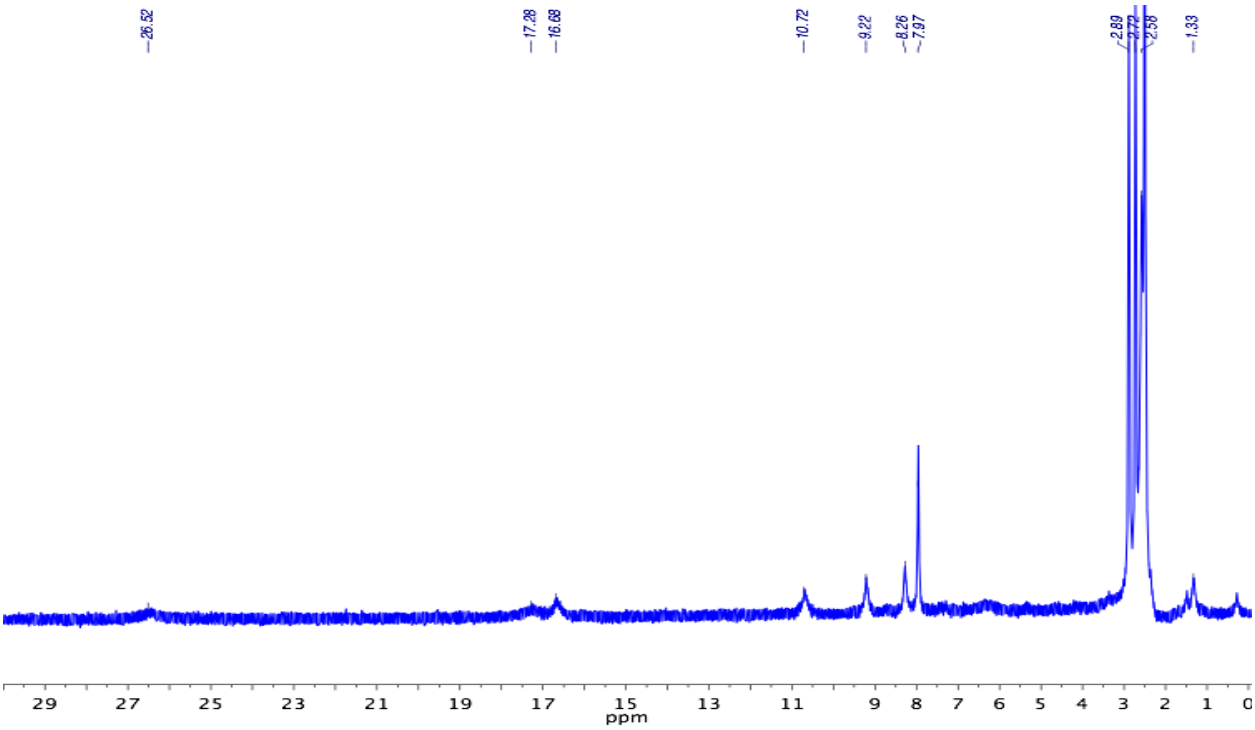

6.4.7. $[NiH_2L^2](BF_4)_2$

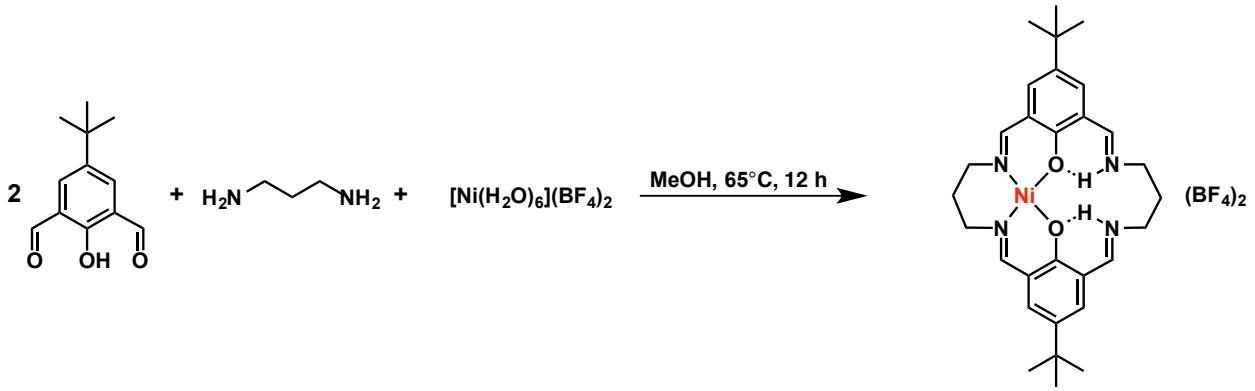

Analogous to $[NiH_2L^1](BF_4)_2$ substituting 1,3-diaminopropane for *o*-phenylenediamine. After refluxing for 12 h, the solvent was removed under vacuum. The resulting precipitate was washed with 5 mL of diethyl ether (3X) to remove excess diformylphenol and dried to produce a tan powder. Suitable crystals for X-ray analysis were grown from vapor diffusion of diethyl ether into a saturated solution in methanol. ^{1}H NMR (500 MHz, d^6-DMSO) δ:

29.28, 12.54, 11.99, 7.81, 7.13, 4.07. ESI-MS *m/z*: 273.08 ($M^{2+}/2$), 545.13 ($M\text{-}H^{+}$), 633.15 ($M\text{-}BF_4^{+}$). E_c, V vs $Fc^{+/0}$ = -1.42 V. No EA was collected.

6.4.8. $[NiCoL^2](BF_4)_2$. To a solution of $[NiH_2L^2](BF_4)_2$ (0.178 mmol) in acetonitrile was added a THF solution (0.359 mmol) of KO^tBu, followed by the addition of $[Co(CH_3CN)_6](BF_4)_2$ (0.195 mmol). After stirring for 30 min, the solution was concentrated and precipitated from diethyl ether. Crystals suitable for X-ray analysis were grown from ether diffusion into a saturated solution of sample in acetonitrile. Crystals were isomorphous with $[NiFeL^2](BF_4)_2$. ESI-MS *m/z*: 302.03 ($M^{2+}/2$), 322.54 ($M^{2+}*CH_3CN/2$), 343.06 ($M^{2+}*2CH_3CN/2$), 691.06 ($M\text{-}BF_4^{+}$), 717.02 ($M*2CH_3CN*CH_3OH^{+}$). E_c, V vs $Fc^{+/0}$ = -1.44 V ($Ni^{I}Co^{II}$), -1.62 V ($Ni^{I}Co^{I}$). No EA was collected.

6.4.9. $[NiZnL^2](BF_4)_2$. To a solution of $[NiH_2L^2](BF_4)_2$ (0.121 mmol) in acetonitrile was added a THF solution (0.265 mmol) of KO^tBu, followed by the addition of $[Zn(H_2O)_x](BF_4)_2$ (0.280 mmol). After stirring for 30 min, the product was precipitated with diethyl ether, filtered, and washed with ether. ESI-MS *m/z*: 689.05 ($M\text{-}BF_4^{+}$). E_c, V vs $Fc^{+/0}$ = -1.42 V ($Ni^{I}Zn^{II}$). No EA was collected.

6.4.10. $[NiCuL^2](BF_4)_2$. Analogous to $[NiCoL^2](BF_4)_2$. Precipitated with diethyl ether. ESI-MS *m/z*: 303.53 ($M^{2+}/2$), 344.56 ($M*2CH_3CN/2$), 694.12 ($M\text{-}BF_4^{+}$), 720.03 ($M*2CH_3CN*CH_3OH^{+}$).

6.4.11. [NiFeL^2](BF$_4$)$_2$. Analogous to [NiCoL^2](BF$_4$)$_2$. ESI-MS *m/z*: 301.04 (M^{2+}/2), 320.06 (M^{2+}*CH_3CN/2), 340.57 (M*2CH_3CN/2), 686.09 (M-BF_4^+), 714.05 (M*2CH_3CN*CH_3OH^+). E_c, V vs $Fc^{+/0}$ = -1.42 V ($Ni^{I}Fe^{II}$). Structure represented as 2 Ni ions, since symmetry prevented the identification of the metal ions. No EA was collected.

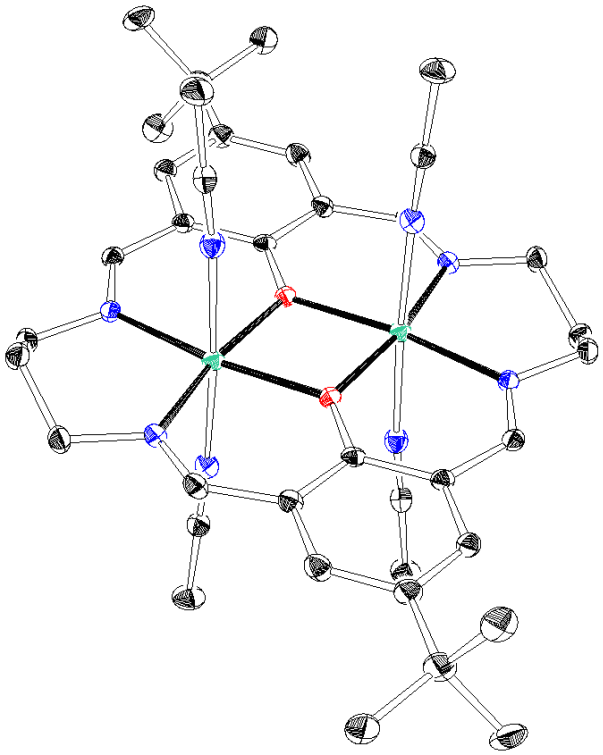

6.4.12. [NiH$_2$L^3](BF$_4$)$_2$

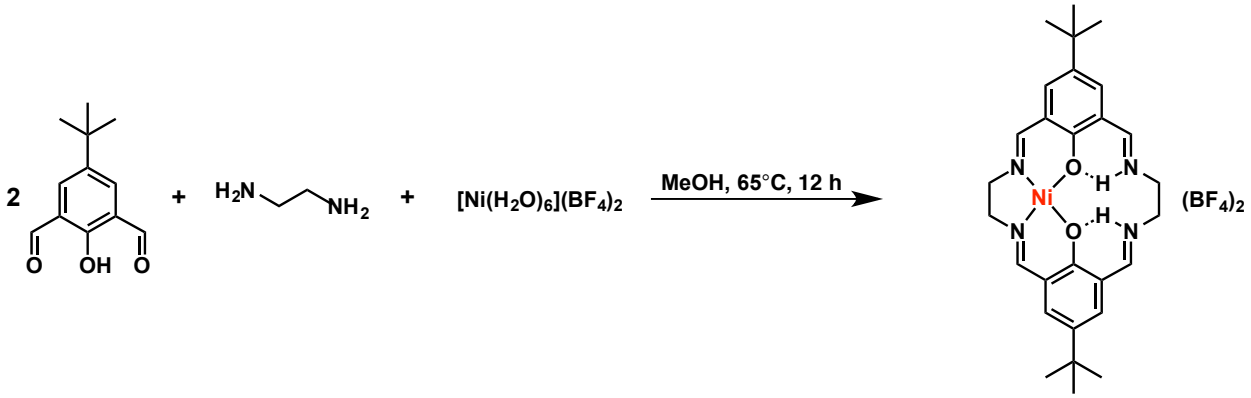

A solution containing ethylenediamine (1.50 mmol) and $[Ni(H_2O)_6](BF_4)_2$ (0.696 mmol) in a minimal amount of ethanol was added to a warm solution of 4-*tert*-butyl-2,6-diformylphenol (1.37 mmol) in 50 mL of ethanol. The solution was brought to reflux for 12 h, filtered, washed with cold methanol, and dried under vacuum (yield 76.2%). Crystals suitable for X-ray analysis were grown from vapor diffusion of diethyl ether into a concentrated DMF solution containing the compound. 50% Ni disorder in both pocket sites. ESI-MS *m/z*: 519.18 (M^+), 259.09 ($M^{2+}/2$). ^{1}H NMR (500 MHz, d^6-DMSO) δ: 13.1 (1H, s), 8.71 (2H, s), 8.15 (2H, s), 7.75 (2H, s), 3.93 (4H, s), 3.64 (4H, s), 1.29 (18H, s). CV (Bu_4NPF_6): E_c, V vs $Fc^{+/0}$ = -1.41 V, -1.65 V.

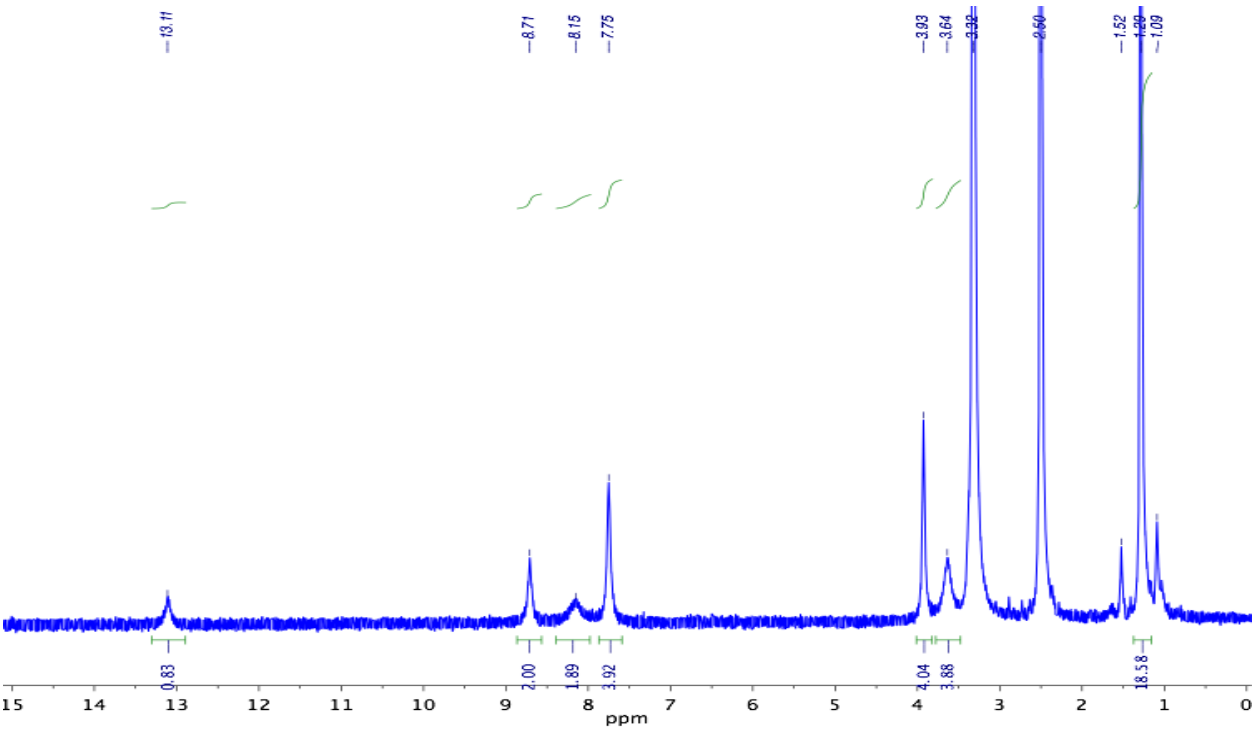

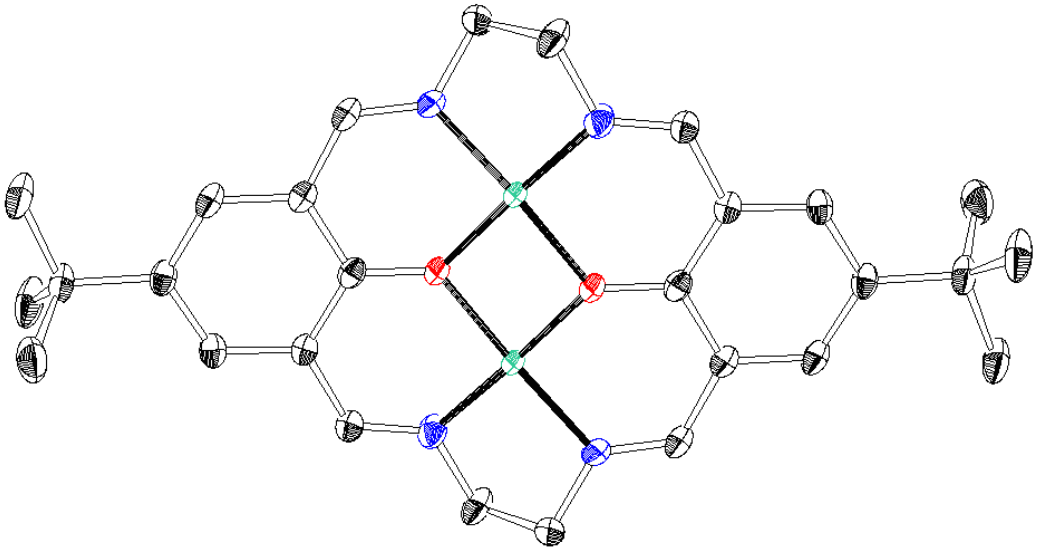

6.4.13. $[NiZnL^3](BF_4)_2$. To a solution of CH_3CN and DMF (5 mL, 1 mL respectively) containing $[NiH_2L^3](BF_4)_2$ (0.279 mmol) was added LiO^tBu in THF (.611 mmol), followed by a solution containing $[Zn(H_2O)_x](BF_4)_2$ (0.472 mmol) in a minimal volume of acetonitrile. The reaction was allowed to stir for 2 h at room temperature, and the product precipitated with diethyl ether. Single crystals suitable for X-ray analysis were grown from vapor diffusion of diethyl ether in an acetonitrile solution containing the product. ESI-MS *m/z*: 332.08 (M^{2+}*$2CH_3CN$/2), 599.14 (M*H_2O^+), 617.10 (M*$2H_2O^+$), 667.14 (M-BF_4^+), 693.08 (M*$2CH_3CN$*$1CH_3OH^+$).

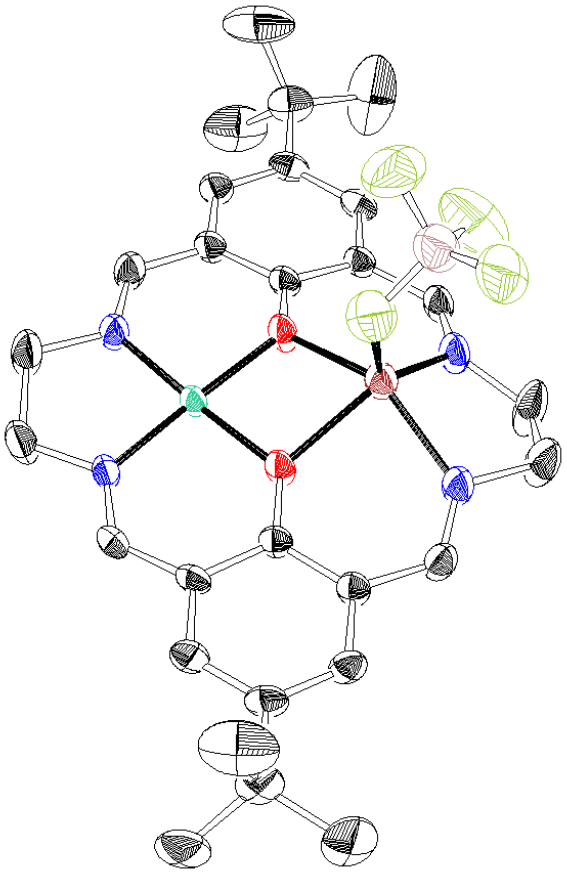

6.4.14. [NiCuL^3](BF$_4$)$_2$. To a solution of CH_3CN and DMF (5 mL, 1 mL respectively) containing $[NiH_2L^3](BF_4)_2$ (0.193 mmol) was added LiO^{t}Bu in THF (.405 mmol), followed by a solution containing $[Cu(MeCN)_4](BF_4)_2$ (0.1928 mmol) in a minimal volume of acetonitrile. The reaction was allowed to stir for 2 h at room temperature, and the product was precipitated with diethyl ether. Single crystals suitable for X-ray analysis were grown from vapor diffusion of diethyl ether in an acetonitrile solution containing the product. ESI-MS *m/z*: 289.54 (M^{2+}/2), 616.09 ($M^*2H_2O^+$), 666.12 ($M\text{-}BF_4^+$), 692.08 ($M^*2CH_3CN^*1CH_3OH^+$). EPR (DMF/THF 1:1, 77 K): g_1 = 2.17 Anal. Calc. (Found) (%): C 44.58 (44.12), H 4.54 (4.83), N 7.43 (7.37).

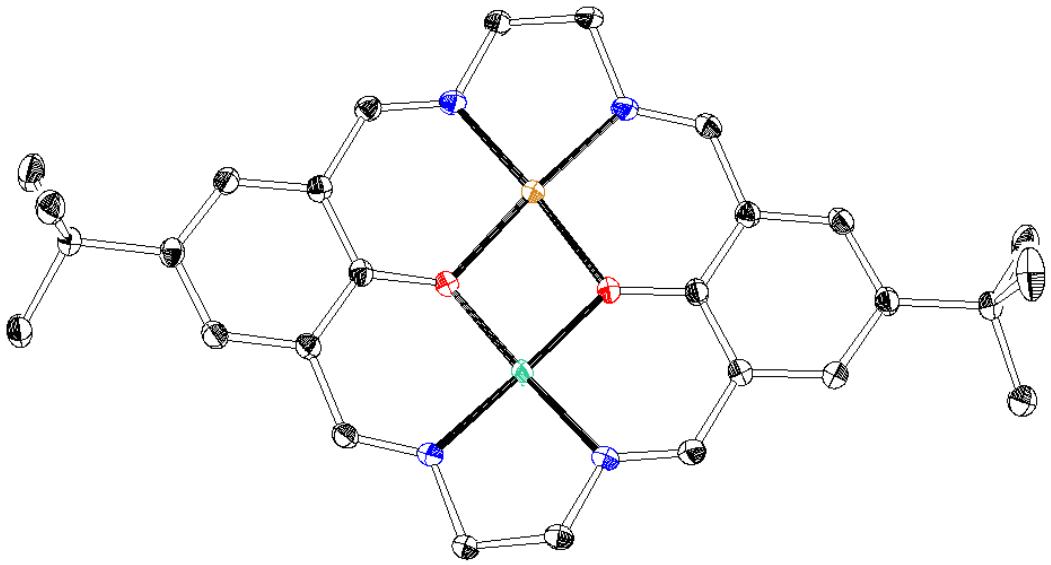

6.4.15. $[Ni_2L^3](BF_4)_2$. Analogous to $[NiCuL^3](BF_4)_2$. Suitable crystals were grown from diffusion of diethyl ether into a saturated solution in acetonitrile. ESI-MS *m/z*: 287.03 ($M^{2+}/2$), 611.10 ($M^*2H_2O^+$), 661.13 (M-BF4$^+$), 689.11 ($M^*2CH_3CN^*1CH_3OH^+$). ^{1}H NMR (500 MHz, d^6-DMSO) δ: 8.16, 7.77. Anal. Calc. (Found) (%): C 44.86 (45.23), H 4.57 (4.58), N 7.47 (7.15). CV (Bu_4NPF_6): E_c, V vs $Fc^{+/0}$ = -1.41 V, -1.65 V.

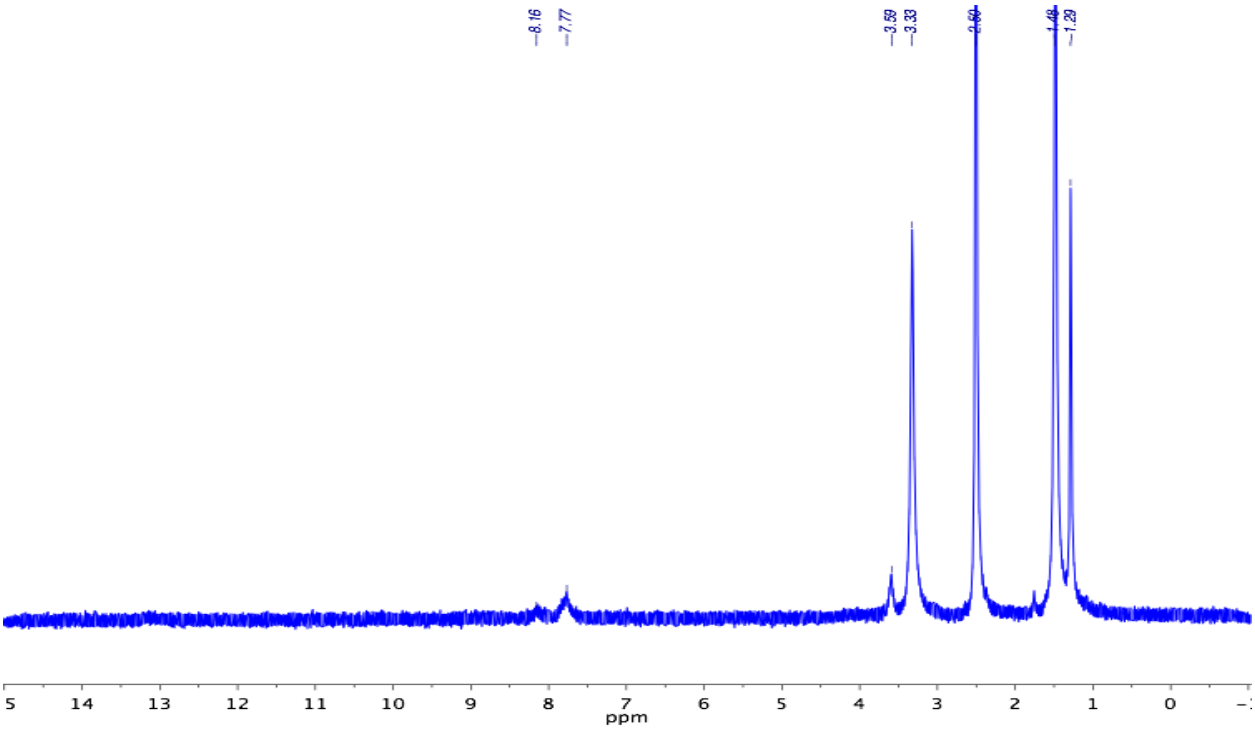

6.4.16. $[NiCoL^3](BF_4)_2$. Analogous to $[NiCuL^3](BF_4)_2$. Suitable crystals were grown from diffusion of diethyl ether into a saturated solution in acetonitrile. Single crystals for X-ray analysis were grown from diffusion of diethyl ether into a saturated solution in acetonitrile. ^1H NMR (500 MHz, d^6-DMSO) δ: 17.78, 14.01, 9.99, 8.67, 6.70, 5.42. ESI-MS *m/z*: 287.56 ($M^{2+}/2$), 610.09 ($M-*2H_2O^+$), 688.09 ($M*2CH_3CN*1CH_3OH^+$). Anal. Calc. (Found) (%): C 45.25 (44.99), H 5.02 (5.08), N 8.51 (8.36). EPR (DMF/THF 1:1, 77 K): g_1 = 3.88. $E_{1/2}$, V vs $Fc^{+/0}$ = -1.24 V ($Ni^{I}Co^{II}$), E_c V vs $Fc^{+/0}$ = -1.65 V ($Ni^{I}Co^{I}$). X-ray data resolved to two structures, with only one shown in Figure 2.7. The second structure (not shown) revealed partial nickel and cobalt in each coordination site, with a single (partial) DMF coordinated to the cobalt atom.

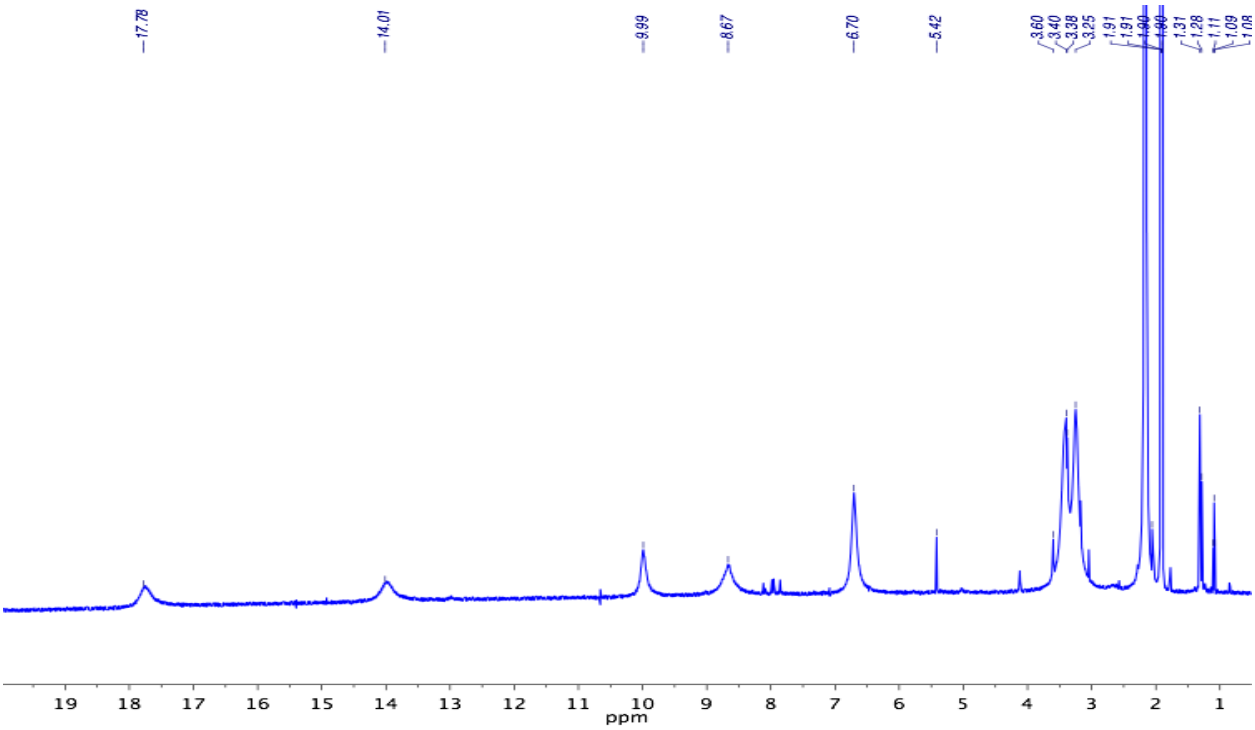

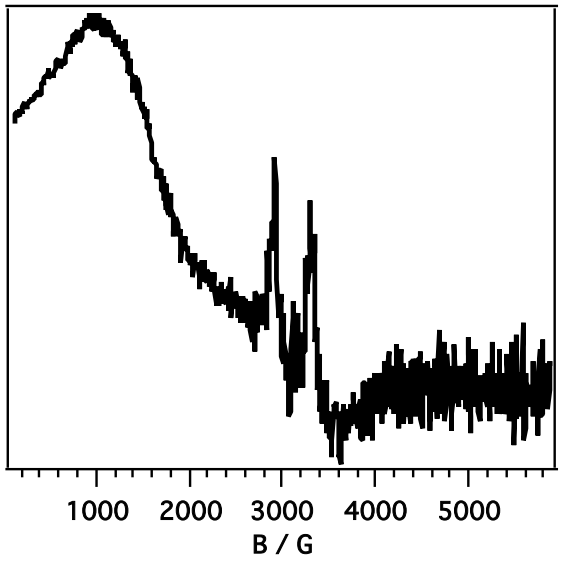

6.4.17. {[NiL^3]$_2$-μ-Fe}(BF$_4$)$_2$. Analogous to [NiCuL^3](BF$_4$)$_2$. Suitable crystals were grown from diffusion of diethyl ether into a saturated solution in acetonitrile. Single crystals for X-ray analysis were grown from diffusion of diethyl ether into a saturated solution in

acetonitrile. Isomorphous crystals with $\{[NiL^3]_2$-μ-Mn$\}(BF_4)_2$ indicate dimerization. ESI-MS *m/z*: 543.65 (M_2^{2+}/2), 684.12 (M*2CH_3CN*1CH_3OH^+). No EA was collected.

6.4.18. $\{[NiL^3]_2$-μ-Mn$\}(BF_4)_2$.. Analogous to $[NiCuL^3](BF_4)_2$. Suitable crystals were grown from diffusion of diethyl ether into a saturated solution in acetonitrile. EPR (DMF/THF 1:1, 77 K): g_1 = 8.53, g_2 = 4.78, g_3 = 2.84. ESI-MS *m/z*: 543.67 (M_2^{2+}/2), 684.11 (M*2CH_3CN*1CH_3OH^+). No EA was collected.

6.5. STEP-WISE HETEROBIMETALLICS

6.5.1. Fsal-2 / L⁴'

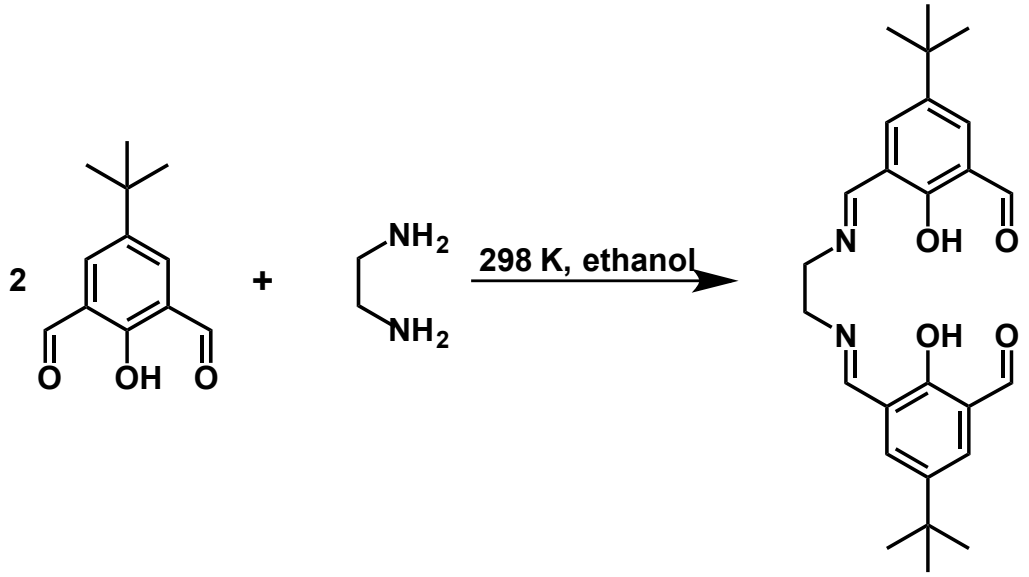

4-*tert*-butyl-2,6-diformylphenol (1.03 mmol) was dissolved in ethanol. Ethylenediamine (0.666 mmol) was added and the yellow solution was stirred for 5 min. The solution was concentrated under vacuum and the precipitate was filtered, dried and washed with ethanol. For a second crop, the remaining filtrate is evaporated to dryness, where the solid

is collected and washed with ethanol to afford clean product. ^{1}H NMR (500 MHz, $CDCl_3$): 10.51 (2H, s), 8.45 (2H, d), 7.90 (2H, d), 7.49 (2H, d), 4.00 (4H, m), 1.28 (18H, s).

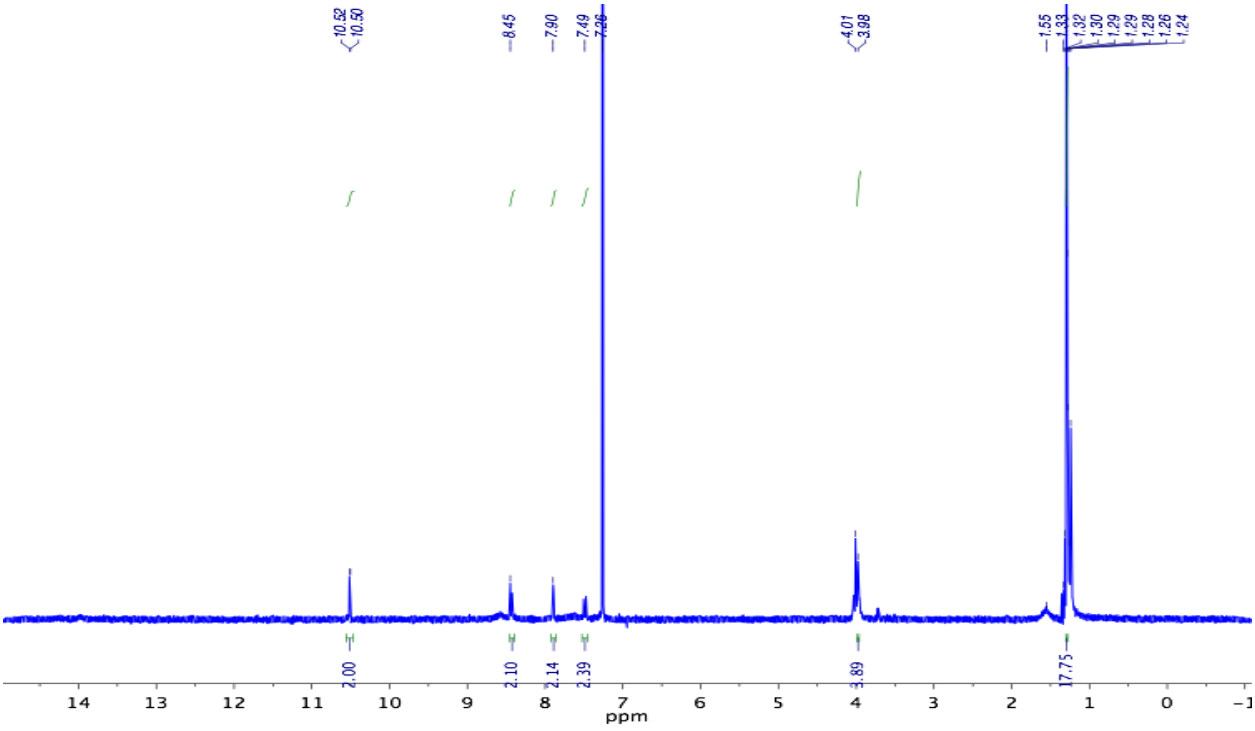

6.5.2. Fsal-2-Zn / ZnL⁴'

To a warm ethanolic solution of Fsal-2 (0.145 mmol) was added solid $Zn(OAc)_2*2H_2O$ (0.148 mmol). The reaction was allowed to stir an additional 5 minutes. The resulting precipitate was then filtered and washed with ethanol to yield yellow microcrystals. ^{1}H NMR (500 MHz, $CDCl_3$): 10.39 (2H, s), 8.28 (2H, s), 7.58 (2H, s), 7.16 (2H, s), 1.58 (4H, s), 1.16 (18H, s).

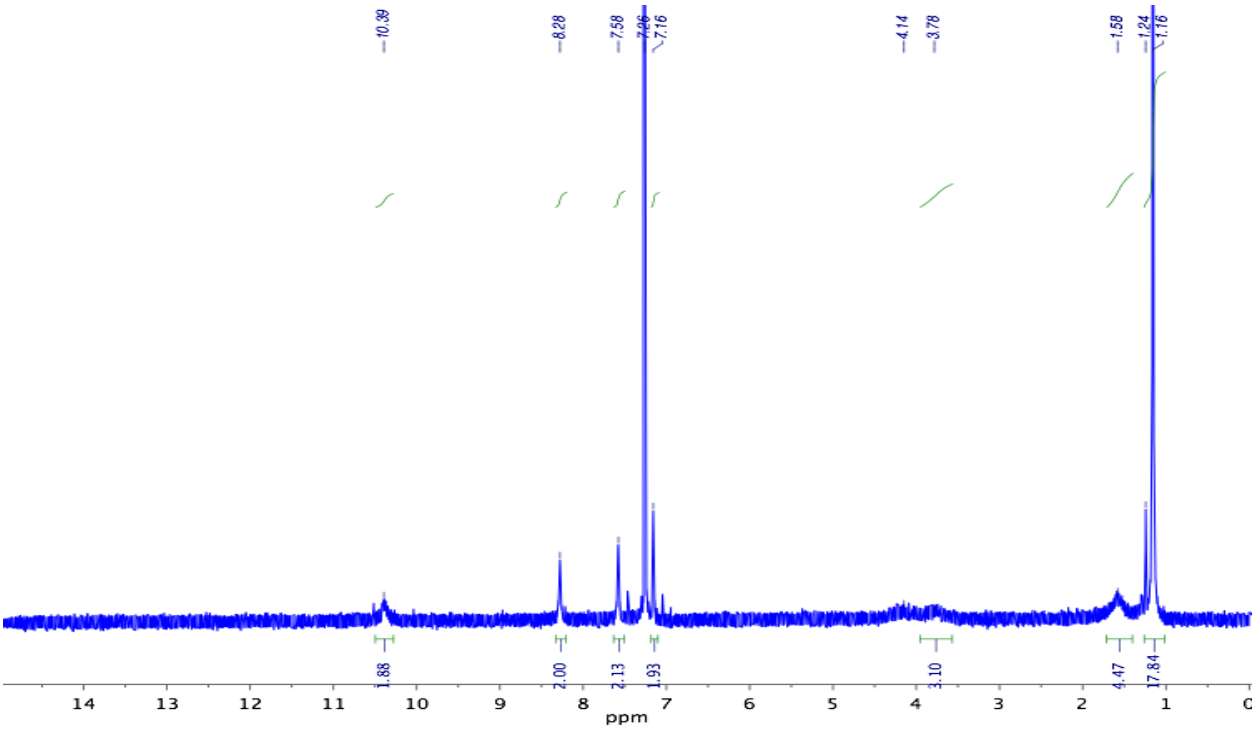

6.5.3. Fsal-2-Ni / NiL$^{4'}$

Analogous to Fsal-2-Zn to yield orange microcrystals. ^{1}H NMR (500 MHz, $CDCl_3$): 10.53 (2H, s), 7.93 (2H, s), 7.58 (2H, s), 7.34 (2H, s), 1.54 (4H, s), 1.27 (18H, s).

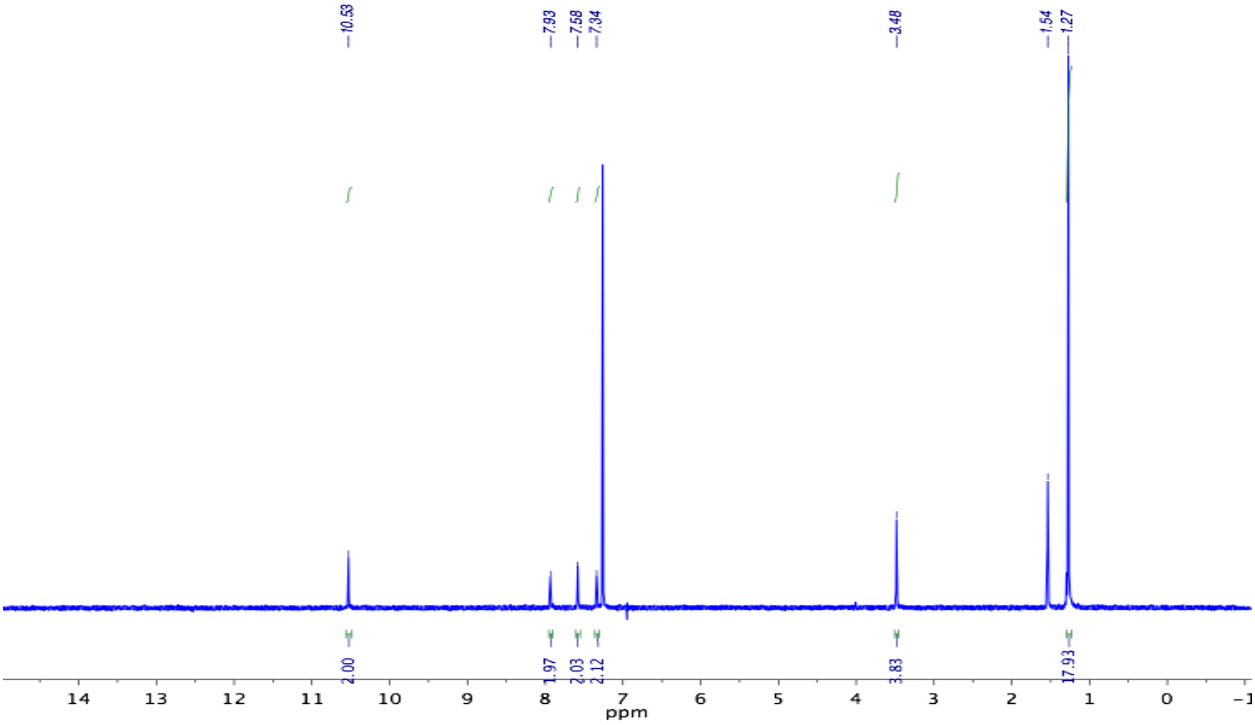

6.5.4. NiL⁴

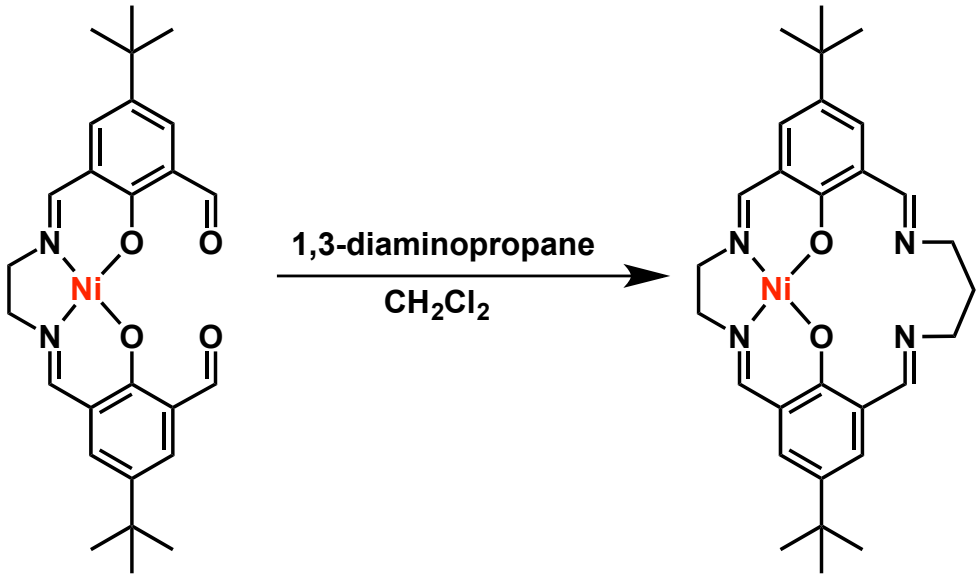

Fsal-2-Ni (0.225 mmol) was dissolved in 5 mL chloroform. 1,3-diaminopropane (0.425 mmol) was added dropwise with stirring. The solution was stirred for 10 min and dried

under vacuum. ^{1}H NMR (500 MHz, $CDCl_3$): 8.91 (2H, s), 8.08 (2H, s), 7.53 (2H, s), 7.13 (2H, s), 1.26 (18H, s). ESI-MS *m/z*: 531.16 ($M\text{-}H^+$).

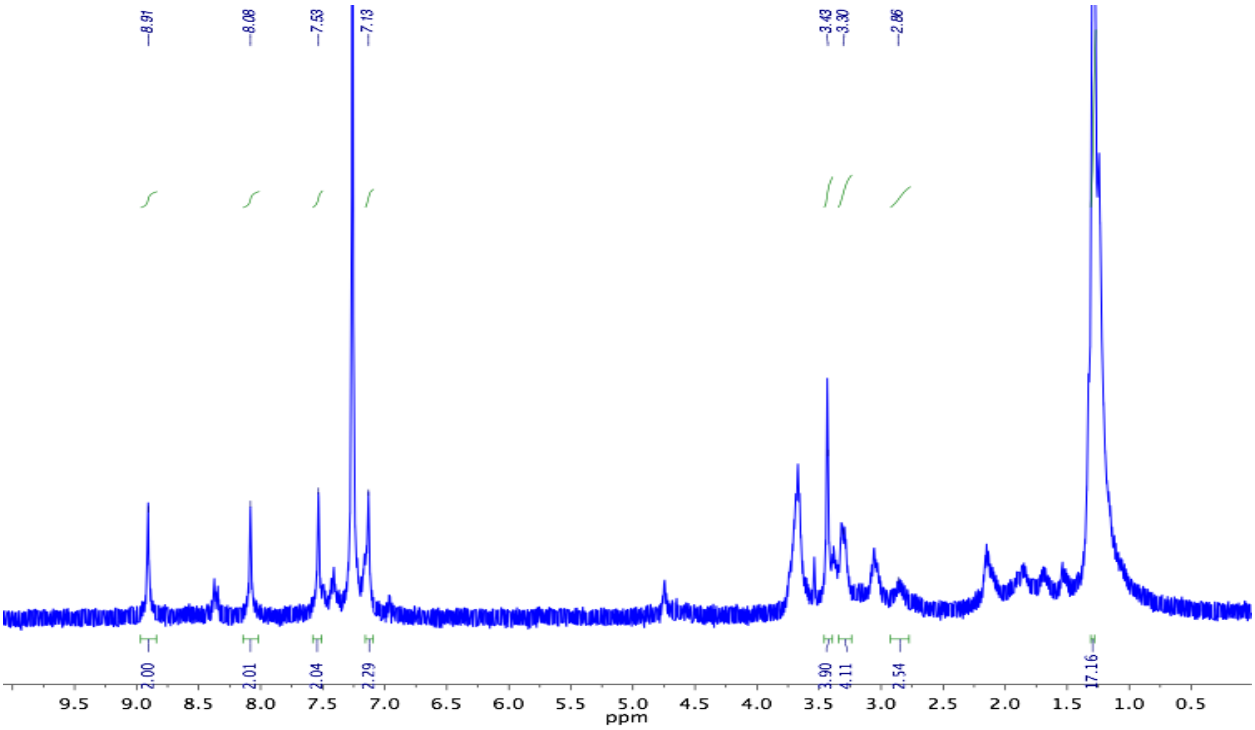

6.5.5. Fsal-3

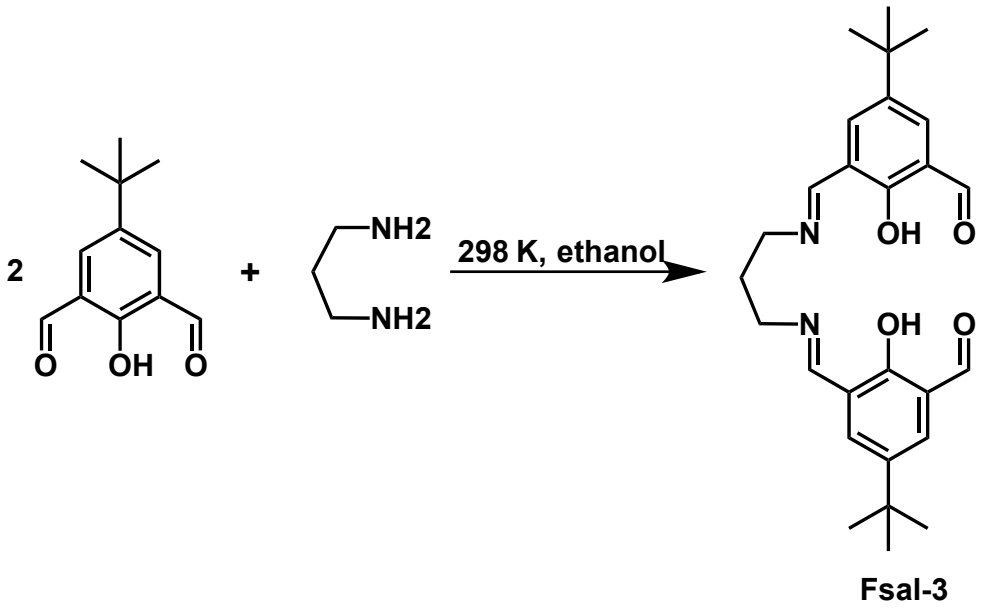

Fsal-3

4-*tert*-butyl-2,6-diformylphenol (1.84 mmol) was dissolved in ethanol. 1,3-diaminopropane (0.920 mmol) was added and the yellow solution was stirred for 5 min and left to stand overnight. The resulting precipitate was filtered and dried under vacuum. For a second crop, the remaining filtrate is evaporated to dryness, where the solid is collected and washed with ethanol to afford clean product (Yield = 84.3%). ^{1}H NMR (500 MHz, d^{6}-DMSO): 14.80 (2H, s), 10.36 (2H, s), 8.71 (2H, s), 7.75 (4H, dd), 3.75 (4H, t), 2.11 (2H, quin.), 1.24 (18H, s).

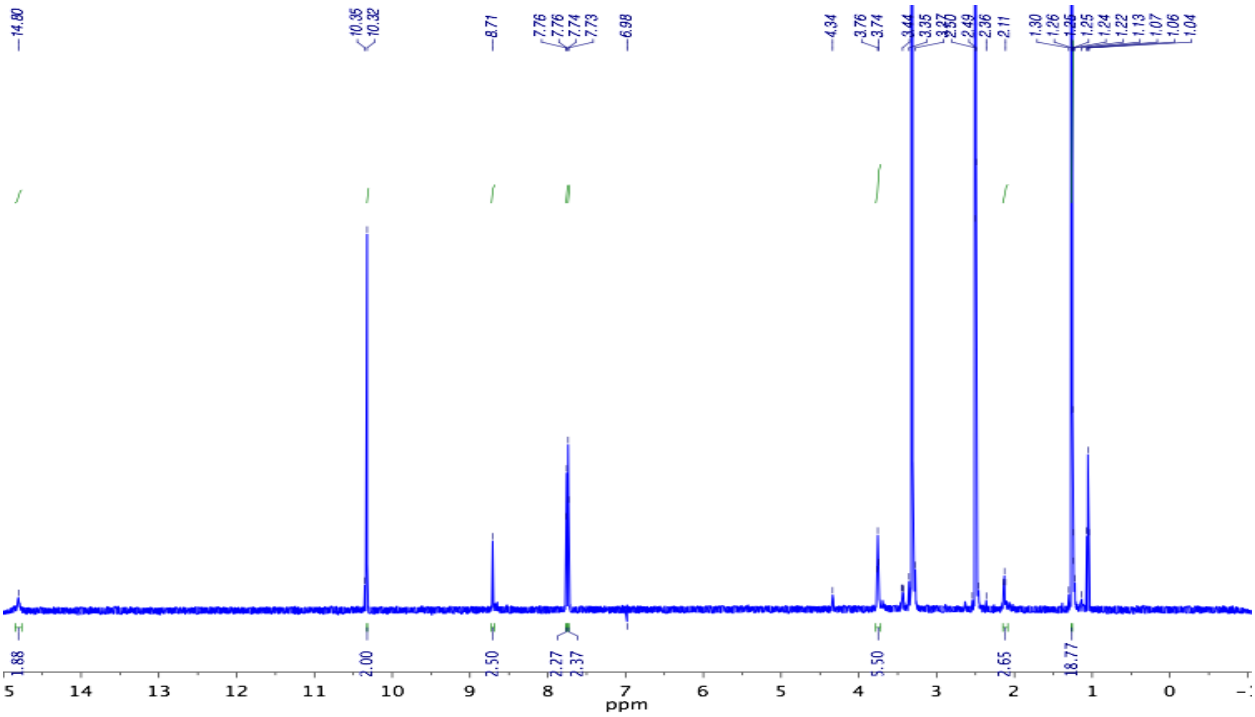

6.5.6. Fsal-3-Zn. To a warm ethanolic solution of Fsal-3 (0.107 mmol) was added solid $Zn(OAc)_2$*$2H_2O$ (0.140 mmol). The reaction was allowed to stir an additional 5 minutes and left to stand overnight, whereby crystals that precipitated were filtered and washed with ethanol. ^{1}H NMR (500 MHz, d^{6}-DMSO): 10.47 (2H, s), 8.37 (2H, s), 7.58 (4H, dd), 3.82 (4H, t), 1.98 (2H, quin.), 1.18 (18H, s).

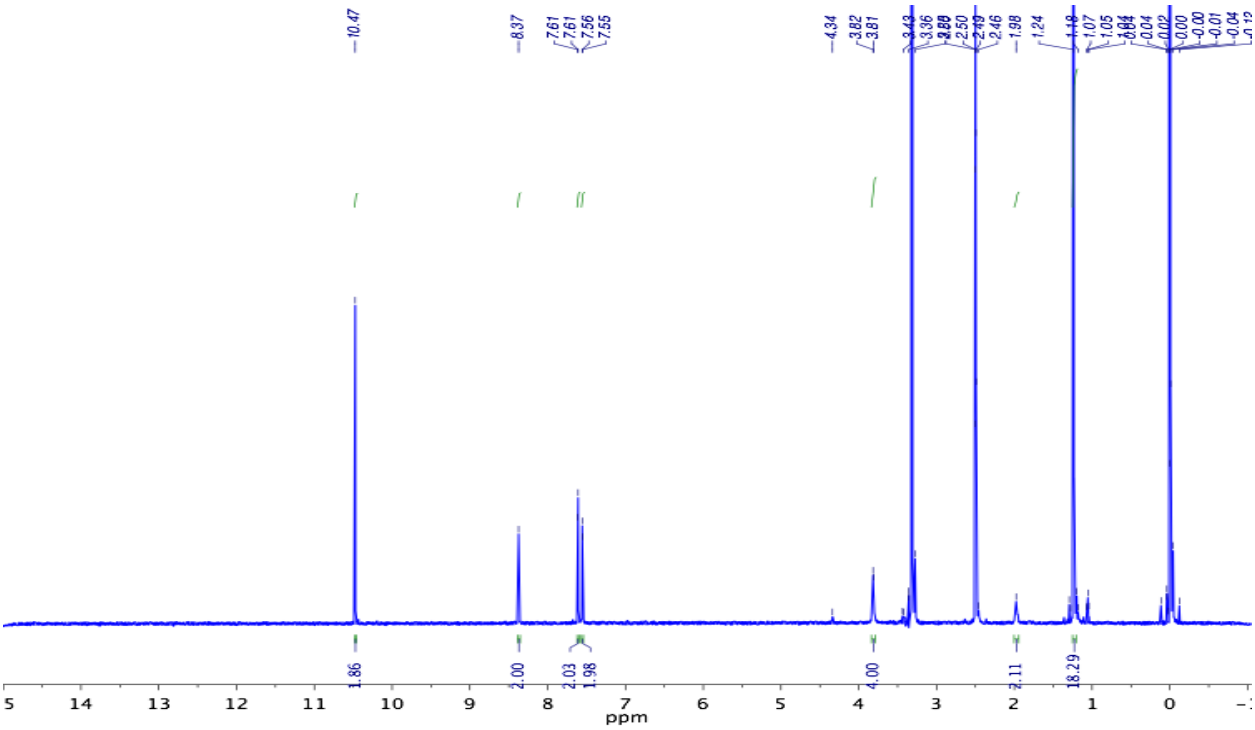

6.5.7. Fsal-3-Cu. Analogous to Fsal-3-Zn. Olive green crystals began to form immediately upon the addition of $Cu(OAc)_2*H_2O$. ESI-MS *m/z*: 534.20 ($M\text{-}Na^+$). Anal. Calc. (Found) (%): C 63.33 (63.36), H 6.30 (6.27), N 5.47 (5.46). X-band EPR (DMF/THF 1:1, 77 K): $g_1 = 2.05$; $A_1 = 1.85 \times 10^{-6}$ cm^{-1}

6.5.8. CuL^2

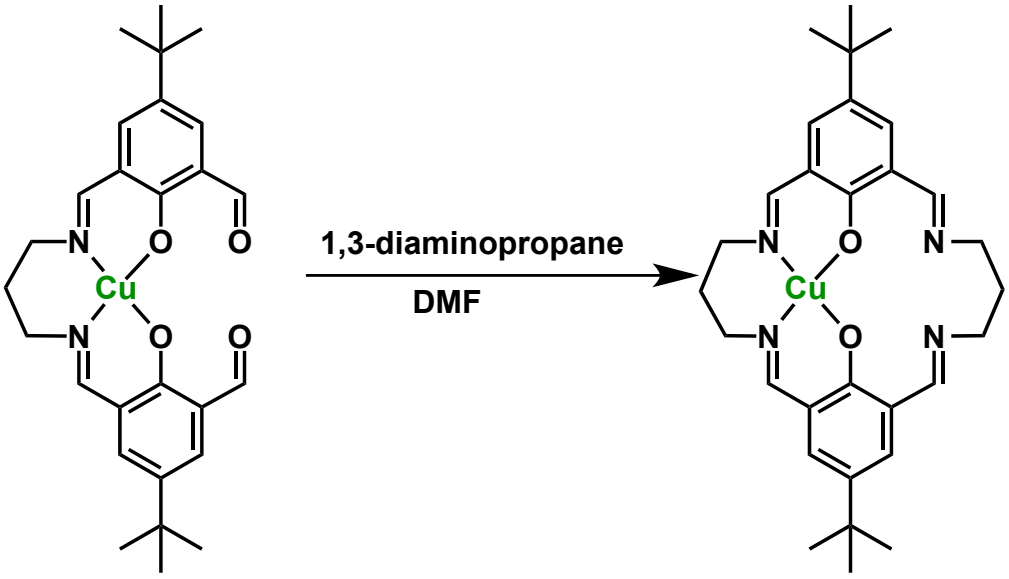

A solution containing Fsal-3-Cu in DMF is heated to 70°C. To this solution is added 1,3-diaminopropane and the solution is stirred for 10 min. The solution is allowed to sit overnight, where dark olive green crystals had formed. These crystals were filtered, washed with water and dried under vacuum. ESI-MS *m/z*: 550.16 ($M\text{-}H^+$); X-band EPR (DMF/THF 1:1, 77 K): $g_1 = 2.04$; $A_1 = 1.78 \times 10^{-6}$ cm^{-1}. No EA was collected.

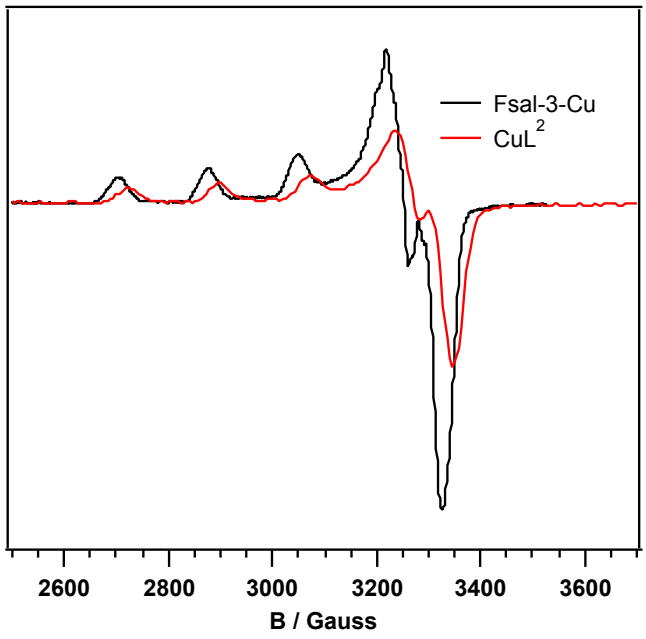

6.5.10. $[Ni_2L^2](BF_4)_2$. To a solution Fsal-3-Ni (0.0830 mmol) in CH_3CN was added $[Ni(H_2O)_6](BF_4)_2$ (0.0876 mmol) in CH_3CN, in which the solution becomes a burnt orange color. After stirring at room temperature for 10 min, 1,3-diaminopropane (0.0830 mmol) was added dropwise and the solution was left to stir for 0.5 hr. The solvent was removed *en vacuo* to produce a golden brown powder. ESI-MS *m/z*: 301.03 ($M^{2+}/2$), 321.49 ($M^*CH_3CN^{2+}/2$), 716.12 ($M^*2CH_3CN^*CH_3OH^+$). CV (Bu_4NBF_4): $E_{1/2}$ or $E_{c,}$ if irreversible, V vs $Fc^{+/0}$ = 1.24 ($Ni^{III}Ni^{III}$) 1.04 ($Ni^{III}Ni^{II}$) -1.44 V ($Ni^{I}Ni^{II}$), -1.75 V ($Ni^{I}Ni^{I}$). No EA was collected.

6.5.11. $[Co_2L^2](BF_4)_2$. Analogous to $[Ni_2L^2](BF_4)_2$ via the method described above. ESI *m/z*: 302.02 ($M^{2+}/2$), 322.59 ($M^*CH_3CN^{2+}/2$), 677.19 ($M^*CH_3CN^*CH_3OH^+$). E_c, V vs $Fc^{+/0}$ = -1.55 V ($Co^{I}Co^{II}$), -1.89 V ($Co^{I}Co^{I}$). No EA was collected.

References

(1) Engelhaupt, E. *Environ. Sci. Technol.* **2008**, *42*, 7548.
(2) Grossmann, W. D.; Steininger, K.; Grossmann, I.; Magaard, L. *Environ. Sci. Technol.* **2009**, *43*, 6421.
(3) Appel, A. M.; Bercaw, J. E.; Bocarsly, A. B.; Dobbek, H.; DuBois, D. L.; Dupuis, M.; Ferry, J. G.; Fujita, E.; Hille, R.; Kenis, P. J. A.; Kerfeld, C. A.; Morris, R. H.; Peden, C. H. F.; Portis, A. R.; Ragsdale, S. W.; Rauchfuss, T. B.; Reek, J. N. H.; Seefeldt, L. C.; Thauer, R. K.; Waldrop, G. L. *Chem. Rev.* **2013**.
(4) Conti, J.; Holtber, P. *International Energy Outlook 2011*, U.S. Energy Information Administration.
(5) Barnhart, C. J.; Dale, M.; Brandt, A. R.; Benson, S. M. *Energy Environ. Sci.* **2013**, *6*, 2804.
(6) Dr. Pieter Tans, NOAA/ESRL (www.esrl.noaa.gov/gmd/ccgg/trends/) and Dr. Ralph Keeling, Scripps Institution of Oceanography (scrippsco2.ucsd.edu/).
(7) Xie, Y.; Wang, T.; Liu, X.; Zou, K.; Deng, W. *Nature Comm.* **2013**, *4*, 1.
(8) Schulz, H. *Appl. Catal., A* **1999**, *186*, 3.
(9) Fischer-Tropsch synthesis, National Energy Technology Laboratory. *http://www.netl.doe.gov/research/coal/energy-systems/gasification/gasifipedia/ftsynthesis.*
(10) Costentin, C.; Drouet, S.; Robert, M.; Savéant, J.-M. *J. Am. Chem. Soc.* **2012**, *134*, 11235.
(11) Christensen, P. A.; Hamnett, A.; Muir, A. V. G.; Freeman, N. A. *J. Electroanal. Chem* **1990**, *288*, 197.
(12) Isse, A. A.; Gennaro, A.; Vianello, E.; Floriani, C. *J. Mol. Cat.* **1991**, *70*, 197.
(13) Ishida, H.; Fujiki, K.; Ohba, T.; Ohkubo, K.; Tanaka, K.; Terada, T.; Tanaka, T. *J. Chem. Soc., Dalton Trans.* **1990**, 2155.
(14) Ishida, H.; Tanaka, K.; Tanaka, T. *Organometallics* **1987**, *6*, 181.
(15) Majumdar, A. *Dalton Trans.* **2014**, *43*, 12135.
(16) Camara, J. M.; Rauchfuss, T. B. *J. Am. Chem. Soc.* **2011**, *133*, 8098.
(17) Camara, J. M.; Rauchfuss, T. B. *Nat Chem* **2012**, *4*, 26.
(18) Lai, C. H.; Reibenspies, J. H.; Darensbourg, M. Y. *Angew. Chem. Int. Edn Engl.* **1996**, *35*, 2390.
(19) Liu, T.; Darensbourg, M. Y. *J. Am. Chem. Soc.* **2007**, *129*, 7008.
(20) Dubois, M.; Dubois, D. L. *Chem. Soc. Rev.* **2009**, *38*, 62.
(21) Jain, A.; Lense, S.; Linehan, J. C.; Raugei, S.; Cho, H.; DuBois, D. L.; Shaw, W. J. *Inorg. Chem.* **2011**, *50*, 4073.
(22) Liu, T.; DuBois, D. L.; Bullock, R. M. *Nat Chem* **2013**, *5*, 228.
(23) Rakowski Dubois, M.; Dubois, D. L. *Acc. Chem. Res.* **2009**, *42*, 1974.
(24) Smith, S. E.; Yang, J. Y.; DuBois, D. L.; Bullock, R. M. *Angew. Chem.* **2012**, *124*, 3206.
(25) Amin, M.; Vogt, L.; Vassiliev, S.; Rivalta, I.; Sultan, M. M.; Bruce, D.; Brudvig, G. W.; Batista, V. S.; Gunner, M. R. *J. Phys. Chem. B* **2013**, *117*, 6217.
(26) Young, K. J.; Takase, M. K.; Brudvig, G. W. *Inorg. Chem.* **2013**, *52*, 7615.

(27) Doukov, T. I.; Iverson, T. M.; Seravalli, J.; Ragsdale, S. W.; Drennan, C. L. *Science* **2002**, *298*, 567.
(28) Weber, K.; Erdem, Ö. F.; Bill, E.; Weyhermüller, T.; Lubitz, W. *Inorg. Chem.* **2014**, *53*, 6329.
(29) Costentin, C.; Drouet, S.; Robert, M.; Savéant, J.-M. *Science* **2012**, *338*, 90.
(30) Costentin, C.; Passard, G.; Robert, M.; Savéant, J.-M. *PNAS* **2014**, *111*, 14990.
(31) Costentin, C.; Robert, M.; Savéant, J.-M.; Tatin, A. *PNAS* **2015**, *112*, 6882.
(32) Barton, B. E.; Olsen, M. T.; Rauchfuss, T. B. *J. Am. Chem. Soc.* **2008**, *130*, 16834.
(33) Barton, B. E.; Rauchfuss, T. B. *J. Am. Chem. Soc.* **2010**, *132*, 14877.
(34) Fontecilla-Camps, J. C.; Amara, P.; Cavazza, C.; Nicolet, Y.; Volbeda, A. *Nature* **2009**, *460*, 814.
(35) Fontecilla-Camps, J. C.; Volbeda, A.; Cavazza, C.; Nicolet, Y. *Chem. Rev.* **2007**, *107*, 4273.
(36) Brecht, M.; van Gastel, M.; Buhrke, T.; Friedrich, B.; Lubitz, W. *J. Am. Chem. Soc.* **2003**, *125*, 13075.
(37) Lubitz, W.; Reijerse, E.; van Gastel, M. *Chem. Rev.* **2007**, *107*, 4331.
(38) Parkin, A.; Seravalli, J.; Vincent, K. A.; Ragsdale, S. W.; Armstrong, F. A. *J. Am. Chem. Soc.* **2007**, *129*, 10328.
(39) Jeoung, J.-H.; Dobbek, H. *Science* **2007**, *318*, 1461.
(40) Dobbek, H.; Svetlitchnyi, V.; Gremer, L.; Huber, R.; Meyer, O. *Science* **2001**, *293*, 1281.
(41) Dobbek, H.; Gremer, L.; Kiefersauer, R.; Huber, R.; Meyer, O. *PNAS* **2002**, *99*, 15971.
(42) Stein, B. W.; Kirk, M. L. *Chem. Commun.* **2014**, *50*, 1104.
(43) Takuma, M.; Ohki, Y.; Tatsumi, K. *Inorg. Chem.* **2005**, *44*, 6034.
(44) Groysman, S.; Majumdar, A.; Zheng, S.-L.; Holm, R. H. *Inorg. Chem.* **2010**, *49*, 1082.
(45) Ishida, H.; Tanaka, H.; Tanaka, K.; Tanaka, T. *J. Chem. Soc., Chem. Commun.* **1987**, 131.
(46) Bolinger, C. M.; Sullivan, B. P.; Conrad, D.; Gilbert, J. A.; Story, N.; Meyer, T. J. *J. Chem. Soc., Chem. Commun.* **1985**, 796.
(47) Bruce, M. R. M.; Megehee, E.; Sullivan, B. P.; Thorp, H.; O'Toole, T. R.; Downard, A.; Meyer, T. J. *Organometallics* **1988**, *7*, 238.
(48) Raebiger, J. W.; Turner, J. W.; Noll, B. C.; Curtis, C. J.; Miedaner, A.; Cox, B.; DuBois, D. L. *Organometallics* **2006**, *25*, 3345.
(49) Bolinger, C. M.; Story, N.; Sullivan, B. P.; Meyer, T. J. *Inorg. Chem.* **1988**, *27*, 4582.
(50) Slater, S.; Wagenknecht, J. H. *J. Am. Chem. Soc.* **1984**, *106*, 5367.
(51) Szymaszek, A.; Pruchnik, F. P. *J. Organomet. Chem.* **1989**, *376*, 133.
(52) Hawecker, J.; Lehn, J.-M.; Ziessel, R. *J. Chem. Soc., Chem. Commun.* **1984**, 328.
(53) Sullivan, B. P.; Bolinger, C. M.; Conrad, D.; Vining, W. J.; Meyer, T. J. *J. Chem. Soc., Chem. Commun.* **1985**, 1414.
(54) Hawecker, J.; Lehn, J.-M.; Ziessel, R. *Helv. Chim. Acta.* **1986**, *69*, 1990.
(55) Breikss, A. I.; Abruña, H. D. *J. Electroanal. Chem* **1986**, *201*, 347.
(56) Hawecker, J.; Lehn, J.-M.; Ziessel, R. *J. Chem. Soc., Chem. Commun.* **1983**, 536.
(57) Therrien, J. A.; Wolf, M. O.; Patrick, B. O. *Inorg. Chem.* **2014**, *53*, 12962.

(58) Fujita, E.; Creutz, C.; Sutin, N.; Brunschwig, B. S. *Inorg. Chem.* **1993**, *32*, 2657.
(59) Fujita, E.; Creutz, C.; Sutin, N.; Szalda, D. J. *J. Am. Chem. Soc.* **1991**, *113*, 343.
(60) Froehlich, J. D.; Kubiak, C. P. *Inorg. Chem.* **2012**, *51*, 3932.
(61) Schmidt, M. H.; Miskelly, G. M.; Lewis, N. S. *J. Am. Chem. Soc.* **1990**, *112*, 3420.
(62) Fujita, E.; Furenlid, L. R.; Renner, M. W. *J. Am. Chem. Soc.* **1997**, *119*, 4549.
(63) DuBois, D. L.; Miedaner, A.; Haltiwanger, R. C. *J. Am. Chem. Soc.* **1991**, *113*, 8753.
(64) Bernatis, P. R.; Miedaner, A.; Haltiwanger, R. C.; DuBois, D. L. *Organometallics* **1994**, *13*, 4835.
(65) Dubois, D. L. *Comments Inorg. Chem.* **1997**, *19*, 307.
(66) Bailes, R. H.; Calvin, M. *J. Am. Chem. Soc.* **1947**, *69*, 1886.
(67) Pfeiffer, P.; Breith, E.; Lübbe, E.; Tsumaki, T. *Justus Liebigs Annalen der Chemie* **1933**, *503*, 84.
(68) Fachinetti, G.; Floriani, C.; Zanazzi, P. F. *J. Am. Chem. Soc.* **1978**, *100*, 7405.
(69) Fachinetti, G.; Floriani, C.; Zanazzi, P. F.; Zanzari, A. R. *Inorg. Chem.* **1979**, *18*, 3469.
(70) Floriani, C.; Fachinetti, G. *J. Chem. Soc., Chem. Commun.* **1974**, *0*, 615.
(71) Gambarotta, S.; Arena, F.; Floriani, C.; Zanazzi, P. F. *J. Am. Chem. Soc.* **1982**, *104*, 5082.
(72) Pearce, D. J.; Pletcher, D. *J. Electroanal. Chem* **1986**, *197*, 317.
(73) Pilkington, N. H.; Robson, R. *Aust. J. Chem.* **1970**, *23*, 2225.
(74) Diehl, H.; Hach, C. C.; Bailar, J. C. In *Inorganic Syntheses*; John Wiley & Sons, Inc.: 2007, p 196.
(75) Brooker, S.; Croucher, P. D.; Roxburgh, F. M. *J. Chem. Soc., Dalton Trans.* **1996**, 3031.
(76) Brooker, S.; D. Croucher, P.; C. Davidson, T.; S. Dunbar, G.; James McQuillan, A.; B. Jameson, G. *Chem. Commun.* **1998**, 2131.
(77) Brooker, S.; de Geest, D. J.; Dunbar, G. S. *Inorg. Chim. Acta.* **1998**, *282*, 222.
(78) Fernández-g, J.; Acevedo-Arauz, E.; Cetina-Rosado, R.; Toscano, R.; Macías-ruvalcaba, N.; Aguilar-martínez, M. *Trans. Met. Chem.* **1999**, *24*, 18.
(79) Gupta, S.; Raina, D. *Trans. Met. Chem.* **1997**, *22*, 372.
(80) Atkins, A. J.; Blake, A. J.; Schroder, M. *J. Chem. Soc., Chem. Commun.* **1993**, 1662.
(81) Branscombe, N. D. J.; Blake, A. J.; Marin-Becerra, A.; Li, W.-S.; Parsons, S.; Ruiz-Ramirez, L.; Schroder, M. *Chem. Commun.* **1996**, 2573.
(82) Nation, D. A.; Reibenspies, J. H.; Taylor, M. R.; Wainwright, K. P. *Inorg. Chim. Acta.* **1997**, *258*, 161.
(83) Atkins, A. J.; Black, D.; Blake, A. J.; Marin-Becerra, A.; Parsons, S.; Ruiz-Ramirez, L.; Schroder, M. *Chem. Commun.* **1996**, 457.
(84) Lambert, S. L.; Hendrickson, D. N. *Inorg. Chem.* **1979**, *18*, 2683.
(85) Spiro, C. L.; Lambert, S. L.; Smith, T. J.; Duesler, E. N.; Gagne, R. R.; Hendrickson, D. N. *Inorg. Chem.* **1981**, *20*, 1229.
(86) Gagne, R. R.; Spiro, C. L.; Smith, T. J.; Hamann, C. A.; Thies, W. R.; Shiemke, A. D. *J. Am. Chem. Soc.* **1981**, *103*, 4073.
(87) Eckshtain-Levi, M.; Lavi, R.; Yufit, D.; Orio, M.; Wanke, R.; Benisvy, L. *Dalton Trans.* **2012**, *41*, 12457.

(88) Zhou, H.-B.; Wang, H.-S.; Chen, Y.; Xu, Y.-L.; Song, X.-J.; Song, Y.; Zhang, Y.-Q.; You, X.-Z. *Dalton Trans.* **2011**, *40*, 5999.
(89) Spodine, E.; Valencia-Gálvez, P.; Fuentealba, P.; Manzur, J.; Ruiz, D.; Venegas-Yazigi, D.; Paredes-García, V.; Cardoso-Gil, R.; Schnelle, W.; Kniep, R. *J. Solid State Chem.* **2011**, *184*, 1129.
(90) Li, Z.; Jablonski, C. *Inorg. Chem.* **2000**, *39*, 2456.
(91) Thompson, L. K.; Mandal, S. K.; Tandon, S. S.; Bridson, J. N.; Park, M. K. *Inorg. Chem.* **1996**, *35*, 3117.
(92) Lambert, S. L.; Spiro, C. L.; Gagne, R. R.; Hendrickson, D. N. *Inorg. Chem.* **1982**, *21*, 68.
(93) Mandal, S. K.; Nag, K. *J. Org. Chem.* **1986**, *51*, 3900.
(94) Okawa, H.; Nishio, J.; Ohba, M.; Tadokoro, M.; Matsumoto, N.; Koikawa, M.; Kida, S.; Fenton, D. E. *Inorg. Chem.* **1993**, *32*, 2949.
(95) Mandal, S. K.; Thompson, L. K.; Nag, K.; Charland, J. P.; Gabe, E. J. *Inorg. Chem.* **1987**, *26*, 1391.
(96) Black, D.; Blake, A. J.; Finn, R. L.; Lindoy, L. F.; Nezhadali, A.; Rougnaghi, G.; Tasker, P. A.; Schroder, M. *Chem. Commun.* **2002**, 340.
(97) Dutta, B.; Bag, P.; Adhikary, B.; Flörke, U.; Nag, K. *J. Org. Chem.* **2004**, *69*, 5419.
(98) Okawa, H.; Kida, S. *Bull. Chem. Soc. Jpn.* **1972**, *45*, 1759.
(99) Okawa, H.; Kida, S. *Inorg. Nucl. Chem. Letters* **1971**, *7*, 751.
(100) Aono, T.; Wada, H.; Yonemura, M.; Furutachi, H.; Ohba, M.; Okawa, H. *J. Chem. Soc., Dalton Trans.* **1997**, 3029.
(101) Ōkawa, H.; Furutachi, H.; Fenton, D. E. *Coord. Chem. Rev.* **1998**, *174*, 51.
(102) Okawa, H.; Tadokoro, M.; Aratake, Y.; Ohba, M.; Shindo, K.; Mitsumi, M.; Koikawa, M.; Tomono, M.; Fenton, D. E. *J. Chem. Soc., Dalton Trans.* **1993**, 253.
(103) Torihara, N.; Okawa, H.; Kida, S. *Chem. Lett.* **1978**, *7*, 185.
(104) Wada, H.; Aono, T.; Motoda, K.-i.; Ohba, M.; Matsumoto, N.; Okawa, H. *Inorg. Chim. Acta.* **1996**, *246*, 13.
(105) Lisowski, J. *Inorg. Chim. Acta.* **1999**, *285*, 233.
(106) da Graça Moraes Braga Martin, M.; Vidotti, M.; Nunes, F. S. *Int. J. Hydrogen Energy* **2012**, *37*, 14094.
(107) Shannon, R. *Acta. Crystallogr., Sect. A: Found. Crystallogr.* **1976**, *32*, 751.
(108) Kaljurand, I.; Kütt, A.; Sooväli, L.; Rodima, T.; Mäemets, V.; Leito, I.; Koppel, I. A. *J. Org. Chem.* **2005**, *70*, 1019.
(109) Kolthoff, I. M.; Chantooni, M. K.; Bhowmik, S. *J. Am. Chem. Soc.* **1968**, *90*, 23.
(110) Maran, F.; Celadon, D.; Severin, M. G.; Vianello, E. *J. Am. Chem. Soc.* **1991**, *113*, 9320.
(111) Krivenko, A. G.; Kotkin, A. S.; Simbirtseva, G. V.; Nazmutdinov, R. R.; Glukhov, D. V.; Roznyatovskaya, N. V.; Tsirlina, G. A. *Phys. Chem. Chem. Phys.* **2008**, *10*, 2390.
(112) Kurahashi, T.; Fujii, H. *J. Am. Chem. Soc.* **2011**, *133*, 8307.
(113) Shimazaki, Y.; Stack, T. D. P.; Storr, T. *Inorg. Chem.* **2009**, *48*, 8383.
(114) Azevedo, F.; Freire, C.; de Castro, B. *Polyhedron* **2002**, *21*, 1695.
(115) Hazra, S.; Bhattacharya, S.; Singh, M. K.; Carrella, L.; Rentschler, E.; Weyhermueller, T.; Rajaraman, G.; Mohanta, S. *Inorg. Chem.* **2013**, *52*, 12881.
(116) Dutta, S.; Biswas, P. *Polyhedron* **2012**, *31*, 110.

(117) Huang, D.; Holm, R. H. *J. Am. Chem. Soc.* **2010**, *132*, 4693.
(118) Sun, J.; Tessier, C.; Holm, R. H. *Inorg. Chem.* **2007**, *46*, 2691.
(119) Zhang, X.; Huang, D.; Chen, Y.-S.; Holm, R. H. *Inorg. Chem.* **2012**, *51*, 11017.
(120) Machan, C. W.; Sampson, M. D.; Chabolla, S. A.; Dang, T.; Kubiak, C. P. *Organometallics* **2014**, *33*, 4550.
(121) Evans, D. F. *J. Chem. Soc.* **1959**, 2003.
(122) Okawa, H.; Honda, M.; Kida, S. *Chem. Lett.* **1972**, *1*, 1027.

APPENDIX A

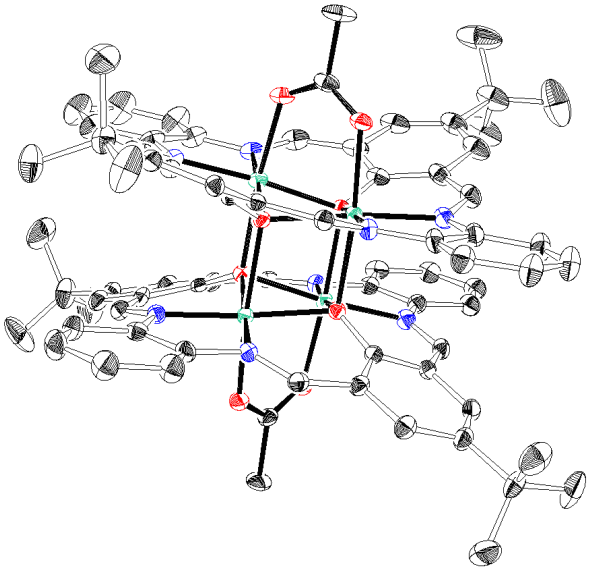

Figure A1. Ortep diagram of [Ni-μ-OAc-NiL^1]$_2$(BF$_4$)$_2$. Ellipsoids are shown at 50% probability. BF$_4$ counter ions have been omitted for clarity.

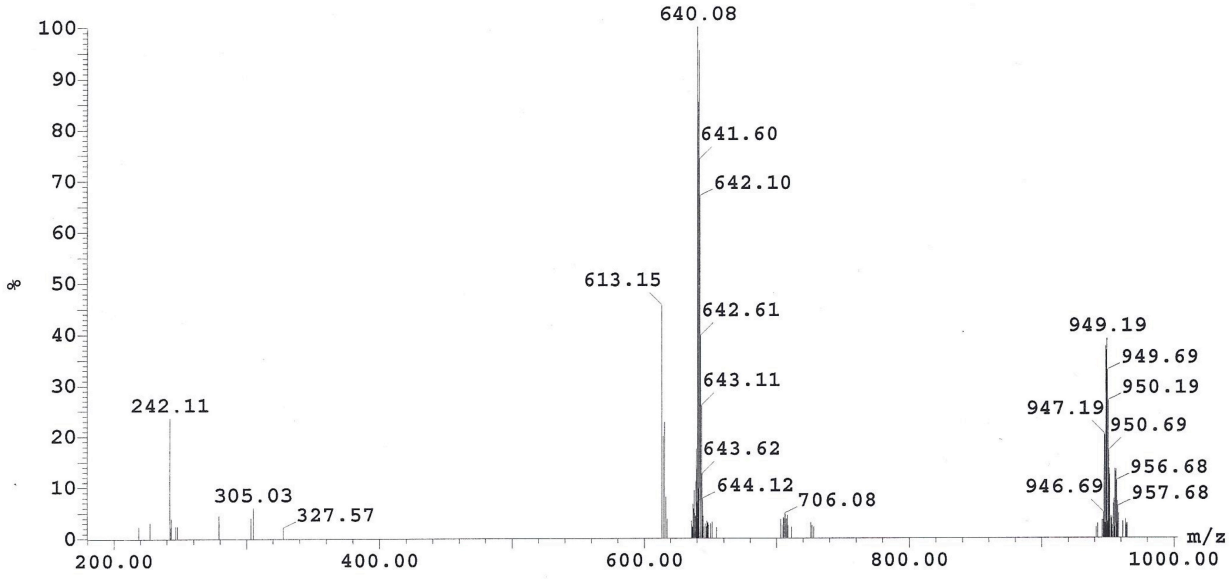

Figure A2. ESI-MS of {[NiL^1]$_2$-μ-Fe}(BF$_4$)$_2$. *m/z* of 640 corresponds to the dimer.

Table A1. Absorbance data for $\{[NiL^1]_2\text{-}\mu\text{-}Fe\}^{n+}$ (n = 0-2) complexes

	λ / nm (ε / $M^{-1}cm^{-1}$)
$\{[NiL^1]_2\text{-}\mu\text{-}Fe\}^{2+}$	365 ($1.2x10^4$), 467 ($6.6x10^3$)
$\{[NiL^1]_2\text{-}\mu\text{-}Fe\}^{+}$	412 ($1.1x10^4$), 515 ($5.6x10^3$), 697 ($2.2x10^3$)
$\{[NiL^1]_2\text{-}\mu\text{-}Fe\}^{0}$	414 ($8.2x10^3$), 516 ($4.4x10^3$), 622 ($2.7x10^3$)

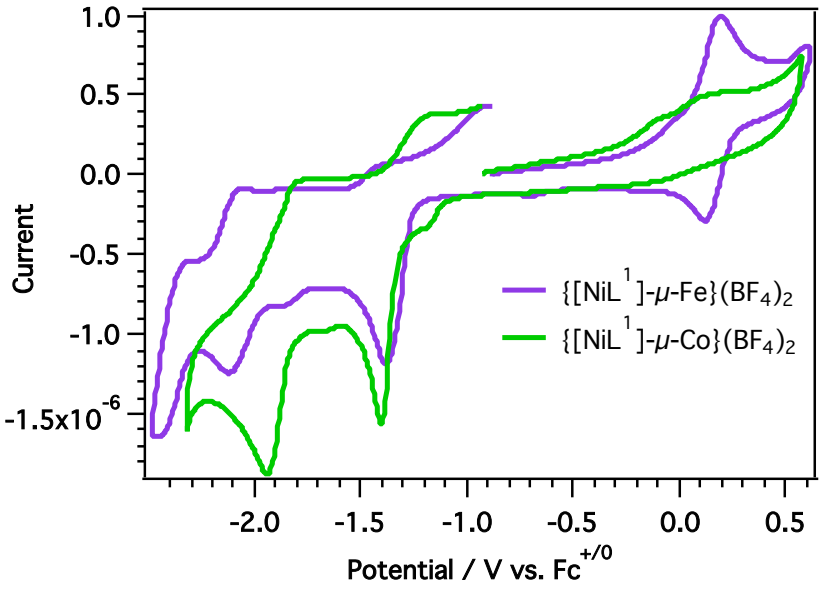

Figure A3. Cyclic voltammograms of $\{[NiL^1]_2\text{-}\mu\text{-}Fe\}(BF_4)_2$ (purple) and $\{[NiL^1]_2\text{-}\mu\text{-}Co\}(BF_4)_2$ (green). 0.2 M Bu_4NBF_4 in DMF, 100 mV/s.

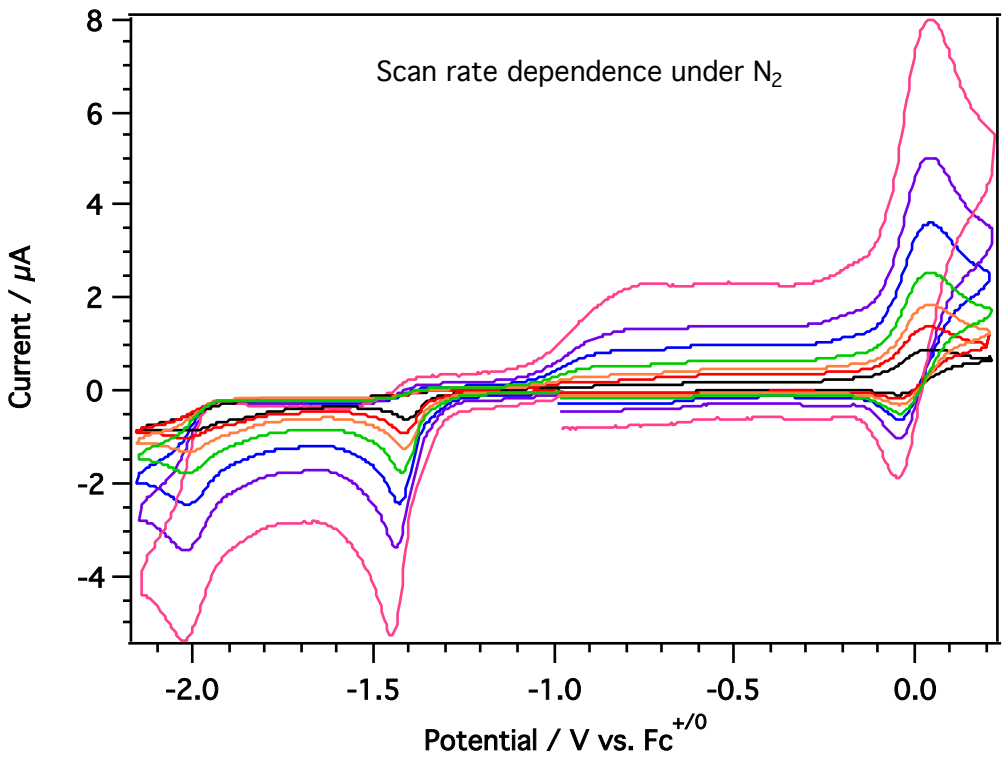

Figure A4. Scan rate dependent cyclic voltammogram of $\{[NiL^1]_2$-μ-Fe$\}(BF_4)_2$. 0.2 M Bu_4BF_4 in DMF, Scan rate ranges from 5 mV/s (Black) to 500 mV/s (pink).

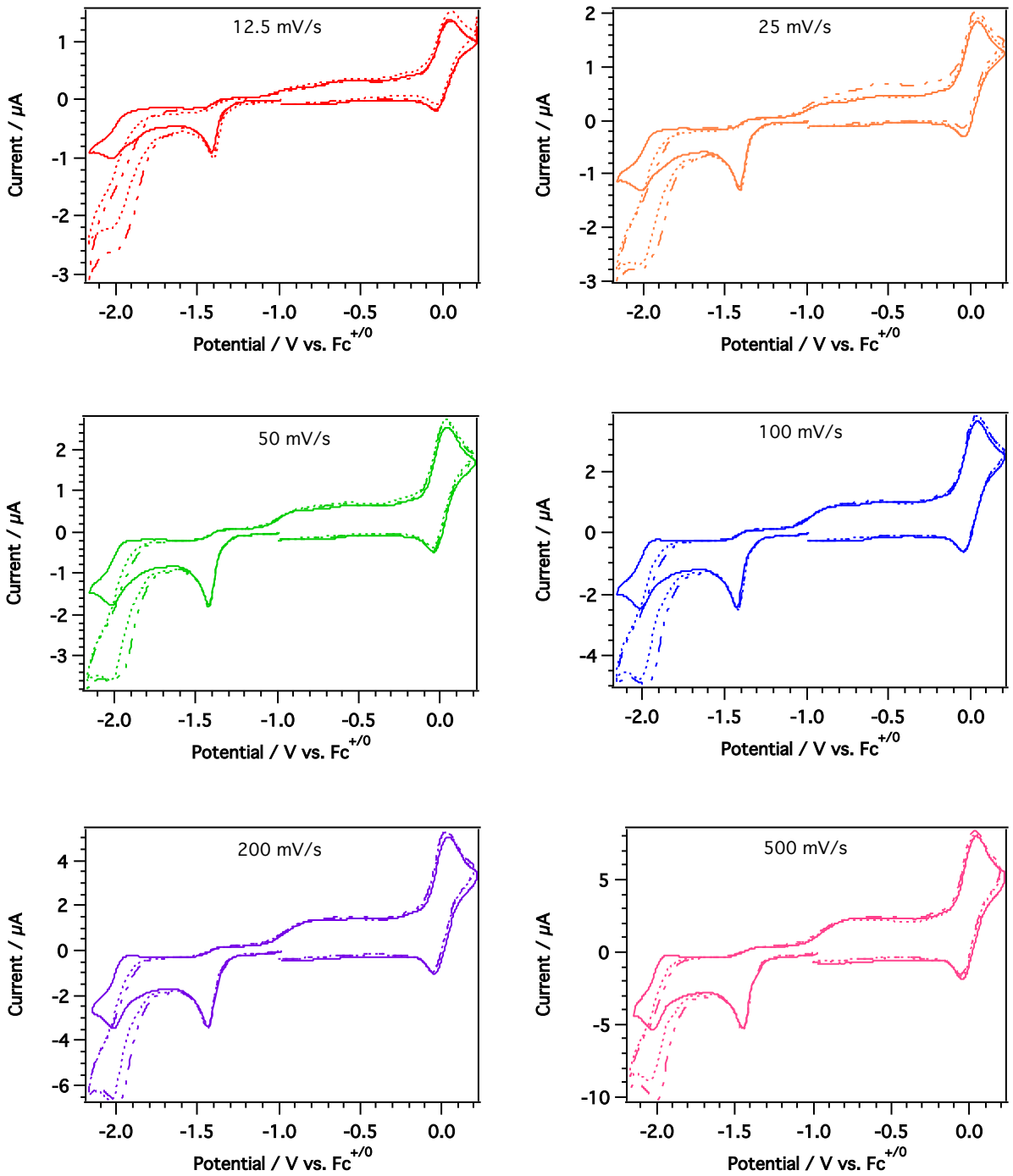

Figure A5. Cyclic voltammograms of $\{[NiL^1]_2$-μ-Fe$](BF_4)_2$ varying by scan rate under N_2 (solid line), CO_2, (dotted line), and the addition of 1 eq. $[NH_4][BF_4]$ under CO_2 (dotted-dashed line). 0.2 M Bu_4NBF_4 in DMF.

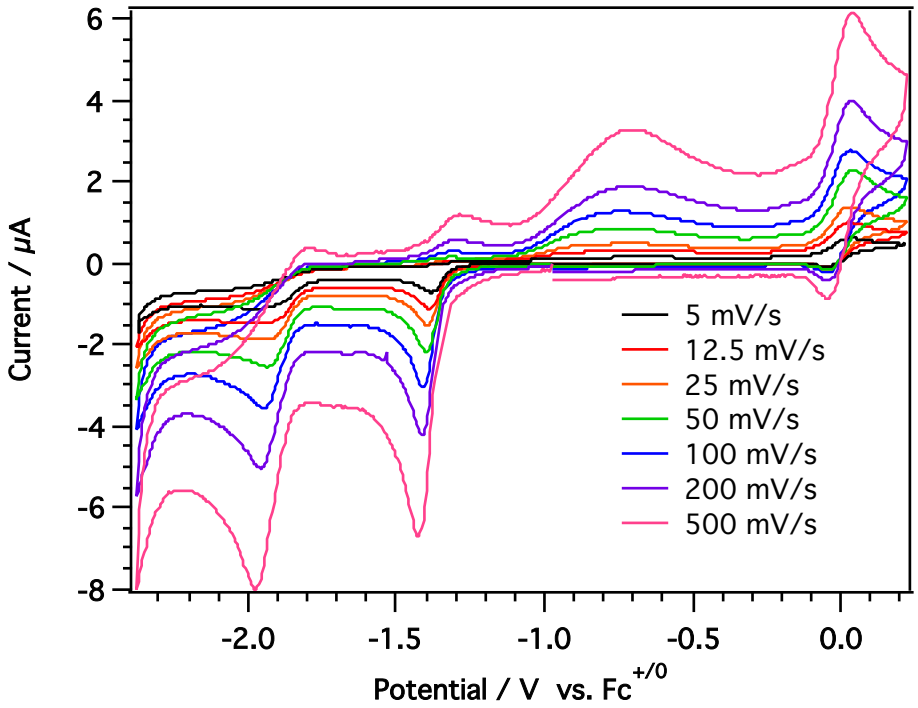

Figure A6. Scan rate dependent cyclic voltammogram of $\{[NiL^1]_2\text{-}\mu\text{-}Co\}(BF_4)_2$. 0.2 M Bu_4BF_4 in DMF, Scan rate ranges from 5 mV/s (Black) to 500 mV/s (pink).

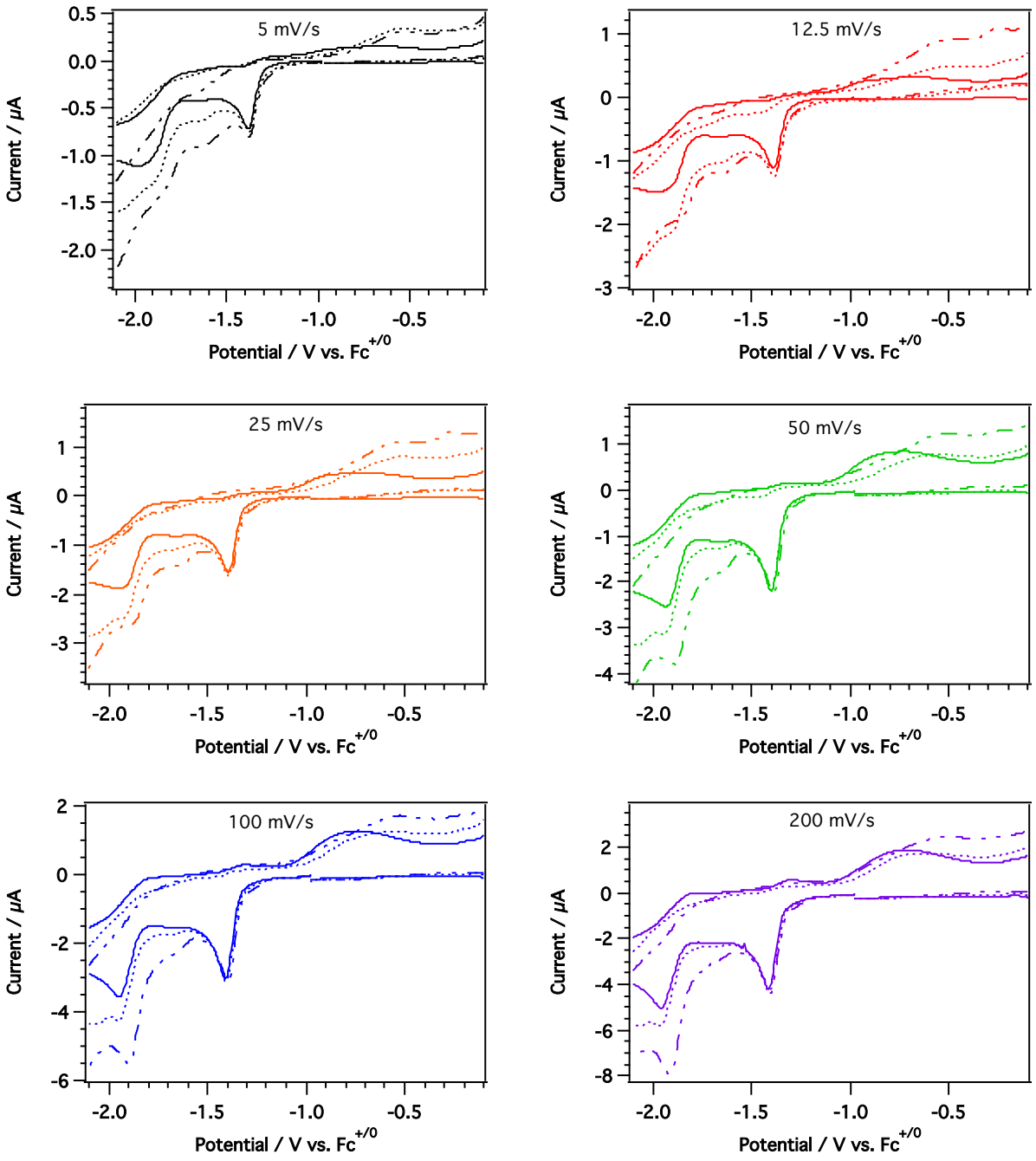

Figure A7. Cyclic voltammograms of $\{[NiL^1]_2$-µ-Co$](BF_4)_2$ varying by scan rate under N_2 (solid line), CO_2, (dotted line), and the addition of 1 eq. $[NH_4][BF_4]$ under CO_2 (dotted-dashed line). 0.2 M Bu_4NBF_4 in DMF.

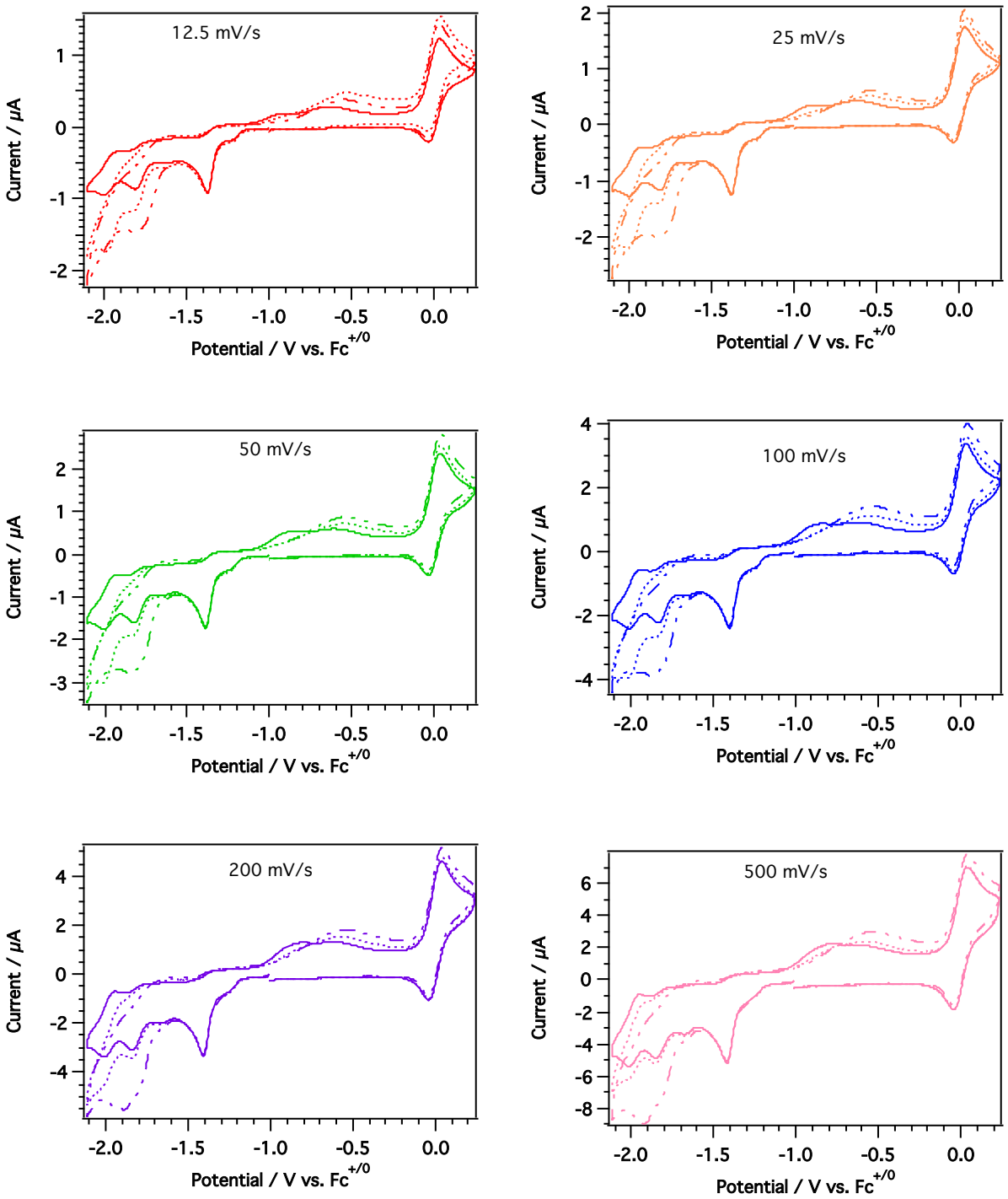

Figure A8. Cyclic voltammograms of $[NiZnL^1](BF_4)_2$ varying by scan rate under N_2 (solid line), CO_2, (dotted line), and the addition of 1 eq. $[NH_4][BF_4]$ under CO_2 (dotted-dashed line). 0.2 M Bu_4NBF_4 in DMF.

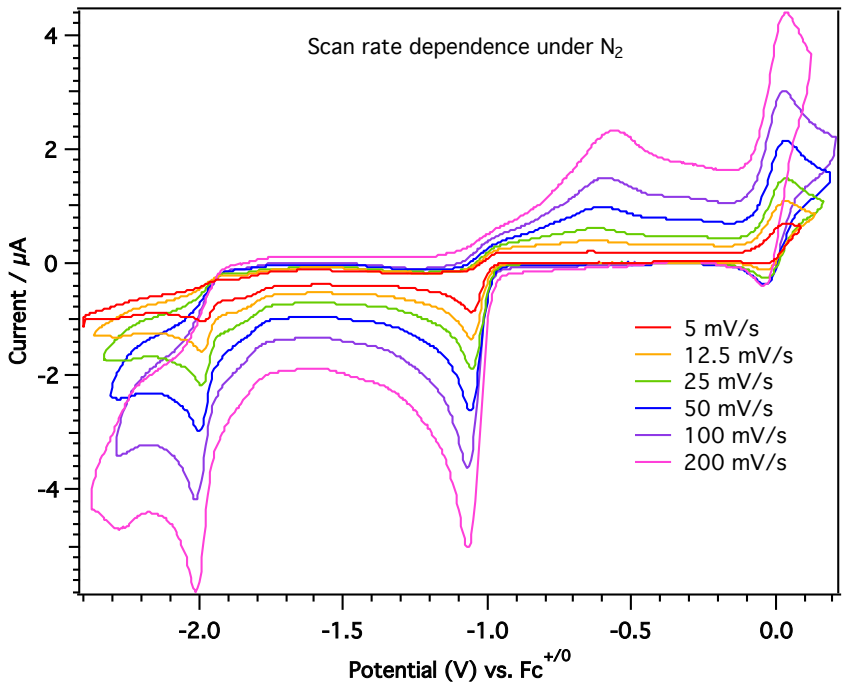

Figure A9. Scan rate dependent cyclic voltammogram of $[NiH_2L^1](BF_4)_2$. 0.2 M Bu_4BF_4 in DMF, Scan rate ranges from 5 mV/s (red) to 200 mV/s (pink).

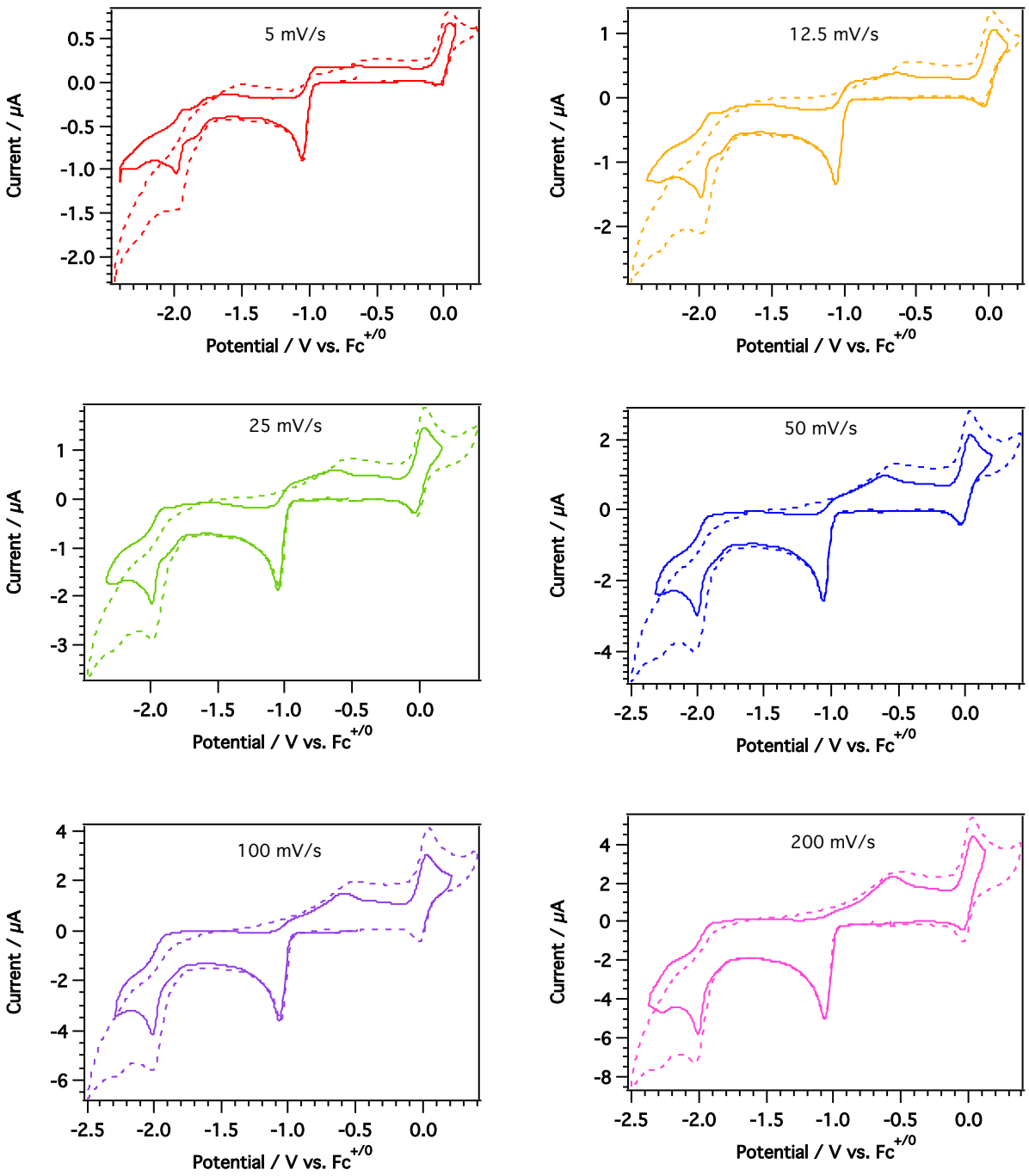

Figure A10. Cyclic voltammograms of $[NiH_2L^1](BF_4)_2$ varying by scan rate under N_2 (solid line) and CO_2, (dashed line). 0.2 M Bu_4NBF_4 in DMF.

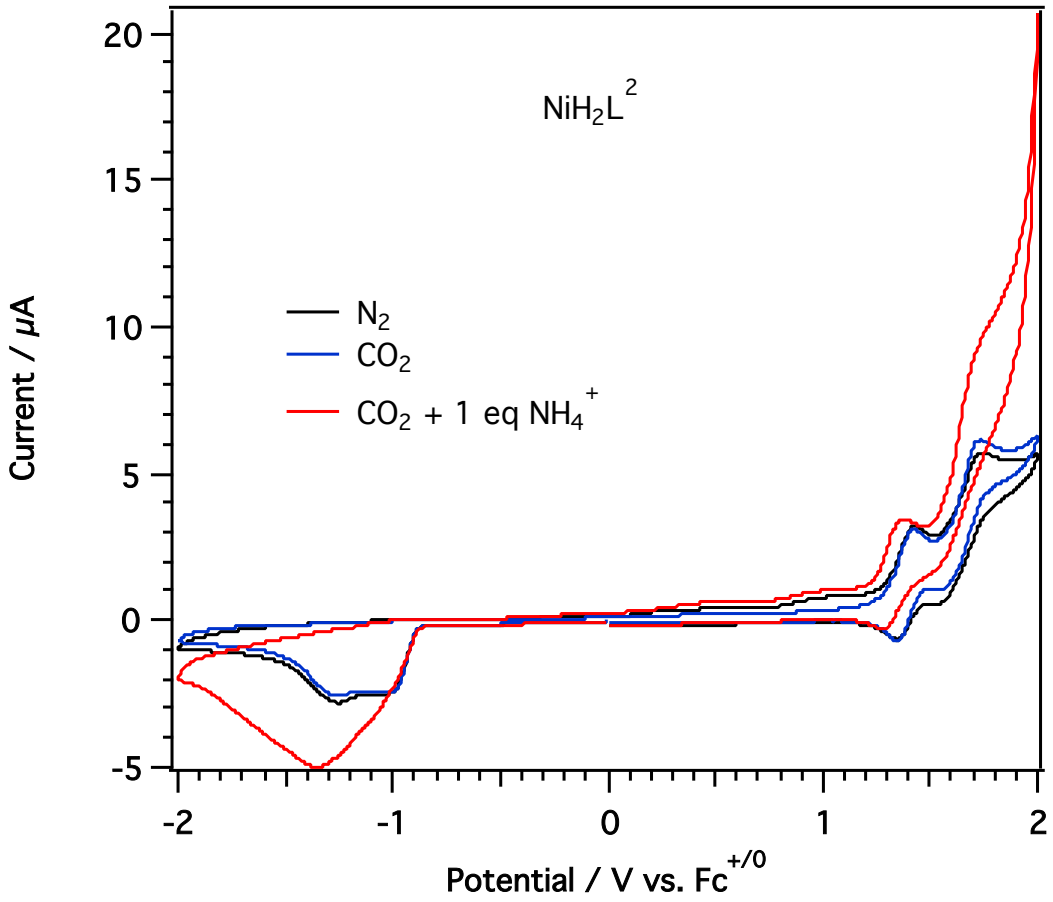

Figure A11. Cyclic voltammograms of $[NiH_2L^2](BF_4)_2$ under N_2 (black line), CO_2, (blue line), and the addition of 1 eq. $[NH_4][BF_4]$ under CO_2 (red line). 0.2 M Bu_4NBF_4 in DMF, 25 mV/s scan rate.

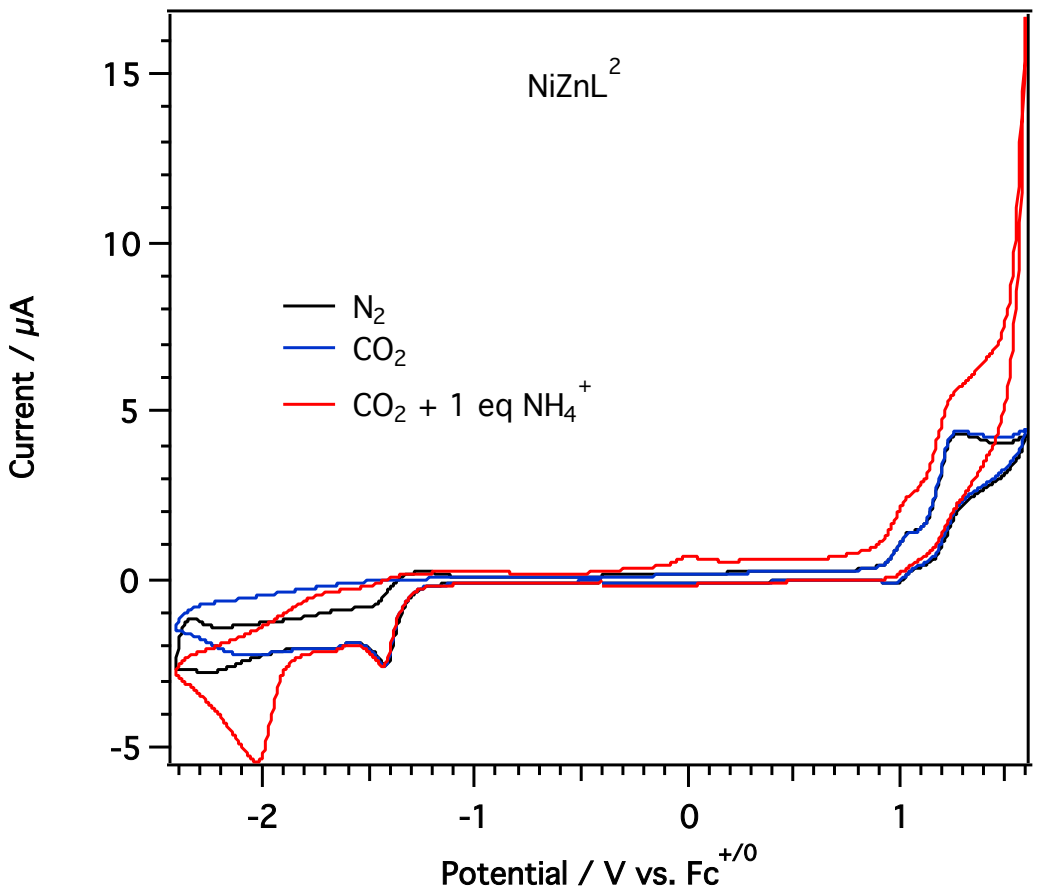

Figure A12. Cyclic voltammograms of $[NiZnL^2](BF_4)_2$ under N_2 (black line), CO_2, (blue line), and the addition of 1 eq. $[NH_4][BF_4]$ under CO_2 (red line). 0.2 M Bu_4NBF_4 in DMF, 25 mV/s scan rate.

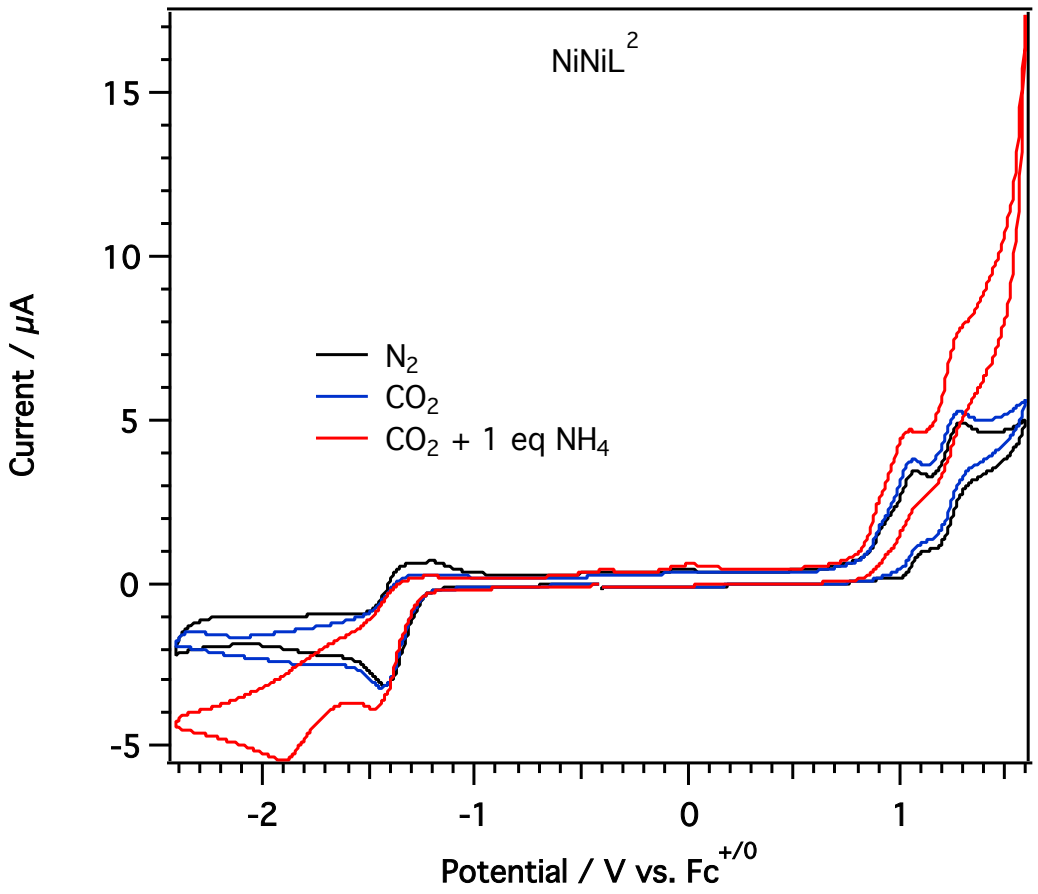

Figure A13. Cyclic voltammograms of $[Ni_2L^2](BF_4)_2$ under N_2 (black line), CO_2, (blue line), and the addition of 1 eq. $[NH_4][BF_4]$ under CO_2 (red line). 0.2 M Bu_4NBF_4 in DMF, 25 mV/s scan rate.

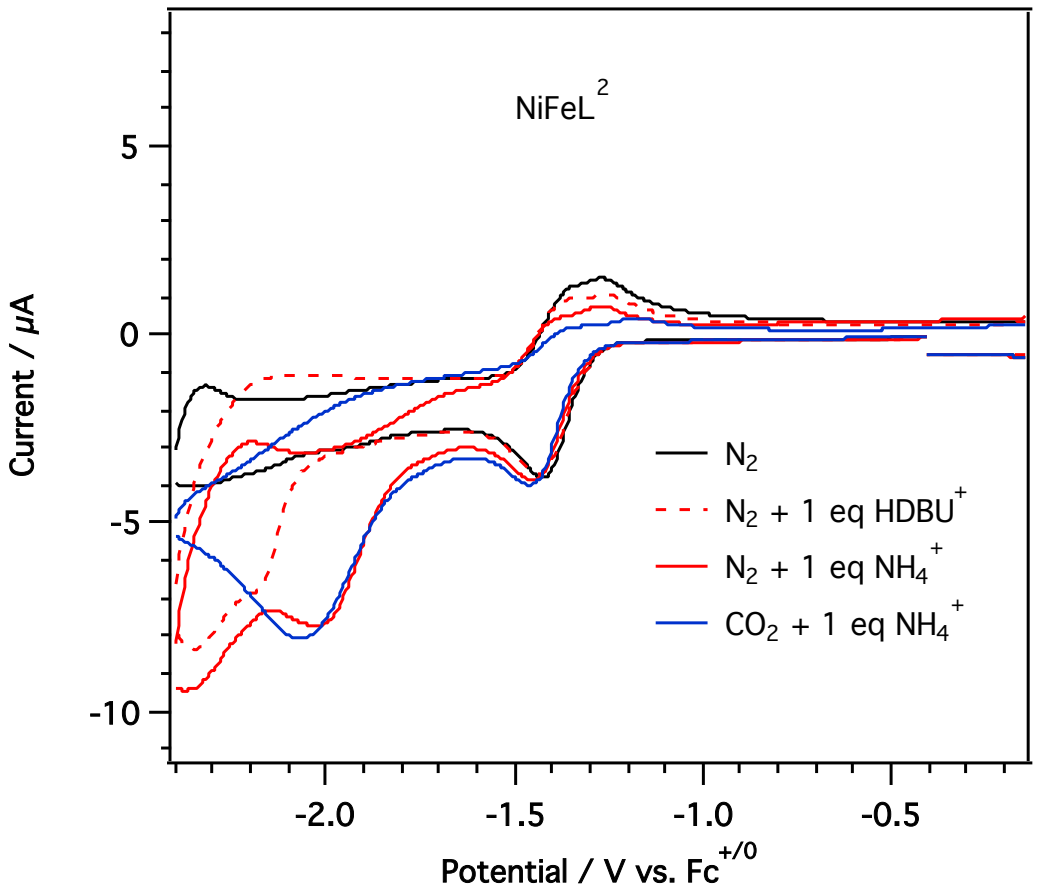

Figure A14. Cyclic voltammograms of $[NiFeL^2](BF_4)_2$ under N_2 (black line), the addition of 1 eq. H^+ (red lines), and the addition of CO_2 (blue line). 0.2 M Bu_4NBF_4 in DMF, 25 mV/s scan rate.

APPENDIX B

$[NiH_2L^3](BF_4)_2$

Table 1. Crystal data and structure refinement for jyy37.

Identification code	jyy37	
Empirical formula	C31 H43 B2 F8 N5 Ni O3	
Formula weight	766.03	
Temperature	88(2) K	
Wavelength	0.71073 Å	
Crystal system	Monoclinic	
Space group	C2/c	
Unit cell dimensions	a = 20.4789(7) Å	α= 90°.
	b = 16.2596(6) Å	β= 105.3032(4)°.
	c = 10.6419(4) Å	γ = 90°.
Volume	3417.9(2) $Å^3$	
Z	4	
Density (calculated)	1.489 Mg/m^3	
Absorption coefficient	0.652 mm^{-1}	
F(000)	1592	
Crystal color	orange	
Crystal size	0.45 x 0.31 x 0.27 mm^3	
Theta range for data collection	1.62 to 29.15°	
Index ranges	-27 <= h <= 26, -21 <= k <= 22, -14 <= l <= 14	
Reflections collected	21054	
Independent reflections	4386 [R(int) = 0.0202]	
Completeness to theta = 25.50°	100.0 %	
Absorption correction	None	
Max. and min. transmission	0.8461 and 0.7596	
Refinement method	Full-matrix least-squares on F^2	
Data / restraints / parameters	4386 / 0 / 249	
Goodness-of-fit on F^2	1.167	
Final R indices [I>2sigma(I) = 4207 data]	R1 = 0.0703, wR2 = 0.1693	
R indices (all data, ? Å)	R1 = 0.0725, wR2 = 0.1704	
Largest diff. peak and hole	0.574 and -0.483 e.$Å^{-3}$	

$[NiCuL^3](BF_4)_2$.

Table 5. Crystal data and structure refinement for jyy38.

Identification code	jyy38	
Empirical formula	C31 H41 B2 Cu F8 N5 Ni O3	
Formula weight	827.56	
Temperature	133(2) K	
Wavelength	0.71073 Å	
Crystal system	Monoclinic	
Space group	P2(1)/c	
Unit cell dimensions	a = 11.7841(6) Å	α= 90°.
	b = 15.2267(8) Å	β= 90.6542(7)°.
	c = 19.3190(10) Å	γ = 90°.
Volume	3466.2(3) $Å^3$	
Z	4	
Density (calculated)	1.586 Mg/m^3	
Absorption coefficient	1.241 mm^{-1}	
F(000)	1700	
Crystal color	red	
Crystal size	0.57 x 0.34 x 0.26 mm^3	
Theta range for data collection	1.70 to 28.76°	
Index ranges	-15 <= h <= 15, -19 <= k <= 19, -25 <= l <= 25	
Reflections collected	40763	
Independent reflections	8469 [R(int) = 0.0209]	
Completeness to theta = 25.50°	100.0 %	
Absorption correction	None	
Max. and min. transmission	0.7402 and 0.5397	
Refinement method	Full-matrix least-squares on F^2	
Data / restraints / parameters	8469 / 0 / 511	
Goodness-of-fit on F^2	1.110	
Final R indices [I>2sigma(I) = 7745 data]	R1 = 0.0404, wR2 = 0.0946	
R indices (all data, ? Å)	R1 = 0.0447, wR2 = 0.0964	
Largest diff. peak and hole	1.249 and -0.879 $e.Å^{-3}$	

$[Ni_2L^3](BF_4)_2$.

Table 8. Crystal data and structure refinement for jyy34a.

Identification code	jyy34a	
Empirical formula	C14 H17 B F4 N2 Ni O	
Formula weight	374.82	
Temperature	133(2) K	
Wavelength	0.71073 Å	
Crystal system	Monoclinic	
Space group	P2(1)/n	
Unit cell dimensions	a = 6.9448(6) Å	α= 90°.
	b = 10.2880(9) Å	β= 91.3330(10)°.
	c = 20.9612(18) Å	γ = 90°.
Volume	1497.2(2) $Å^3$	
Z	4	
Density (calculated)	1.663 Mg/m^3	
Absorption coefficient	1.343 mm^{-1}	
F(000)	768	
Crystal color	orange	
Crystal size	.15 x .194 x .317 mm^3	
Theta range for data collection	1.94 to 28.80°	
Index ranges	-9 <= h <= 8, -9 <= k <= 12, -28 <= l <= 16	
Reflections collected	4876	
Independent reflections	3256 [R(int) = 0.0244]	
Completeness to theta = 28.80°	83.1 %	
Absorption correction	None	
Refinement method	Full-matrix least-squares on F^2	
Data / restraints / parameters	3256 / 0 / 211	
Goodness-of-fit on F^2	0.943	
Final R indices [I>2sigma(I) = 2626 data]	R1 = 0.0375, wR2 = 0.1081	
R indices (all data, ? Å)	R1 = 0.0474, wR2 = 0.1141	
Largest diff. peak and hole	0.530 and -0.616 $e.Å^{-3}$	

$[NiCoL^3](BF_4)_2$.

Table 11. Crystal data and structure refinement for jyy36b.

Identification code	jyy36b	
Empirical formula	C47.50 H48 B4 Co2 F16 N7 Ni2 O3	
Formula weight	1347.45	
Temperature	296(2) K	
Wavelength	0.71073 Å	
Crystal system	Triclinic	
Space group	P-1	
Unit cell dimensions	a = 11.5681(11) Å	α= 106.1990(10)°.
	b = 16.2209(15) Å	β= 105.7400(10)°.
	c = 18.1038(18) Å	γ = 104.2350(10)°.
Volume	2943.7(5) $Å^3$	
Z	2	
Density (calculated)	1.520 Mg/m^3	
Absorption coefficient	1.279 mm^{-1}	
F(000)	1360	
Crystal color	orange	
Crystal size	0.42 x 0.41 x 0.09 mm^3	
Theta range for data collection	1.26 to 28.34°	
Index ranges	-15 <= h <= 7, -13 <= k <= 21, -23 <= l <= 23	
Reflections collected	15696	
Independent reflections	12282 [R(int) = 0.0598]	
Completeness to theta = 28.34°	83.5 %	
Absorption correction	None	
Max. and min. transmission	0.8936 and 0.6164	
Refinement method	Full-matrix least-squares on F^2	
Data / restraints / parameters	12282 / 0 / 776	
Goodness-of-fit on F^2	1.021	
Final R indices [I>2sigma(I) = 7134 data]	R1 = 0.0745, wR2 = 0.2292	
R indices (all data, ? Å)	R1 = 0.1205, wR2 = 0.2523	
Largest diff. peak and hole	3.093 and -0.600 $e.Å^{-3}$	

[NiZnL^3](BF$_4$)$_2$.

Table 14. Crystal data and structure refinement for jyy50a.

Identification code	jyy50a	
Empirical formula	C31 H41 B2 F8 N5 Ni O3 Zn	
Formula weight	829.39	
Temperature	173(2) K	
Wavelength	0.71073 Å	
Crystal system	Monoclinic	
Space group	P2(1)/c	
Unit cell dimensions	a = 12.7304(6) Å	α= 90°.
	b = 13.9945(7) Å	β= 105.3933(6)°.
	c = 21.1155(10) Å	γ = 90°.
Volume	3626.9(3) Å^3	
Z	4	
Density (calculated)	1.519 Mg/m^3	
Absorption coefficient	1.261 mm^{-1}	
F(000)	1704	
Crystal color	orange	
Crystal size	0.51 x 0.48 x 0.40 mm^3	
Theta range for data collection	1.66 to 29.21°	
Index ranges	-17 <= h <= 17, -19 <= k <= 19, -27 <= l <= 28	
Reflections collected	44198	
Independent reflections	9282 [R(int) = 0.0509]	
Completeness to theta = 25.00°	100.0 %	
Absorption correction	None	
Max. and min. transmission	0.6358 and 0.5662	
Refinement method	Full-matrix least-squares on F^2	
Data / restraints / parameters	9282 / 0 / 496	
Goodness-of-fit on F^2	1.077	
Final R indices [I>2sigma(I) = 7503 data]	R1 = 0.0606, wR2 = 0.1888	
R indices (all data, ? Å)	R1 = 0.0715, wR2 = 0.1950	
Largest diff. peak and hole	1.555 and -1.327 e.Å^{-3}	